

**Multilayer Film Deposition,
Characterization by Reflectometry
Techniques and Their Structure
Property Correlation**

By

MITALI SWAIN

PHYS01200904021

Bhabha Atomic Research Centre

*A thesis submitted to the
Board of Studies in Physical Sciences
In partial fulfillment of requirements
For the Degree of*

DOCTOR OF PHILOSOPHY

of

HOMI BHABHA NATIONAL INSTITUTE



March, 2015

Homi Bhabha National institute

Recommendation of the Viva Voce Board

As members of the Viva Voce Board, we certify that we have read the dissertation prepared by Ms. Mitali Swain entitled "Multilayer Film Deposition, Characterization by Reflectometry Techniques and Their Structure Property Correlation" and recommended that it may be accepted as fulfilling the dissertation requirement for the Degree of Doctor of Philosophy,

S. L. Chaplot Date: 29-9-2015
Chairman- Prof. S. L. Chaplot

Saibal Basu Date: 29-9-15
Guide- Prof. Saibal Basu

Ajay Gupta Date:
External Examiner- Prof. Ajay Gupta

Absent Date:
Member-1- Prof. M. Senthil Kumar

N.K. Sahoo Date: 29/9/2015
Member-2- Prof. N.K. Sahoo

Final approval and acceptance of this dissertation is contingent up on the candidate's submission of the final copies of the dissertation to HBNI.

I hereby certify that I have read this dissertation prepared under my direction and recommend that it may be accepted as fulfilling the dissertation requirement.

Date: 29/09/2015

Place: Mumbai

Saibal Basu 29.9.15
Guide: Dr. Saibal Basu

डॉ. सैबल बसु / Dr. Saibal Basu
अध्यक्ष, एस.एस.पी.डी./Head, SSPD
भारत सरकार, भा.प.अ.केंद्र/Govt. of India, BARC
ट्रॉम्बे, Trombay, / मुंबई, Mumbai - 400 085.

STATEMENT BY AUTHOR

This dissertation has been submitted in partial fulfillment of requirements for an advanced degree at Homi Bhabha National Institute (HBNI) and is deposited in the library to be made available to borrowers under rules of the HBNI.

Brief quotations from this dissertation are allowable without special permission, provided that accurate acknowledgement of source is made. Requests for permission for extended quotation from or reproduction of this manuscript in whole or in part may be granted by the Competent Authority of HBNI when in his or her judgment the proposed use of the material is in the interests of scholarship. In all other instances, however permission must be obtained from the author.

Mitali Swain
Mitali Swain

DECLARATION

I, hereby declare that the investigations presented in the thesis have been carried out by me. The work is original and has not been submitted earlier as a whole or in part for a degree / diploma at this or any other institution / university.

Mitali Swain
Mitali Swain

List of publications:

Journals:

1. **Micro-structural characterization of low resistive metallic Ni Germanide growth on annealing of Ni-Ge multilayer.**
M. Swain, S. Singh, D. Bhattacharya, A. Singh, R.B. Tokas, C.L. Prajapat and S. Basu, AIP Advances **5**,077129 (2015).
2. **Stoichiometry dependent inter diffusion and structural evolution in Al-Ni multilayer.**
M. Swain, S. Singh, S. Basu, D. Bhattacharya, R. B Tokas and M. Gupta. J. Alloy. Compd. **631**, 46–51 (2015).
3. **Identification of a kinetic length scale which dictates alloy phase composition in Ni-Al interfaces on annealing at low temperatures.**
M. Swain, S. Singh, S. Basu, D. Bhattacharya and M. Gupta, J. App. Phys. **116**, 222208 (2014).
4. **Effect of interface morphology on intermetallics formation upon annealing of Al-Ni multilayer.**
Mitali Swain, Surendra Singh, Saibal Basu, Mukul Gupta. J. Alloy. Compd. **576**, 257–261 (2013).

Publications in Conferences/ Symposia:

1. **Deposition of Optical Quality Cu/Ti films.**
Mitali Swain, Debarati Bhattacharya, and Saibal Basu, AIP Conf. Proc. 1591, 946-947, (2014).
2. **Thermal Diffusion in Ni/Al Multilayer.**
M. Swain, D. Bhattacharya, S. Singh, M. Gupta and S. Basu, AIP Conf. Proc. 1512, 678-679, (2013).
3. **Characterization of Ni/Al multilayer on Si substrate by diffraction and reflectometry techniques.**
Mitali Swain, Saibal Basu, Debarati Bhattacharya and Mukul Gupta, AIP Conf. Proc. 1447, 647-648, (2012).
4. **Characterization of Sputtered Samples in Fe-Cu System.**
D. Bhattacharya, T.V.Chandrasekhar Rao, K.G.Bhushan, M. Swain and S.Basu, AIP Conf. Proc. 1451, 319-321,(2012).

5. **Deposition of a Nickel Film by DC Magnetron Sputtering and its Characterization.**

M. Swain, D.Bhattacharya, K.G Bhushan, and S. Basu, AIP Conf. Proc. 1451, 182-184, (2012).

6. **Design and Development of a D.C. Magnetron Sputtering System for Thin Film and Multilayer Deposition.**

D. Bhattacharya, A. Biswas, K.G. Bhushan, **M. Swain** and S. Basu. AIP Conf. Proc. 1349, 487-488, (2011).

Dedicated to
My Late Grandfather

Acknowledgements

First and foremost, I express my deepest sense of gratitude to my thesis advisor, Dr. Saibal Basu, for his invaluable guidance, productive discussions, critical observations and constant encouragement in every step of my Ph.D work. I could not have asked for a more knowledgeable, thorough person to work with.

My sincere thanks to Dr.(Ms.) Debarati Bhattacharya, SSPD, BARC for her encouragement and help from the very beginning of my research work. Without her guidance and support it would never have been possible for me to grow as a research student.

Next, and very importantly, I am greatly indebted to Dr. Surendra Singh, SSPD, BARC, without whom I could never accomplish this work. He has been a valuable mentor for me. I thank him for his expert guidance, precious time and encouragement throughout this research work, and for driving me to extrapolate the limit of my abilities.

I sincerely acknowledge, professionally and personally, the help of Mr. Swapan Jana SSPD, BARC at every step of working with the sputtering unit and to understand the technical drawings.

I take the pleasure to thank all the members of my doctoral committee, Dr. S. L. Chaplot (Director, Physics Group, BARC), Dr. N.K Sahoo (Head , A&MPD, BARC) and Prof. Senthil Kumar (Department of Physics, IIT Bombay) for their constant guidance and support to the present thesis work.

I gratefully acknowledge Dr. R. Mukhopadhyay (Head, SSPD, BARC) for his support for this thesis work.

I thank all the office staff of SSPD, BARC, India, for their help during all the paper work related to the present work. I also thank each and every member of SSPD, BARC who directly/indirectly helped me in completing my thesis work.

I would like to gratefully acknowledge the help and support from my collaborators Dr. Mukul Gupta (UGC DAE Consortium for Scientific Research, Indore, India), Mr. R.B Tokas (A&MPD, BARC, India), Mr. C.L Prajapat (TPD, BARC, India), Dr Ajay Singh (TPD, BARC, India) for their collaboration that has helped me to complete my work.

I thank Department of Atomic Energy (DAE), INDIA, for providing the fellowship and financial support to attend various conferences/symposia.

My sincerest thanks to my friend, Ms. Dipti Biswal (L&PTD, BARC), for her invaluable help and moral support. Without her, I could not complete the writing of this thesis. I also thank Mr. Shuvendu Jena (A&MPD, BARC) for his valuable suggestions during preparation of this thesis. I thank my friends at BARC Nitya, Sohini, Priyanka, Suresh and all others for their moral support in accomplishing this work.

Last but not the least, I would like to thank my supporting pillars, my parents (Batakrisna and Geetanjali) for standing by me in all my ups and downs and eternally reminding me to believe in myself. My special thanks to my brother Ambika, my sisters (Sonali and Rosalin), who are the main building blocks of my educational carrier. Without their guidance, I could never reach this level of confidence. I also thank my uncle (Mihir) for his encouragement and support for my Ph.D. I am immensely indebted to my grandmother (Sita Devi) for her love and blessings that has been a moral boost for me all the time.

Contents

Synopsis	1
List of Figures:	7
List of Tables	11
Chapter 1: Introduction	12
1.1 Thin films, surfaces, interfaces.....	12
1.2 Deposition techniques	15
1.3 Characterization methods	17
1.3.1 Polarized Neutron and X-Ray Reflectometry (PNR and XRR).....	17
1.4 Multilayer films: Nickel-Aluminides, Nickel-Germanides.....	20
1.5 Diffusion in thin films.....	22
1.5.1 Fick's laws of diffusion	23
1.5.2 Diffusion constant from reflectometry experiments	26
Chapter 2: Thin Film Deposition	28
2.1 Introduction	28
2.2 Sputtering	30
2.3 Advantages of sputtering over other deposition methods	31
2.3.1 DC/RF sputtering	31
2.3.2 Magnetron Sputtering	32
2.4 Parameters affecting sputtering	34
2.4.1 Base Vacuum	34
2.4.2 Target substrate geometry.....	34
2.4.3 Sputter gas pressure.....	35
2.4.4 Target/Substrate Temperature.....	36
2.5 Optimization of a DC/RF magnetron sputtering unit	36
2.5.1 Description of the system	37
2.5.2 Steps for deposition	39
2.5.3. Samples prepared	41
Chapter 3: Neutron and X-ray Reflectometry	48
3.1 Reflectometry at a glance	48
3.2 Neutron and X-ray Reflectometry at an interface	50
3.2.1 Refractive Index and Critical Angle.....	52

3.2.2 Reflectivity from a rough surface	54
3.3 Polarized Neutron Reflectometry (PNR)	58
3.4 Polarized Neutron Reflectometer at DHRUVA	62
3.4.1 Description of the instrument.....	63
3.4.2 Control and data acquisition system.....	65
3.4.3 Resolution of the instrument	67
3.4.4 Analysis of Specular Reflectometry data	68
3.4.5 Estimation of errors in fitted parameter.....	71
3.5 Determining stoichiometry of interface alloy layer by XRR and PNR	72
Chapter 4: Nickel Aluminides (Effect of interface morphology, kinetics of alloy formation and stoichiometry dependant inter diffusion).....	74
4.1. Introduction	74
4.2 Sample preparation and characterization techniques.....	76
4.3 Effect of interface morphology on alloy phase formation:	78
4.3.1 Results and Discussion:	79
4.3.2 Summary.....	88
4.4 Identification of a kinetic length scale	88
4.4.1 Results and Discussion	89
4.4.2 Summary	99
4.5 Stoichiometry dependent inter diffusion and structural evolution	100
4.5.1. Results and Discussion	101
4.5.2 Summary	111
Chapter 5: Nickel Germanides (Micro-structural characterization of low resistive metallic Ni Germanide growth on annealing of Ni-Ge multilayer)	113
5.1 Introduction	113
5.2 Sample preparation and experimental details.....	115
5.3 Results and discussion	116
5.4 Summary	127
Chapter 6: Summary and Future Directions	128
6.1 Summary	128
6.2 Future Directions	132
References.....	134

Synopsis

Present thesis comprises deposition and characterization of thin films using reflectometry techniques. It primarily targets growth of interface alloys formed by annealing of multilayer films. The definition of thin films varies widely depending on the context. For the work reported in this thesis, we defined thin film as a layer (or multiple layers, multilayers in short) of material deposited on a substrate with thickness ranging from few nanometers to hundreds of nanometers. A thin film can be considered as a quasi two-dimensional (2D) structure, since its thickness is much smaller compared to its other two dimensions. Due to their reduced dimensionality, thin films often have properties quite different from their bulk counterpart and can be tuned for various technical applications. They are also of interest for basic understanding of growth of interfacial layers. The list of application of thin films is quiet long, but few are worth mentioning viz. intermetallics in corrosion and oxidation protection, magnetic thin films as magnetic storage elements, magnetic sensors, metal-semiconductor systems in microelectronics etc. Thin films of dissimilar elements can be deposited alternately producing multilayer structures. These tailored structures have larger surface to volume ratio, are not fully dense, contain defect structures and hence possesses different structural, magnetic and electronic properties.

Apart from the application aspect these multilayered thin films are well-suited for study of surface and interface effects as they provide number of reacting interfaces between its constituting elements and enhancing the effects to be observed. These reacting interfaces don't follow the conventional equilibrium phase diagram during solid state reaction. Hence it is of interest to identify the first alloy phase formed in a multilayer system during annealing. Diffusion study of constituting elements in a solid state reaction is also important for understanding of kinetics of phase formation in such systems. It is worth

studying kinetics of alloy formation at microscopic length scales. In the present thesis we have identified first alloy phase formed in binary systems of Ni-Al and Ni-Ge due to annealing at nanometer length scales using x-ray and polarized neutron reflectometry (XRR and PNR) techniques. In both the systems we have also studied kinetics of the components and estimated the diffusion constants at the temperature of annealing.

The interface properties of a multilayer thin film play crucial role in deciding the properties of the system. In this regard it is of importance to grow thin films with controlled thickness and interface quality and to characterize the films to understand the structure-property correlation in these films. In recent days, there has been major improvement in thin film deposition and characterization techniques, which allows one to deposit ultra-thin films in a controlled manner and also characterize them with resolution in the range of nanometers. The work presented in the thesis primarily consists of deposition of multilayer thin films and their detailed characterization at various stages of annealing, to study growth of interface alloy layers of interest.

A solid interface consists of a small number of atomic layers that separates two dissimilar solids in intimate contact with one another. An ideal interface has a sharp boundary between two materials. But in reality there is penetration of material across the boundary due to inter-mixing of the components or due to roughness at the interface, which is a measure of jaggedness at the interface. A real interface is a combination of both these effects making the interface broader compared to the ideally flat interface. During thermal annealing interface alloying takes place at the interfaces. We have studied such alloy layers forming at the interfaces in details in the present thesis.

Chapter 1 gives a brief introduction about thin films, surfaces, interfaces, their importance and the type of studies carried out in the present thesis. Diffusion is one of the basic processes associated with the interfaces in case of thin films. Solution to Fick's

second law of diffusion and its application to thin films in terms of intensity of Bragg peaks is described in detail in this chapter.

Using various growth techniques, one can create artificial multilayers with interfaces between dissimilar materials, which otherwise may not occur in nature, with control at atomic/molecular level. Thin film deposition techniques are of considerable interest for creating new materials. There are several methods for preparation of thin films which may be broadly classified as physical vapor deposition (PVD) and chemical vapor deposition (CVD). Among several PVD methods, we will focus on the sputtering technique in details here, since the films used in the present work were deposited using this technique. Sputtering can be broadly divided into two types, DC and RF. These techniques, combined with magnetic field on the target, constitute DC magnetron or RF magnetron sputtering. DC sputtering is usually used for conducting targets and RF for insulating and semiconducting targets. In case of magnetron sputtering, a transverse magnetic field \vec{B} is used to trap the electrons in a helical path near the target surface in order to increase the ionisation efficiency of the electron gas close to the target, increasing sputtering yield. Involvement of many parameters such as sputter gas pressure (Ar), deposition rate, base vacuum etc. makes sputter deposition a complex process, but also allow a large degree of control over the growth and microstructure of the film. The author has carried out optimisation of a DC/RF magnetron sputtering unit as a part of the work reported in this thesis and will be discussed in chapter 2.

Polarized Neutron Reflectometry (PNR) and X-ray Reflectometry (XRR) have been used as the primary characterization tools in the present thesis. X-ray being an electromagnetic radiation interacts with atomic electrons and can reveal the electron scattering length density profile (ESLD). The neutron primarily interacts with the atomic nuclei and

neutron reflectometry gives nuclear scattering length density (NSLD), which is complementary to ESLD obtained from x-ray reflectometry (XRR). Neutrons are electrically neutral, and can penetrate matter more deeply and hence are valuable probes for buried layers and interfaces. In addition, neutrons carry a magnetic moment of $-1.91 \mu_n$ that interacts with the atomic magnetic moment present in the system (due to the unpaired electrons), capable of giving also the magnetization depth profile of the system along with the nuclear density profile. PNR and XRR are two non-destructive techniques, which can characterize thin films with sub-nanometer resolution. Especially PNR is a unique tool to study magnetization depth profile in thin films. Special attempt has been made to characterize the structure and magnetic properties at the interfaces in the thin film multilayers studied. Interface alloys have been formed by controlled annealing in several multilayers with binary elements viz. metal/metal and metal/semiconductor components. Detailed theory of XRR, PNR and their use in determination of exact alloy stoichiometry, diffusion constant and growth of first phase at the interfaces has been described in detail in chapter 3.

Transition metal aluminides, especially Ni aluminides, have been recognized as possible candidates for a variety of high-temperature structural applications. They are suitable to operate well beyond the operating temperatures of conventional materials due to their excellent oxidation and corrosion resistant properties. Ni is hard, ductile, ferromagnetic and a good conductor of heat and electricity. It also has excellent corrosion-resistant properties. Aluminum on the other hand is light, non-magnetic and fairly ductile. With the advent of several deposition techniques these days, we can combine both elements in a desired manner to produce specific alloys having ordered crystal structure with a combination of desirable physical and mechanical properties viz. light weight, good mechanical strength, high hardness, and high melting point. Nickel

aluminides are heavily used in the field of aeronautics and automobiles due to their suitable properties mentioned above. The phase diagram of Ni/Al binary system has been studied extensively both experimentally as well as theoretically. There are several stable nickel aluminides NiAl_3 , NiAl , Al_3Ni_2 , Ni_3Al according to their equilibrium phase diagram. Hence Ni/Al system offers an excellent platform to study the kinetics of first phase formation at the interface. Details of interface alloy formation have been studied in several ultra-thin multilayer films of Ni/Al using PNR and XRR in the present thesis. Surface energy effect on the interfaces has been discussed in detail in Ni/Al systems. The kinetics of interface alloy formation on annealing, their composition and dependence on initial stoichiometry have been studied with nanometer resolution. We have obtained a kinetic length scale which dictates the local density responsible for stoichiometry of the alloy phase. Results of the studies carried out on Ni/Al multilayer samples have been described in chapter 4 of the thesis.

Several magnetic hetero-structures such as semiconductors/ferromagnets, and ferromagnets/antiferromagnets exhibit properties required for applications in microelectronics. These combinations acquire properties that are important in the field of magnetism, nanotechnology and semiconductor technology. Nickel Germanides are one of the important class among the transition metal Germanides. They are suitable candidates for inter-connects in MOSFET applications, as they form low resistive phases on annealing. In the present thesis low-resistance Ni-Germanide phase has been formed at the interfaces of a Ni/Ge multilayer film by controlled annealing and has been characterized for its composition, transport and magnetic properties. This study has been discussed in detail in chapter 5. The Ni/Ge systems were prepared by the DC/RF magnetron sputtering unit described in chapter 2.

Chapter 6 gives a brief summary of the research work carried out in the present thesis and future directions for further studies. Work presented in the thesis highlights the study of structural and magnetic properties at nanometer length scales. The work also demonstrates that x-ray and neutron reflectometry techniques can be successfully used to study kinetics of diffusion in case of the thin films.

List of Figures:

1.1 Schematic of different type of interfaces (a) An ideal interface, (b) Interface with mixing of components (upper panel) and roughness (lower panel) and (c) Interface alloy layer of two primary components, A and B in a binary system.....	14
1.2 XRR profile of (a) an infinitely thick Si layer and (b) from Ge layer [Ge Si (substrate) /Ge(200 Å)].....	19
1.3 (a)Un polarized and (b) polarized neutron reflectometry from a Ni-Al multilayer [Si (substrate) /Al(25Å)/Ni(50Å)]×10].....	21
1.4 Flux across area ‘A’ due to particle flux J(x).....	23
1.5 (a) Reduction in Bragg peak intensity due to diffusion (inset shows interface alloy layer formation due to diffusion) (b) diffusion at atomic level	27
2.1 Classification of thin film deposition methods.....	29
2.2 Schematic of Sputtering.....	30
2.3 Schematic showing the magnetic field and target assembly in a RF magnetron sputtering set up.....	33
2.4 Sputter Yield/ Deposition rate as a function of sputter gas pressure (Ar).....	36
2.5 Cross-sectional schematic view of the D.C./RF magnetron sputtering system layout.....	38
2.6 Photograph of the sputtering unit at SSPD, BARC during deposition.....	40
2.7 XRR profile of Ni(380Å)/Si.....	42
2.8 (a) XRR profile (b) XRD profile of the Ni film [Ni(222Å)/Si] deposited on Si substrate.....	42
2.9 XRR of Si/Cu (405Å)/Ti (286Å)	43
2.10 XRR of Si/[{Cu(56Å)/Ti(76Å)}×5]	44
2.11 XRR profile of Ge films with varying sputter power (a) with 20W (b) with 50W.....	45
2.12 XRR profile of a Ni-Ge bilayer [Si/[Ni(93Å)/Ge(215Å)]].....	46

2.13	PNR profile of a Ni-Ge multilayer { Si (substrate) / [Ni _{100Å} / Ge _{200Å}] [×] 4}	46
3.1	Geometry of specular and off-specular (diffuse) reflectivity (b) wave function at the interface	50
3.2	Effect of roughness on specular reflectivity from Si substrate with $\sigma = 0 \text{ \AA}$ (solid line) and $\sigma = 10 \text{ \AA}$ (dashed line). Inset (a) shows image of rough interface with Gaussian profile of height. The standard deviation of the Gaussian function describing the roughness represents the root mean square roughness, σ	54
3.3	Diagram of a multilayer stack containing N layers, where the refractive index, thickness, propagation angle, and interface roughness parameter of the i^{th} layer are n_i , d_i , θ_i and σ_i , respectively	56
3.4	Schematic, representation of the scattering geometry, for polarized neutron reflectivity measurements, used in the present thesis	60
3.5	Simulated (a) un-polarized and (b) polarized neutron reflectivity pattern for Ni/Al multilayer	62
3.6 (a)	Schematic of Polarized Neutron Reflectometer at Dhruva reactor	64
3.6 (b)	Photograph of the Polarized Neutron Reflectometer at Dhruva reactor	65
3.7	Steps involved in working of GA. (I is the number of iteration)	70
3.8	Schematic of alloy layer formation in a bilayer	73
4.1	Polarized Neutron Reflectivities, R^+ (solid circles) and R^- (open circles) for as deposited (a) and sample annealed at 160°C for 1hr (b), 4hr (c) and 8hr (d) along with fits (solid lines) to the data	80

4.2 Nuclear scattering length density (SLD) profiles (a) for as deposited sample and sample annealed at 160°C for (b) 1hr, (c) 4hrs (d) 8hrs, and (e)-(h) show the corresponding magnetization (M) depth profiles.....	81
4.3 Nuclear scattering length density (SLD) depth (a) and magnetization (M) depth (b) profiles across Ni on Al (Ni/Al) and Al on Ni (Al/Ni) interfaces of the Ni-Al bilayer.....	82
4.4 (a) X-ray reflectivity (XRR) data from the as-deposited sample and sample annealed at 160°C for 8 hrs. (b) Electron scattering length density (SLD) profile of the sample which gave best fit to XRR data (Fig. (a)). (c) represents the Electron SLD profile across Ni/Al and Al/Ni interfaces of a Ni-Al bilayer.....	85
4.5 Variation of magnetization (M) of Ni layer (a) and diffusion length (b) as a function of annealing time. Inset of (b) shows the X-ray reflectivity (XRR) data across first order Bragg peak for as-deposited sample and sample annealed at 160°C for different times.....	86
4.6 (a) and (b) show x-ray diffraction (XRD) pattern from as-deposited and annealed (at 150°C and 300°C) samples S1 and S2, respectively, (c),(d) shows SIMS profiles for as-deposited samples for S1 and S2 respectively, (e),(f) shows corresponding annealed profiles for SIMS at 300°C.....	91
4.7 (a) and (b) show x-ray reflectivity (XRR) profile from as-deposited and annealed (at 150°C and 300°C) samples S1 and S2 respectively, (c) and (d) show corresponding electron scattering length density (ESLD) profiles from fits to the XRR data.....	92
4.8 (a) and (b) show polarized neutron reflectivity (PNR) profiles R^+ (red solid circles) and R^- (blue open circles) from as-deposited and annealed (at 150°C and 300°C) samples S1 and S2 respectively, (c) and (d) show corresponding nuclear scattering length density (NSLD) profiles for samples S1 and S2, respectively, (e) and (f) show magnetization depth profiles for samples S1 and S2, respectively.....	95

4.9	Block diagrams for two bilayers in S1 and S2 for the as-deposited samples and after annealing the same at 300°C. Lengths of the coloured blocks are proportional to the thickness of the corresponding elements and the alloy layers (after annealing). The ‘virtual Kirkendall markers’ allows to compare the position of the interfaces before annealing and the growth of the alloy layers after annealing with the substrate-film interface as a fixed reference line.....	99
4.10	X-ray diffraction (XRD) pattern for as-deposited and annealed (150°C, 200°C, 300°C) states for samples S1(a) and S2(b), respectively. Open triangles, solid triangles and solid squares mark the possible Bragg peaks for alloy phases.....	102
4.11.	Variation of alloy peak as a function of annealing temperatures (150°C, 200°C, 300°C) for samples, S1 (left panel) and S2 (right panel) respectively.....	104
4.12.	Height-difference correlation function ($g(r)$, open circles) with the fit (solid lines) from samples, S1 and S2 for as deposited and annealed state obtained from AFM. (Inset shows corresponding 3-dimensional AFM images of size (2 μm \times 2 μm)).....	105
4.13	Spin ASYM $[(R^+ - R^-)/(R^+ + R^-)]$ function (closed circles) with fit (solid lines) at different temperature of annealing for S1 [(a)-(d)] and S2 [(e)-(h)].....	107
4.14	Measured reflectivity profiles for spin up (R^+) neutrons for as deposited and annealed state at 300°C for samples S1 (a) and S2 (b) respectively. Inset of (a) shows Bragg Peak intensity variation as a function of different annealing temperature for S1.....	108
4.15	Arrhenius plot for growth of alloy phase in sample S1 and S2.....	109
4.16	Variation of (a) crystallite size (b) alloy layer thickness (c) average magnetic moment of Ni atom in individual layers as a function of annealing temperature for S1 and S2. Lines drawn are just a guide to visualization.....	110

5.1 Resistance measurement of the Ni-Ge multilayer at different stages of annealing by Four probe method. All the measurements were carried out on samples of same geometry.....	117
5.2 X-Ray diffraction of the sample for the (a) as deposit and (b) annealed stage at 250 °C for 4hr, Panel below shows the possible XRD Bragg peaks.....	118
5.3 Height-difference correlation function for the as deposited and annealed state at 250°C_4hr (Inset shows respective 3d-AFM image of the film surface (2×2μm ²).....	120
5.4 (a) PNR measurements from the as-deposited and annealed samples along with fits (solid lines) (b) Nuclear scattering length density (NSLD) and (c) magnetic scattering length density (MSLD) depth profile of a single Ni-Ge bilayer, that fits the PNR data shown in 2(a). (d) XRR profiles for as-deposited and annealed sample along with fits and (e) corresponding electron scattering length density (ESLD) profile of a single Ni-Ge bilayer.....	121
5.5 SQUID measurement profiles for the as deposited and sample annealed at 250 °C for 4h.....	123
5.6 Variation in (a) layer thicknesses of Ni, Ge and the alloy layer and (b) resistance of the Ni-Ge multilayer sample at 300 K as a function of annealing time. (c) left panel show the schematic of interface before and after annealing the Ni/Ge multilayer sample. Right panel show the schematic of a parallel combination of resistors with Ni and Ge in alternating positions and considering only the Ni layers as resistors in the as deposited state.....	125

List of Tables

2.1 Sputtering parameters of deposited systems.....	39
3.1 Specification of PNR instrument	66
4.1 Physical parameters obtained from XRR and PNR.....	84

Chapter 1: Introduction

- 1.1 Thin films, surfaces and interfaces
- 1.2 Deposition techniques
- 1.3 Characterization Methods
 - 1.3.1 Neutron and X-ray reflectometry techniques
- 1.4 Multilayer films: Nickel-Aluminides, Nickel-Germanides
- 1.5 Diffusion in thin films
 - 1.5.1 Fick's laws of diffusion
 - 1.5.2 Diffusion constant from reflectometry experiments

1.1 Thin films, surfaces, interfaces

The definition of thin films varies widely depending on the context. For the work reported in the thesis, we defined thin film as a layer (or multiple layers, multilayers in short) of material deposited on a substrate with thickness ranging from few nanometers to hundreds of nanometers. A thin film can be considered as a quasi two-dimensional (2D) structure, since its thickness is much smaller compared to its other two dimensions. Due to their reduced dimensionality, thin films often have properties quite different from their bulk counterpart and can be tuned for various technical applications and are also of interest for basic understanding of interface growth [1]. The list of application of thin films is quiet long, but few are worth mentioning viz. intermetallics in corrosion and oxidation protection, magnetic thin films as magnetic storage elements, magnetic sensors, metal-semiconductor systems in microelectronics etc.[2-4]. Thin films of dissimilar elements can be deposited alternately producing multilayer structures. These tailored structures have larger surface to volume ratio, are not fully dense, contain defect structures and hence possesses different structural, magnetic and electronic properties [5,6]. Apart from the application aspect these multilayered thin films are well-suited for study of surface and interface effects as they provide number of

reacting interfaces between its constituting elements and enhancing the effects to be observed [7]. These reacting interfaces don't follow the conventional equilibrium phase diagram during solid state reaction [8]. Hence it is of interest to identify the first alloy phase formed in a multilayer system. Diffusion study of constituting elements in a solid state reaction is also important for understanding of kinetics of phase formation in such systems [9,10]. It is worth studying kinetics of alloy formation at microscopic length scales. In the present thesis we have identified first alloy phase formed in binary systems of Ni-Al and Ni-Ge due to annealing at nanometer length scales using neutron and x-ray reflectometry techniques.

The interface properties of a multilayer thin film play crucial role in deciding the properties of the system [4,5]. In this regard it is of importance to grow thin films with controlled thickness and interface quality and to characterize the films to understand structure-property correlation in these films [7, 10]. In recent days there have been major improvement in thin film deposition and characterization techniques, which allows one to deposit ultra-thin films in a controlled manner and also characterize them with resolution in the range of nanometers. The work presented in the thesis primarily consists of deposition of multilayer thin films and their detailed characterization at various stages of annealing, to study growth of interface alloy layers of interest.

A solid interface consists of a small number of atomic layers that separates two dissimilar solids in intimate contact with one another. Schematic of an ideal and actual interface of constituent elements A and B is given in Fig.1.1 Fig.1.1(a) shows an ideal interface with a sharp boundary between two materials. In reality there is penetration of material across the boundary due to inter-mixing of the components [Fig. 1.1 (b), upper panel] or due to roughness at the interface [Fig.1.1 (b), lower panel]), which is a measure of jaggedness at the interface. A real interface is a combination of both these effects making the interface

broader compared to the ideally flat interface. Fig. 1.1(c) shows an alloy layer at the interface of the primary constituents A and B. We have studied such alloy layers forming at the interfaces in details in the present thesis.

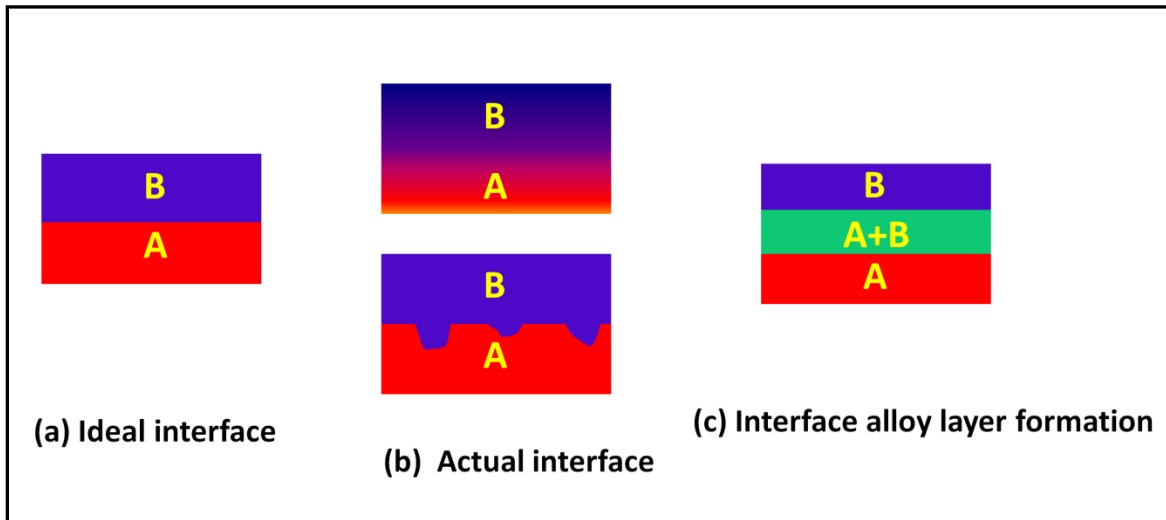


Figure 1.1: Schematic of different type of interfaces (a) An ideal interface, (b) Interface with mixing of components (upper panel) and due to roughness (lower panel) (c) Interface alloy layer of two primary components, A and B in a binary system.

The surface of a solid is where the solid is in contact with the surrounding world i.e., the atmosphere or vacuum. Similarly as we have seen an interface is a boundary between two different materials. Rapidly growing application of thin films and various available techniques of their deposition have made thin films studies more relevant these days as it opens up new possibilities for fabricating materials of technological interest in various fields. Surface and interface physics is related to various important properties of thin film/multilayer systems such as diffusivity [9,10], magnetism [11], charge/spin transport properties [12,13] which have been studied widely. Apart from the structural parameters of the systems such as thickness, roughness, mass density of the individual layers, we have also studied diffusion and magnetic property variation across the layers of a multilayer system in the present thesis. Quality of the film and interface, uniformity of growth, first

phase formation on annealing has been quantified with help of various characterization techniques [10-14] .With controlled solid state reaction one can grow desired intermetallics alloys of particular stoichiometry which is of technical interest [7].

Polarized Neutron Reflectometry (PNR) and X-ray Reflectometry (XRR) are two non-destructive techniques, which can characterize thin films with sub-nanometer resolution [15,16]. Especially PNR is a unique tool to study magnetization depth profile in thin films. These two techniques have been used as primary tools for characterization of thin films along with x-ray diffraction (XRD), atomic force microscopy (AFM), secondary ion mass spectrometry (SIMS) and other techniques in the work presented in the thesis. Special attempt has been made to characterize the structure and magnetic properties at the interfaces in the thin film multilayers studied. Interface alloys have been formed by controlled annealing in several multilayers with binary elements viz. metal/metal and metal/semiconductor components. The kinetics of alloy formation at the interfaces at microscopic length scales in multilayer samples by controlled annealing has been studied in detail [10,14]. Determination of exact alloy stoichiometry, diffusion constant and growth of first phase at the interfaces have been attempted using reflectometry techniques.

1.2 Deposition techniques

Quality of the film is strongly affected by many physical parameters. Some of the important parameters are structure of the substrate vis-à-vis structure of the deposited film, surface energy of the respective components and propagation of roughness at the interfaces [8]. Quality of thin films also strongly depends on the deposition technique used. The films used in the series of studies presented in this thesis have been deposited using ion beam sputtering and DC/RF magnetron sputtering.

Chapter1: Introduction

Using various growth techniques, one can create artificial multilayers with interfaces between dissimilar materials, which otherwise may not occur in nature, with control at atomic/molecular level [17]. Thin film deposition techniques are of considerable interest for creating new materials. There are several methods for preparation of thin films which are broadly classified as physical vapor deposition (PVD) and chemical vapor deposition (CVD). Among several PVD methods, we will focus on the sputtering technique in details here, since the films used in the present work were deposited using this technique. The author has carried out optimization of a DC/RF magnetron sputtering system as a part of the work reported in the thesis [18].

Sputtering involves ejection of material atoms from a "target" that is a source onto a "substrate" (quite often silicon wafer) by momentum transfer between the sputter gas and target atoms. A sputtering gas (usually Ar) is used to strike a plasma at the source/target by application of voltage. The ejected particles are ionized and ballistically move towards the substrate. The process deals with energy of few tens of eV and hence adhesion of the film is better in sputtering. Unlike other evaporation methods, sputtered films contain less defects, they have lower interface roughness, and are highly dense due to higher energy of sputtered particles. Sputtering can be broadly divided into two types, DC and RF and these techniques, combined with magnetic field on the target constitute DC magnetron or RF magnetron sputtering [19]. Details of this technique and optimization of different deposition parameters for various films deposited during the present work will be described in chapter 2 of the thesis.

Involvement of many parameters such as sputter gas pressure (Ar), deposition rate, base vacuum etc. makes sputter deposition a complex process, but also allow a large degree of control over the growth and microstructure of the film [17-19]. Optimisation of a DC/RF

magnetron sputtering unit installed in SSPD, BARC, INDIA will be discussed in detail in chapter 2.

1.3 Characterization methods

Several techniques have been adopted for characterization of thin films and multilayers in the present thesis. XRR and PNR are used as the primary characterization techniques for physical and magnetic characterization of samples. XRD has been used to confirm crystallinity of the samples. XRD has been used to identify possible phases and growth of grain in our thin film samples. SIMS was used to confirm the periodicity of the multilayer samples in some of our studies. Superconducting Quantum Interference Device (SQUID) Magnetometer were used for determining the magnetic hysteresis loop for the samples to support the findings of polarized neutron reflectometry. AFM also has been used in some cases in order to determine surface morphology of the samples.

1.3.1 Polarized Neutron and X-Ray Reflectometry (PNR and XRR)

Neutron and X-ray reflectometry have emerged in recent years as two powerful non-destructive tools for investigating the structures of surfaces and buried interfaces with depth resolutions in sub nm range. [15,16]. X-ray being an electromagnetic radiation interacts with electrons only and can reveal the electron scattering length density profile (ESLD). The neutron primarily interacts with the atomic nuclei and neutron reflectometry gives nuclear scattering length density (NSLD), which is complementary to ESLD obtained from XRR. Neutrons are electrically neutral, and can penetrate matter more deeply ; and hence are valuable probes for buried layers and interfaces [20]. In addition, neutrons carry a magnetic moment of $-1.91 \mu_n$ that interacts with the atomic magnetic

moment present in the system (due to the unpaired electrons), capable of giving the magnetic depth profile of the system along with the nuclear density profile.

There are two possible types of reflections from a surface: (a) specular reflection, when the angle of reflection is equal to the angle of incidence and (b) off-specular reflection, where the above equality is not maintained. Specifically, specular reflectivity can be analyzed to reconstruct laterally averaged compositional depth profile along the normal to the surface of a film. Off-specular reflectivity provides height-height in-plane correlation function at an interface. This allows one to quantify interface morphology. Specular neutron reflectivity in un-polarized mode can be used to determine the structural parameters of thin films viz. individual layer thickness, interface roughness and the density of the layers. Same result can be obtained from XRR. Whereas in PNR we can obtain the additional information of magnetic scattering length density (MSLD) profile for each magnetic layer. In the present thesis we have used XRR and PNR in specular mode only.

Specular reflectivity from a sample is measured as a function of the wave vector transfer $Q = 4\pi \sin(\theta)/\lambda$, where 'θ' is the incident angle on the film and 'λ' is the wavelength of the incident radiation. Typical reflectivity profiles are shown in Fig. 1.2. Fig. 1.2 (a) shows XRR from a film of infinite thickness, silicon (Si) substrate in this instance and Fig. 1.2(b) shows the XRR of a film of finite thickness $\sim 200\text{\AA}$ Ge layer on Si substrate [Si/Ge(200 Å)]. The oscillations observed in the reflectometry pattern of Fig 1.2 (b) are due to finite thickness of the film and are called Kiessig oscillations [21]. The spacing between two Kiessig oscillations is inversely proportional to the thickness of the film ($\sim 2\pi/d$, where d= film thickness). Higher the thickness of the film, closer are the oscillations. From fits to the reflectivity pattern one can estimate thickness of films with angstrom resolution, which is not possible by most other technique.

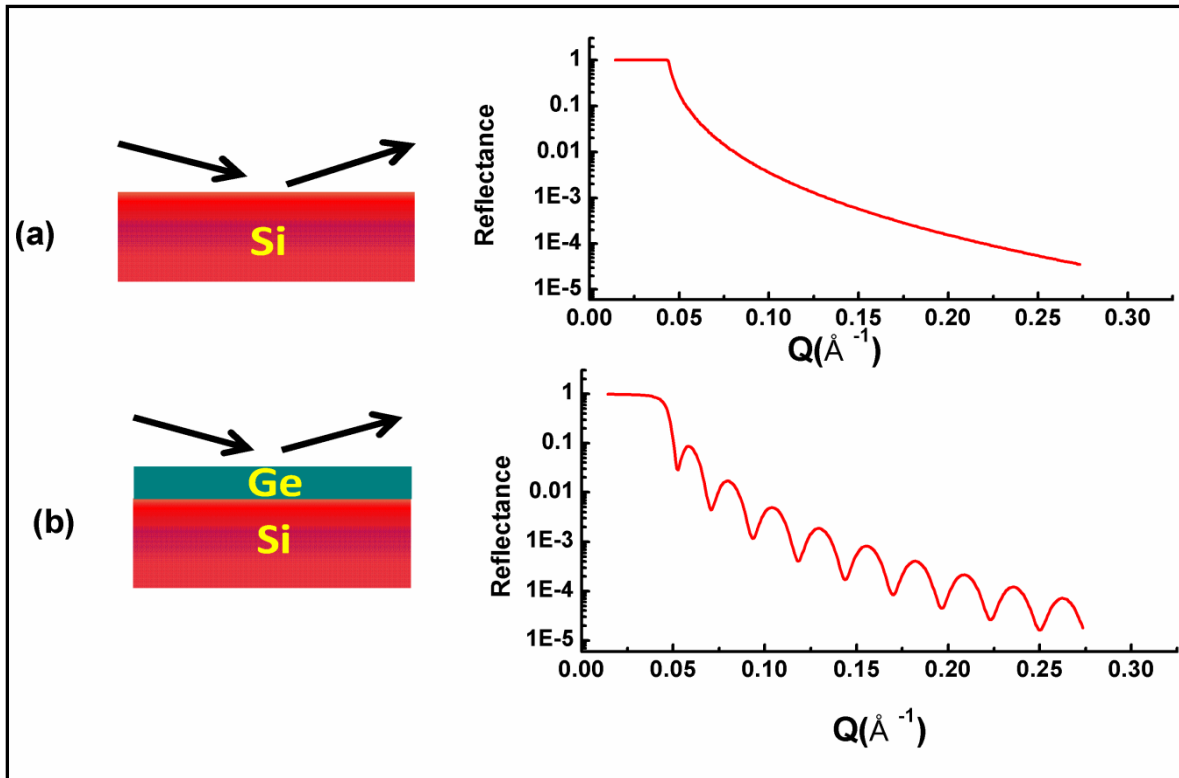


Figure 1.2: XRR profile of (a) an infinitely thick Si layer and (b) from Ge layer [Ge Si (substrate)/Ge(200 Å)].

Both XRR and PNR techniques are based on the principle of reflection from a surface. The SLD variation in the medium is related to the contrast in refractive index between layers of a film or medium. If ‘ k ’ is the wave vector of the incident radiation in vacuum then the wave vector of the radiation inside a material of refractive index ‘ n ’ is nk . A generic expression for refractive index for neutrons and x-rays can be given by:

$$n = 1 - (\delta - i\beta) \dots\dots\dots(1.1)$$

‘ δ ’ is the deviation from unity and $\sim 10^{-5}$ for x-rays and $\sim 10^{-6}$ for neutrons. Since the deviation of refractive index from unity is quite small, total reflection of neutrons and x-rays occur at grazing incidences in the range tens of arc-minutes, which makes it experimentally challenging. For most of the samples studied, neutrons absorption

coefficient ' β ' is negligibly small, hence can be neglected. In case of XRR refractive index of a medium depends on the ESLD of the medium. For neutrons refractive index of the same medium depends on the NSLD. In case of PNR we need to add or subtract the MSLD with the NSLD depending on the relative orientation of the neutron polarization with respect to the sample magnetization direction. PNR and XRR together form an excellent couple of complementary tools for characterization of thin films [10,11] .

Un-polarized and polarized neutron reflectivity from a Ni-Al multilayer comprising 10 Ni/Al bilayers on a Si single crystal substrate with nominal structure: Si (substrate) / [Al(25Å)/Ni(50Å)] \times 10 , is given in Fig 1.3. The difference between the R^+ and R^- profiles in PNR is due to magnetic moment of the Ni layers in this sample. The Bragg peaks are the signature of periodic bilayers in the multilayer sample. Information about the structural parameters like thickness, roughness, density was obtained from analysis of both the reflectometry data (XRR, PNR) and the magnetization profile was obtained from PNR data [22]. Using the density profiles obtained from XRR and PNR together one can obtain the exact stoichiometry of the alloy formed at an interface in case of binary systems [10,11]. We have used XRR and PNR together for obtaining interface alloy composition extensively in the present thesis [10-14]. PNR was carried out at the reflectometer beam line in DHURVA reactor, BARC, India with an incident wave length of 2.5 Å. Details of XRR and PNR technique will be described in chapter.3 in the present thesis.

1.4 Multilayer films: Nickel-Aluminides, Nickel-Germanides

Transition metal aluminides, especially Ni aluminides, have been recognized as possible candidates for a variety of high-temperature structural applications. They are suitable to operate well beyond the operating temperatures of conventional materials due to their excellent oxidation and corrosion resistant properties [23-25]. Ni is hard, ductile,

ferromagnetic and a good conductor of heat and electricity [26]. It also has excellent corrosion-resistant properties.

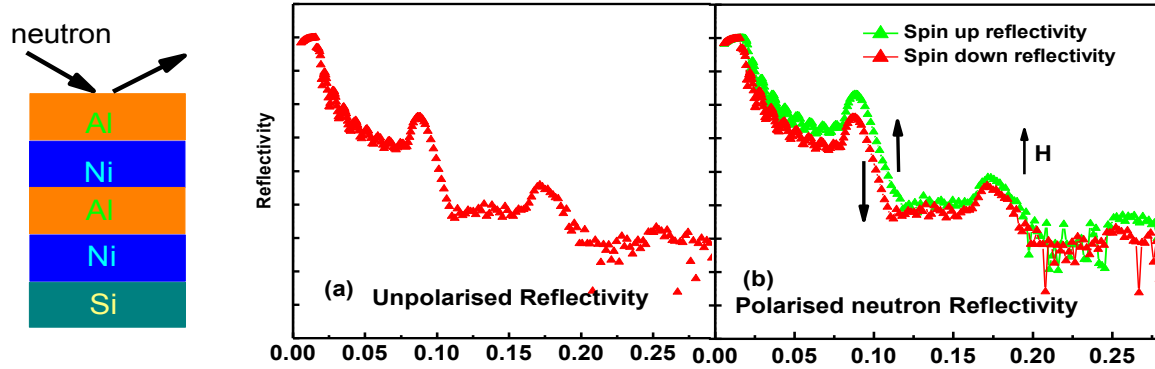


Figure 1.3: (a) Unpolarised and (b) polarised neutron reflectometry from a Ni-Al multilayer [Si (substrate) / [Al(25Å)/Ni(50Å)] \times 10].

Aluminum on the other hand is light, non-magnetic and fairly ductile [27]. With the advent of several deposition techniques these days, we can combine both elements in a desired manner to produce specific alloys having ordered crystal structure with a combination of desirable physical and mechanical properties viz. light weight, good mechanical strength, high hardness, and high melting point [24,25]. Nickel aluminides are heavily used in the field of aeronautics and automobiles due to their suitable properties mentioned above [28,29]. The phase diagram of Ni-Al binary system has been studied extensively both experimentally as well as theoretically [30]. There are several stable nickel aluminides NiAl_3 , NiAl , Al_3Ni_2 , Ni_3Al according to their equilibrium phase diagram [31]. Hence Ni/Al system offers an excellent platform to study the kinetics of first phase formation at the interface. Details of interface alloy formation have been studied in several ultra-thin multilayer films of Ni/Al using PNR and XRR in the present thesis [10,14]. Surface energy effect on the interfaces has been discussed in detail for Ni-Al systems. The kinetics of interface alloy formation on annealing, their composition and

dependence on initial stoichiometry have been studied with nanometer resolution. We have obtained a kinetic length scale which dictates the local density responsible for stoichiometry of the alloy phase [10]. Results of the studies carried out on Ni/Al multilayer samples have been described in chapter 4 of the thesis.

Several magnetic hetero-structures such as semiconductors/ferromagnets, and ferromagnets/antiferromagnets exhibit properties required for applications in microelectronics [32,33]. These combinations acquire properties that are important in the field of magnetism, nanotechnology and semiconductor technology. Nickel Germanides are one of the important class among the transition metal Germanides [34]. They are suitable candidates for inter-connects in MOSFET applications, as they form low resistive phases on annealing [34-36]. In the present thesis low-resistance Ni-Germanide phase has been formed at the interfaces of a Ni/Ge multilayer film by controlled annealing and has been characterized for its composition, transport and magnetic properties. The results are discussed in chapter 5. The Ni/Ge systems were prepared by DC/RF magnetron sputtering on a deposition unit built in-house (details described in chapter 2).

1.5 Diffusion in thin films

When two miscible systems (solid, liquid, gas) are in intimate contact with one another with a difference in their concentration, diffusion takes place across the interface between the two systems due to random thermal motion of the components. Diffusion is basically net movement of a substance (e.g., atoms, ions or molecules) from a region of higher concentration to a region of lower concentration. This also can be referred to as the movement of a substance down a concentration gradient that leads to equalization of concentration. The notion of diffusion and its physical meaning can be understood by the phenomenological approach in Fick's laws of diffusion and their mathematical consequences [37].

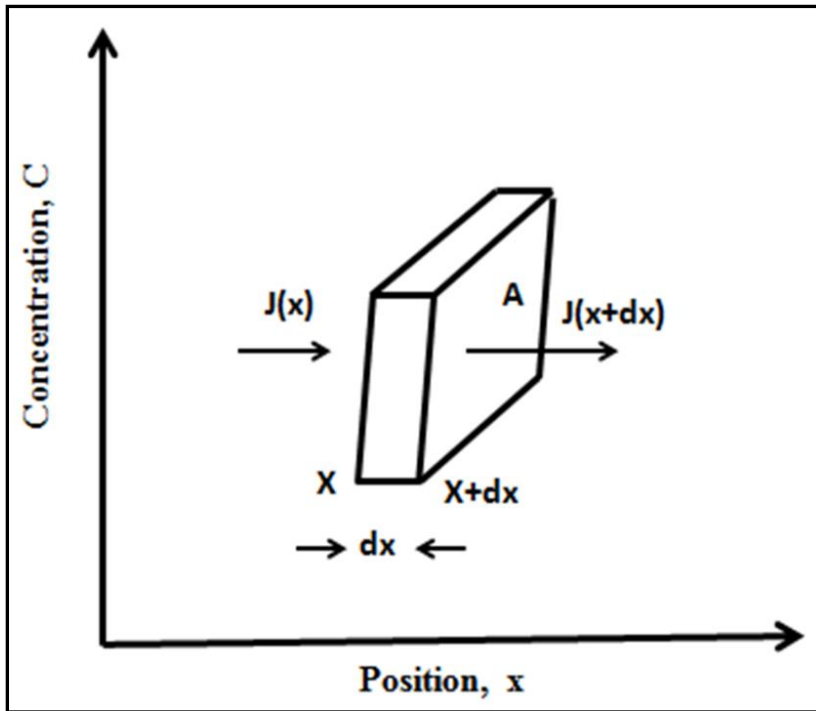


Figure 1.4: Flux across area 'A' due to particle flux $J(x)$

1.5.1 Fick's laws of diffusion

Consider the flux of diffusing particles in one dimension (x-direction) as shown in Fig.1.4. Considering the material flux is directly proportional to the concentration gradient, we can write for the particle flux 'J' in one dimension (x) as:

$$J(x) = -D \frac{dC(x)}{dx} \dots\dots\dots(1.2)$$

This is Fick's first law of diffusion, Where $J(x)$ = The diffusion flux (amount of substance transported per unit area per unit sec) at position 'x', 'D' is the diffusion constant or diffusivity, 'C(x)' is concentration per unit volume, where 'x' is the position coordinate. The negative (-) sign implies that the diffusion flux is in opposite direction to the concentration gradient. We define the local concentration and diffusion flux (through unit area, 'A') at position 'x' and time 't' as: $C(x)$ and $J(x)$ respectively. In diffusion process the number of diffusing particles are conserved. Hence Fick's law obeys equation

of continuity. If one considers spatial dependence of particle flux $J(x)$ [Fig.1.4] and change in concentration $dC(x)$, the difference of particles entering and leaving a region, one can write:

$$dC(x) = \frac{J(x) - (J(x + dx))}{A dx} A dt$$

where, $J(x + dx) = J(x) + \frac{dJ(x)}{dx} dx$

This implies;
$$\frac{dC(x,t)}{dt} = - \frac{dJ(x)}{dx}$$

Putting Fick's first law (1.2) in the above equation:

$$\frac{\partial C(x,t)}{\partial t} = D \frac{\partial^2 C}{\partial x^2} \dots\dots\dots (1.3)$$

This second order partial differential equation is Fick's second law in one dimension. For three dimensional diffusion (3D), it can be generalized as:

$$\frac{\partial C}{\partial t} = D \nabla^2 C$$

At steady state (equilibrium) $\frac{\partial C(x,t)}{\partial t} = 0$, leading to Fick's first law. This is a special case of Fick's second law in case of steady state diffusion.

Let's consider the solution of equation (1.2) using Fourier Transform as:

$$C(x,t) = \int_{-\infty}^{\infty} C(k,t) e^{ikx} dk \dots\dots\dots (1.4)$$

Putting (1.4) in (1.3) we can get:

$$C(k,t) = C_0 e^{-Dk^2 t} \dots\dots\dots (1.5)$$

Where C_0 is a constant. At $t=0$, $C(k,t)=C(k,0)$, So (1.5) will be:

$$C(k,t) = C(k,0) e^{-Dk^2 t} \dots\dots\dots (1.6)$$

For diffusion from a point source at t=0;

$$C(x,0) = N\delta(x) \dots\dots\dots(1.7)$$

Here the diffusing species (diffusant) is deposited at the plane x=0 and allowed to spread for time, t >0.

‘N’ denotes the number of diffusing particles per unit area and

$$\int_0^{\infty} C(x,t)dx = N = \text{Constant.}$$

Then we can write, $C(k,0) = \frac{1}{2\pi} \int_{-\infty}^{\infty} C(x,0)e^{-ikx} dx = \frac{N}{2\pi} \dots\dots\dots(1.8)$

Putting (1.6) and (1.8) in (1.4):

$$C(x,t) = \int_{-\infty}^{\infty} \frac{N}{2\pi} e^{-Dk^2t} e^{ikx} dk$$

Using Gamma Function we can write:

$$\boxed{C(x,t) = \frac{N}{\sqrt{4\pi Dt}} e^{-x^2/4Dt} \dots\dots\dots(1.9)}$$

This is the solution of one dimensional (1D) Fick’s second law when the diffusing species is allowed to spread into two material bodies occupying the half space $0 < x < \infty$ and $-\infty < x < 0$ which have equal and constant diffusivity or called a sandwich geometry solution [38].

For thin film geometry the solution will be :

$$C(x,t) = \frac{N}{\sqrt{\pi Dt}} e^{-x^2/4Dt} \dots\dots\dots(1.10)$$

The quantity $2\sqrt{Dt}$ is a characteristic *diffusion length* and can be termed as L_d .

This solution $C(x,t)$ can be compared with the scattering amplitude in case of a reflectivity measurement. A solution in Q -space can be obtained by taking a FT over 'x' of above equation:

$$C(Q,t) = \frac{N}{\sqrt{4\pi Dt}} e^{-Q^2Dt} \dots\dots\dots(1.11)$$

Where Q = the momentum transfer vector = $2n\pi/d$, and 'n' is the order of Bragg peak and 'd' is thickness of periodicity and is the bilayer thickness in case of a multilayer system.

1.5.2 Diffusion constant from reflectometry experiments

In a specular reflectivity experiment with a multilayer sample comprising periodic bilayers, the ideal reflectivity profile will show the Bragg peaks due to the periodicity of the bilayers as shown in Fig. 1.5(a). If one anneals the multilayer sample at a raised temperature, diffusion takes place across the boundary (interface) of the bilayers and there will be formation of alloy layers at the interfaces (as shown in inset of Fig. 1.5(a)). This will cause loss in contrast between respective layers and the corresponding intensity of the Bragg peaks in the reflectivity pattern will diminish as shown in the figure. In a reflectivity experiment one measures reflected intensity 'I' as a function of momentum transfer 'Q'. This intensity is directly proportional to the Fourier transform of the concentration, 'C(Q, t)' in equation (1.11). If we substitute the value of 'Q' at a Bragg peak by $\frac{2n\pi}{d}$, where 'd' is the bilayer thickness in a periodic multilayer of two components, the following relationship can be obtained from equation (1.11) that relates the intensities of reflected beams at the Bragg peak positions before and after annealing.

$$I(Q, t) = I(0) \exp\left(-\frac{8n^2\pi^2 D}{d^2} t\right) \dots\dots\dots(1.12)$$

Where $I(0)$ is reflected intensity before annealing.

This is 1D solution of Fick's law for thin films in Q-space that we routinely used to obtain diffusion constant in our reflectivity measurements [10,11]. The decrease in Bragg peak intensity as a signature of diffusion due to annealing and its atomistic picture is shown in Fig. 1.5 (a) and (b) respectively. Using the above equation we can find the diffusivity (D) and the diffusion length (L_d) for a system from the reduced Bragg peak intensity [10,14]. The diffusion studies for Ni-Al and Ni-Ge systems have been discussed in detail in chapter 4 and chapter 5 respectively.

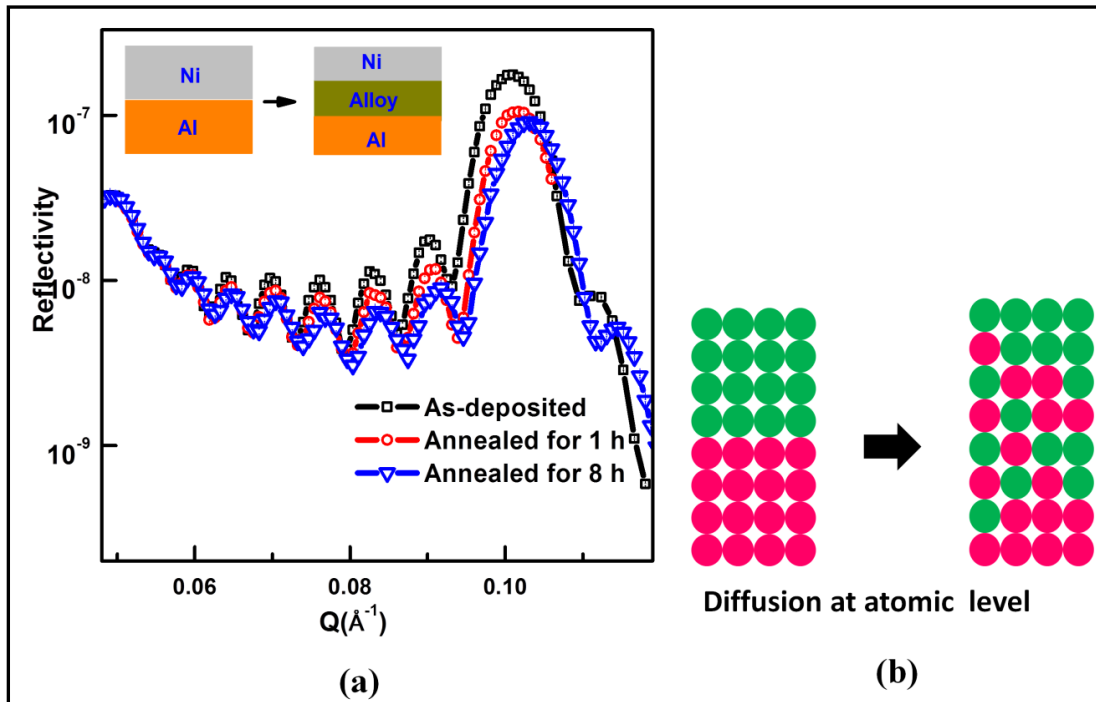


Figure 1.5: (a) Reduction in Bragg peak intensity due to diffusion (inset shows interface alloy layer formation due to diffusion) (b) diffusion at atomic level.

Chapter 2: Thin Film Deposition

- 2.1 Introduction
- 2.2 Sputtering
- 2.3 Advantage of Sputtering over other deposition methods
 - 2.3.1 DC/RF Sputtering
 - 2.3.2 Magnetron Sputtering
- 2.4 Factors Affecting Sputtering
 - 2.4.1 Base vacuum
 - 2.4.2 Target substrate geometry
 - 2.4.3 Sputter gas pressure
 - 2.4.4 Target/Substrate Temperature
- 2.5 Optimization of a DC/RF magnetron sputtering unit
 - 2.5.1 Description of the system
 - 2.5.2 Steps for Deposition
 - 2.5.3 Samples prepared
 - 2.5.3.1 Single Ni film
 - 2.5.3.2 Multilayer film of Cu-Ti
 - 2.5.3.3 Ge films: semiconducting layers

2.1 Introduction

Often thin films are artificial hetero-structures deposited on a substrate using one of several deposition techniques. Thin film properties are strongly dependent on the method of deposition, substrate material, substrate temperature, deposition rate and the background gas pressure [39,40]. Various applications in modern technology demand specific properties in thin films viz. adhesion, thermal stability, low porosity, desirable stoichiometry etc. Such properties are strongly dependant on the deposition methods. There are several methods for preparation of thin films and multilayer [17,19]. Knowledge of various growth procedures enables us to deposit ultra-thin films with control at atomic/molecular level and to deposit thin films of desired thickness/stoichiometry that satisfy required functionality. It is of importance to understand and optimize the deposition procedure to produce good quality thin

films. Improved quality of thin films, surfaces and interfaces have made remarkable advances in thin film based technology [41].

Thin film deposition techniques may be broadly classified as physical vapor deposition (PVD) and chemical vapor deposition (CVD) techniques [17]. A classification table for deposition methods is given below in Fig.2.1.

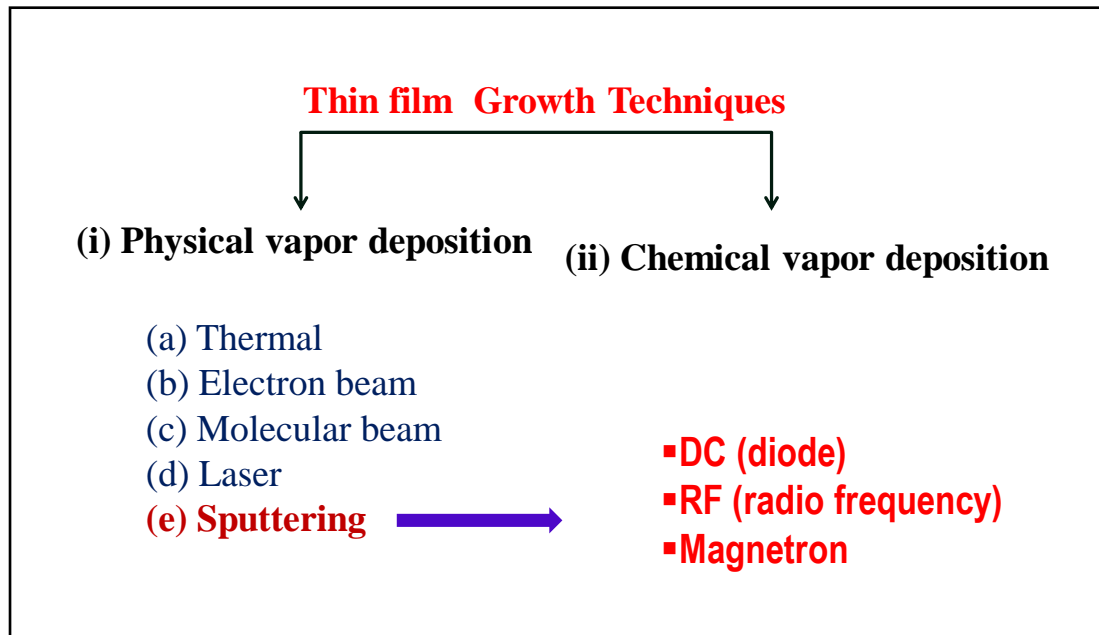


Figure 2.1: Classification of thin film deposition methods.

PVD includes a variety of vacuum deposition methods to deposit thin films by the condensation of a vaporized form of the desired film material onto the substrate. Among the PVD methods, sputtering has been focused upon in the present thesis, since all the samples studied in the thesis were deposited using this technique. Although there are many variants of the technique, sputtering can again be broadly divided into DC magnetron and RF magnetron types. In magnetron sputtering, magnets are used behind the target assembly to provide a closed drift path of electric and magnetic field for electrons to enhance the probability of ionization [17,42]. Optimization of a DC/RF magnetron sputtering system installed in SSPD, BARC, INDIA has been discussed in detail in this chapter [18].

2.2 Sputtering

When a surface is bombarded with high velocity positive ions, it is possible to cause ejection of the surface atoms. This process of ejecting atoms from the surface by bombardment of positive ions (usually inert gas ions), by momentum transfer process between the sputter gas and target atoms is commonly known as sputtering (cathode sputtering) [19]. Argon is commonly used as the sputtering gas. The ejected atoms can be made to condense on a substrate at an optimal distance from the target to form a film. Apart from the neutral atoms, charged atoms and electrons are also emitted from the surface. The sputtering yield ‘S’ (number of atoms ejected from the target surface per incident ion) depends on the target material composition, binding energy, characteristics of the incident ion and the experimental geometry. It also depends on the voltage and current (sputter power) at which sputtering takes place.

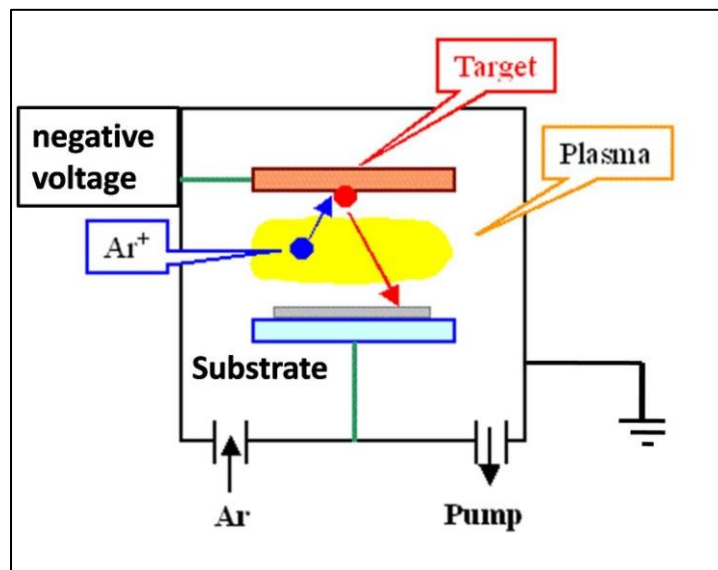


Figure 2.2: Schematic of Sputtering

Schematic of a conventional sputtering process is given in Fig 2.2. The target is connected to a negative voltage supply (cathode) and the substrate holder along with the chamber maintained at a ground potential acts as the anode and faces the target during sputtering. The

plasma is maintained between the target and the substrate. The process deals with energy of few tens of eV and hence adhesion of the film on substrate is better in sputtering.

2.3 Advantages of sputtering over other deposition methods

In sputtering, the entire surface of the target is the source, unlike evaporation process where a point (where electron beam hits) on the target is the source. The surface source implies a higher coverage area during deposition as compared to other evaporation techniques [19]. The deposition process in sputtering is not purely ballistic. In sputtering the evaporants bombard the substrate surface, rearrange themselves and then condense on the substrate. Higher kinetic energy of the sputtered particles (~ tens of eV) giving rise to better adhesion to the substrate. Some of the main advantages of sputtering as a thin film deposition technique are due to high kinetic energy of the sputtered atoms, causing their re-distribution on the substrate, leading to (a) high uniformity, density and interface roughness of the deposited film (b) deposition over large surface area [19]. By incorporating target cooling provision in sputtering, higher melting point elements can be deposited. With a better understanding of the sputtering processes, it has become one of the versatile methods for preparing high quality thin solid films of any material.

2.3.1 DC/RF sputtering

The sputtering process is classified as DC or RF depending on the type of power supply used. DC sputtering is mainly used to deposit metals. In case of insulators after the ions strike the surface, their charge will remain localized and with passage of time positive charge will build up on the target, making it unfeasible to further bombard the surface. This can be prevented by bombarding the insulator by both positive ions and electrons simultaneously [19]. That is done by applying a RF potential to the target. The RF potential provide sufficient energy to the electrons oscillating in the alternating field to cause ionizing

collisions, and a self-sustained discharge is maintained. As electrons have higher mobility compared to ions, more electrons will reach the insulating target surface during the positive half cycle than the positive ions during the negative half cycle. Hence the target will be self biased negatively. This repels the electrons from the vicinity of the target and forms a sheath enriched in positive ions in front the target surface. These ions bombard the target and sputtering is achieved. At a frequency less than 10 kHz such an ion sheath will not be formed. Typical RF frequencies are employed in the range from 5 to 30 MHz. However, 13.56 MHz is the most general frequency used for rf sputtering [17]. The most important difference between RF and DC systems is that the former requires an impedance matching network between the power supply and sputtering chamber [43]. The main job of this network is to provide optimal matching of the load to the RF generator, so that sufficient power can be delivered to the sputtering chamber.

2.3.2 Magnetron Sputtering

Sputtering sources often employ magnetrons that utilize strong magnetic (\vec{B}) fields to confine charged plasma particles close to the surface of the sputter target in order to increase the sputter yield. In a magnetic field, electrons follow helical paths around magnetic field lines. This causes an increase in the effective path length, causing more ionizing collisions with gaseous neutrals near the target surface. The sputtered atoms are mostly neutral and also much heavier and are unaffected by the magnetic trap. The sputter gas is typically an inert gas such as Ar. The Ar ions created as a result of collisions with electrons lead to a higher deposition rate. It also means that the plasma can be sustained at a lower Ar pressure. A schematic of the target and magnetic field arrangement in a typical magnetron sputtering set up is given in Fig 2.3. The $E \times B$ drift path is shown in the figure, where the electrons are confined to increase the sputter yield in a toroidal path generated by the magnets placed

behind the target. An electron launched by the target is affected by the component of magnetic field bending towards the target surface (magnetron component) and finally returns, after completion of the magnetic circuit [17]. As the target material is depleted due to sputtering, an annular erosion profile may appear on the surface of the target.

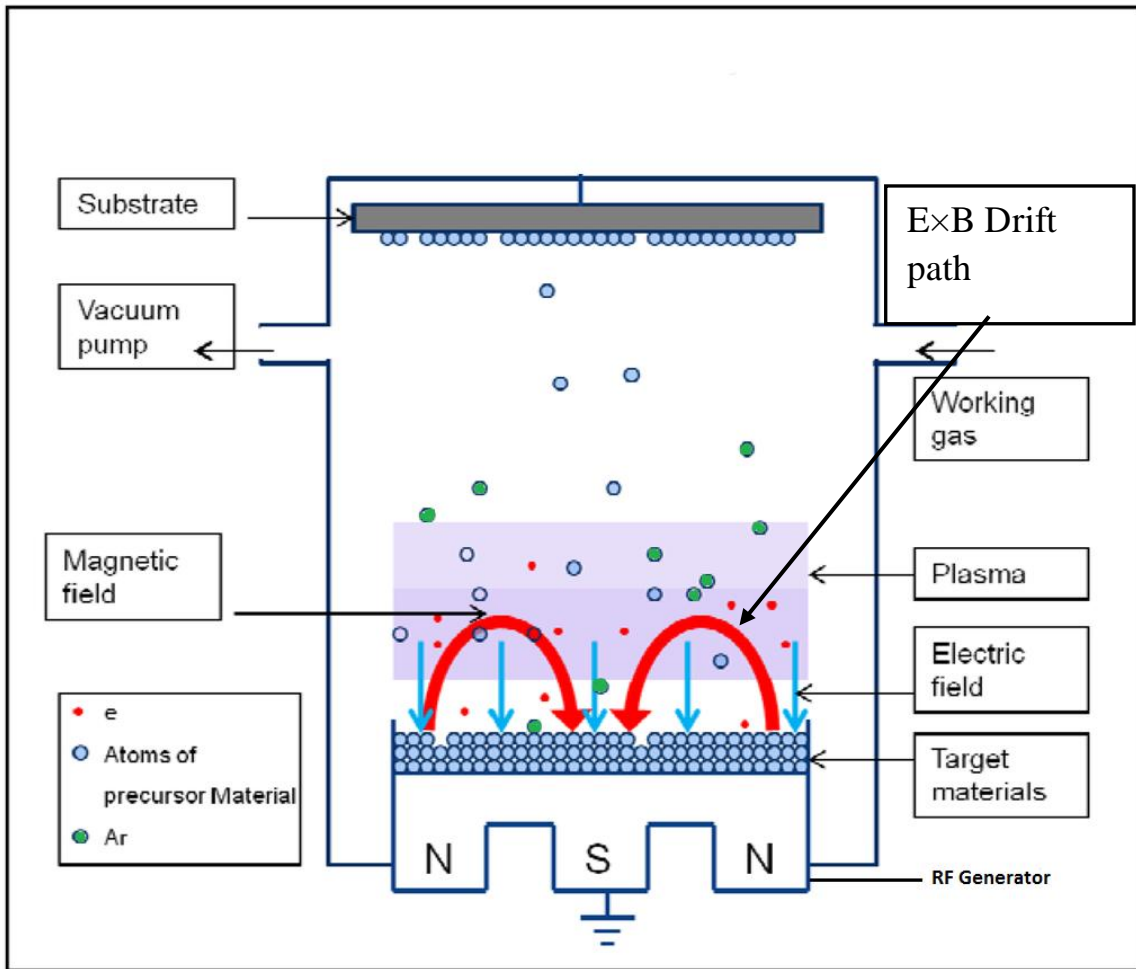


Figure 2.3: Schematic showing the magnetic field and target assembly in a RF magnetron sputtering set up.

In RF sputtering electrons present at the space between substrate and target (inter electrode space) do not get enough energy by the RF field to cause ionisation. But if we apply a magnetic field parallel to the RF field, it will constrain the electrons without being lost to the flow, thus improving the RF discharge efficiency. So a magnetic field is more important

for a RF sputtering than in a DC sputtering [19]. The work presented in chapter 5 of this thesis on Ni-Ge multilayer was prepared by DC/RF magnetron sputtering.

2.4 Parameters affecting sputtering

Sputtering involves many parameters that affect the deposition process such as: base vacuum, sputter gas pressure during deposition (here argon), sputter power, target and substrate temperature etc. The microstructure of the film or its quality which includes surface roughness, adhesion, impurity, density of the film produced by sputtering process is a result of interplay of the above parameters [44]. Contribution of such a large number of parameters makes the process complex but also provides a large degree of control over the film growth process, if optimized properly. Apart from the above parameters the deposition geometry, that is the relative orientation of the target and the substrate, also plays an important role that affects the thin film growth process. Some of the important factors that are important for sputtering are discussed below.

2.4.1 Base Vacuum

The chemical purity of evaporated films depends on the nature and level of impurities that are initially present in the sputtering chamber, in the source (target) or contaminates from the support materials during deposition. Also, it may originate from the residual gases present in the vacuum system. Hence it is necessary to obtain a good base vacuum prior to thin film deposition. Sometimes sputtering system is also thoroughly baked for improving base vacuum.

2.4.2 Target substrate geometry

The target-substrate geometry, is an important factor that influences the ultimate film uniformity. This includes the orientation of the source (target) and substrate and their

distance of separation. In sputtering, apart from target atoms there are also electrons emitted from the target (cathode) by ion bombardment, and these are accelerated towards the substrate where the electrons collide with the gas atoms. These electrons help in sustaining the plasma by causing ionization as the ionized gas atoms in turn may bombard the target producing the secondary electrons. If the gas pressure is too low or the cathode (target) and anode (substrate) distance is too small then the secondary electrons cannot undergo sufficient ionizing collisions before hitting the substrate. On the other hand, if the gas pressure is too high or the distance between the target and substrate is too large then the ions generated are slowed down by inelastic collisions and hence when they strike the target, they will not have enough energy to cause sufficient secondary electrons. Hence the target substrate distance has to be optimized for better deposition. As sputtering is a line of sight deposition, hence substrate rotation may also help to ensure a uniform deposition over an area.

2.4.3 Sputter gas pressure

Deposition of the target atoms on to the substrate depends on its surface binding energy [45]. The film deposition rate also depends on the sputtering pressure and power. At low pressures, the mean-free of electron between collisions is large. Hence, ionization efficiencies are low, and self-sustained discharges cannot be maintained below a certain pressure ($\sim 10^{-4}$ mbar). On the other hand, as the pressure is increased at a fixed voltage, the electron mean-free path is decreased, more ions are generated, and larger current flow occurs. But if the pressure is too high, the sputtered atoms undergo increased collision leading to scattering hence they move diffusively towards the substrate and are not efficiently deposited [19,46]. So there should be an optimum pressure for highest achievable deposition rate. A typical plot of deposition rate/sputter efficiency vs. residual gas pressure is shown in Fig.2.4. In case of magnetron

sputtering we can increase the number of Ar ions without increasing the number of Ar neutrals so that one can work at relatively lower pressure $\leq 15 \times 10^{-3}$ mbar.

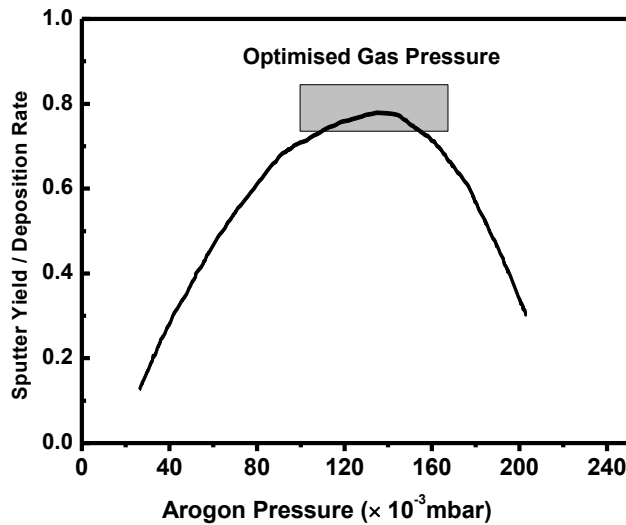


Figure 2.4: Sputter Yield/ Deposition rate as a function of sputter gas pressure (Ar)

2.4.4 Target/Substrate Temperature

Sputtering is a low temperature process and small fraction ($\sim 1\%$) of total applied power is consumed in ejecting the sputtered particles and secondary electrons. A considerable amount of energy is dissipated at the cathode by the ions that strike it, and the cathode gets hot. The rise of temperature depends on the sputtering conditions. Though the sputter yield increases with the temperature, but it should not go beyond a tolerable limit which may cause problems of out gassing. Hence it is necessary to cool the target during sputtering [19]. The substrate temperature also affects properties of thin films like adhesion, uniformity surface roughness etc. Hence substrate temperature is also an important parameter in thin film deposition, which one can vary for specific films.

2.5 Optimization of a DC/RF magnetron sputtering unit

2.5.1 Description of the system

We have developed a DC/RF magnetron sputtering system with 3 targets for preparing high quality thin films with large area (~ 75 mm diameter). Using these targets one can deposit multilayer thin films using multiple targets or alloy films by co-sputtering [47-49]. Schematic of the cross-sectional view of the stainless steel vacuum chamber with various components is shown in Fig. 2.5.

The system is a spherical chamber with diameter ~ 450 mm with three sputter guns in a confocal arrangement. These guns have an in situ tilt ($\pm 15^\circ$) facility, and are arranged at the bottom of the chamber in a confocal geometry at 60° to each other. In this arrangement all three sputter guns are facing towards the substrate and this facilitates deposition of three components together for forming alloys on the substrate. This process is called co-sputtering.

In the present deposition system, two sputter guns are operational under DC magnetron sputtering for metallic targets and one gun is used for RF sputtering to deposit insulators/semiconductors. Two 1.5 kW D.C. power supplies are used for the DC sputter guns. A 300W (13.56 MHz) Hüttinger RF power supply with an impedance matching network is used for the RF sputtering. Targets of 3 inch diameter are used so that sputtering can yield uniform deposition over substrates of diameter 3 to 4 inch. Each sputter gun and the substrate holders are provided with their own shutters in order to isolate them when not in use. The pumping system consists of a turbo molecular pump (TMP) backed by a rotary pump. There is a throttle valve with adjustable opening between the deposition chamber and the vacuum system to maintain a dynamic vacuum in the chamber by balancing the evacuation rate and rate of Ar gas injection in the chamber.

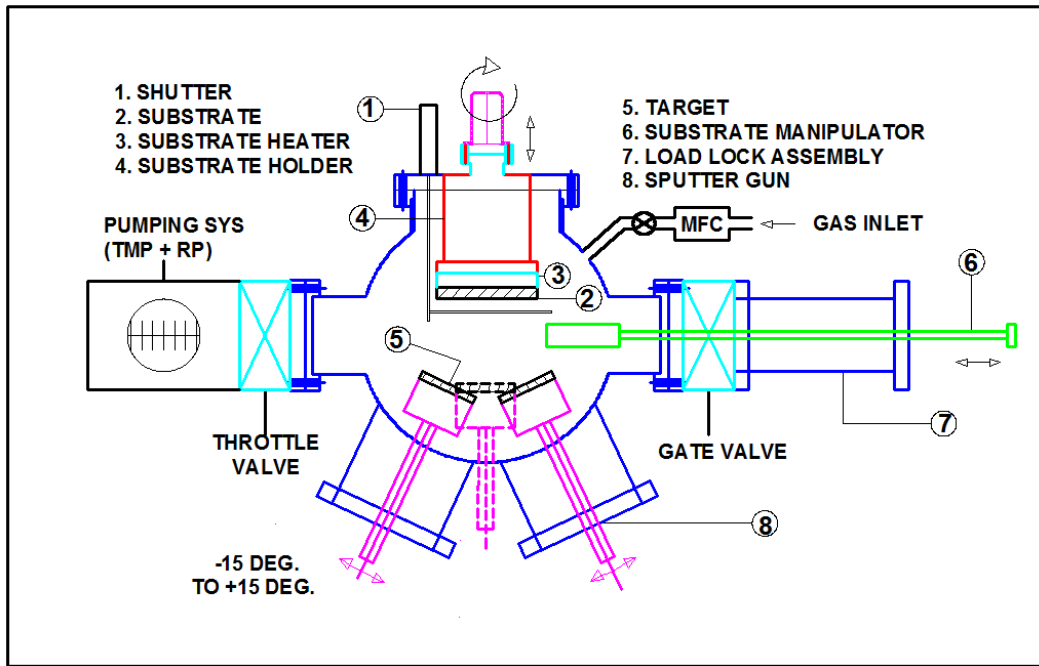


Figure 2.5: Cross-sectional schematic view of the D.C./RF magnetron sputtering system layout. The pumping port is actually positioned towards the rear in line with the central axis, but has been shown in the foreground here for clarity.

The substrate assembly can be translated vertically to adjust the target-substrate distance (TSD). TSD has been optimized for different targets to get maximum sputter yield and uniformity over large substrate area. Uniformity during deposition is also ensured by substrate rotation (1-4 rpm). Introduction of substrates through a load lock assembly minimizes contamination to the main chamber. Pure Ar gas is allowed in the chamber via a mass flow controller, after passing through a moisture bed of silica gel (SiO_2) and magnesium perchlorate ($\text{Mg}(\text{ClO}_4)_2$) crystals. The deposited films are characterized first by x-ray reflectivity (XRR) and x-ray diffraction (XRD) in order to obtain a quick check on the film structure and quality.

Ultimate vacuum achieved in the main chamber after systematic baking is $\sim 2.5 \times 10^{-7}$ mbar. The sputter rate of the elements are calibrated by a quartz crystal thickness monitor that can be inserted in the plasma, prior to actual film deposition on the substrates. The

sputter rate can be controlled by varying sputter voltage/current and Ar gas flow. Deposition parameters that were varied for optimal films are TSD, substrate rotation speed and the Ar flow rate. Depending upon energy of the sputtered atoms the target substrate distance (TSD) has been optimized for different targets in order to get better particle flux, uniformity and density of the films. The optimized sputtering parameters are given in Table 2.1 for the various deposited elements attempted on the system. A photograph of the sputtering chamber during deposition is given in Fig .2.6.

Table 2.1 Sputtering parameters of deposited systems:

Deposited Material	Voltage (volt)	Current (Amp)	Gas Flow Rate (SCCM)	Target-Substrate Distance(TSD) (in mm)	Working Vacuum with flow of Ar (in mbar)
Ni	300	0.06	40	88	$\sim 5.0 \times 10^{-3}$
Cu	360	0.3	40	79.52	$\sim 5.3 \times 10^{-3}$
Ti	401	0.51	40	79.52	$\sim 5.3 \times 10^{-3}$
Fe	515	0.03	40	57	$\sim 4.7 \times 10^{-2}$

2.5.2 Steps for deposition

The targets are cleaned and fixed on the respective sputter guns. The substrates (silicon wafers) are cleaned using three chemicals, tri-chloro ethylene, methanol and acetone and then loaded in to the deposition chamber load lock system. The system is pumped to get a good starting vacuum using the rotary and TMP ($\sim 2.5-5 \times 10^{-7}$ mbar). One can see the plasma on the respective targets. The color of the plasma indicates the target material being sputtered. The photograph shows the deposition of an alloy film with two targets being co-sputtered. Argon gas is introduced into the chamber through a mass flow controller, once the desired vacuum is achieved in the system. By partially closing the throttle valve that connects the chamber to the vacuum pumps one can maintain a steady pressure of Ar in the chamber during deposition.



Figure 2.6: Photograph of the sputtering unit at SSPD, BARC during deposition.

Voltage is applied to the sputter gun with the target material we want to deposit. The gas flow rate and the voltage are adjusted simultaneously to establish a stable plasma in the chamber. Prior to actual deposition, the plasma is deposited on the quartz crystal monitor up to certain thickness for a certain period to obtain the deposition rate under the given conditions. Taking this time as a reference one deposits a film on the substrate. During deposition, the substrate is rotated at a particular speed with the help of a DC motor attached to it to get a uniform deposition.

During the present thesis work optimization of the deposition parameters were carried for several targets of interest such as Nickel (Ni), Copper (Cu) and Titanium (Ti) targets using DC magnetron sputtering, and Germanium (Ge) by using RF sputtering [47-49] Thin films, bilayers and multilayers were deposited for various studies. Deposited films were primarily characterized by X-Ray reflectivity (XRR) [15] and X-Ray Diffraction (XRD) immediately after deposition to obtain quality of the deposited film. XRR gives structural information of the sample in terms of layer thickness, surface roughness and density of the film. Crystallographic information was obtained from XRD. In the following section details of optimization of the process parameters for some of the films deposited by the

sputtering system will be described. Detailed structural and magnetic characterization of a Ni/Ge multilayer is described in Chap.5 of present thesis.

2.5.3. Samples prepared

2.5.3.1 Single Ni film

We have deposited Ni films of several thicknesses with varying the deposition parameters. This was a case study to understand the role of the system parameters on the quality of the film deposited. A film was deposited with a base vacuum $\sim 5 \times 10^{-7}$ mbar and working vacuum $\sim 2 \times 10^{-2}$ mbar. The target substrate distance (TSD) was fixed at 84 mm. Sputtering power was 12.8W (V=427V, I=.03A). After deposition we carried out XRR on the film. From the XRR data we obtained thickness of the film $\sim 380 \text{ \AA}$ (shown in Fig. 2.7) [18]. But density of the film obtained was quite low $\sim 64\%$ of the bulk. Keissig oscillations [21] in the film were also absent indicating higher degree of roughness in this film. This may also be caused due to fluctuation in the average thickness of a film in lateral direction

To improve the film quality several steps were followed. First we improved the base vacuum by long baking of the deposition chamber. The sputter power was increased to 18W (V=300V, I=0.06A) expecting a film of higher density. The Ar pressure was set to $\sim 5 \times 10^{-3}$ mbar for deposition. Proceeding with these conditions, we have deposited another Ni film. The XRR profile is given in Fig. 2.8 (a). Thickness of the film obtained was 222 \AA with a surface roughness of 9 \AA . The well defined Keissig oscillations proves that the film has lower interface roughness. The density obtained was also $\sim 84\%$ of the bulk. Thus with improved base vacuum and increased sputter power we could obtain a better quality Ni film. We carried out XRD measurements on the sample shown in Fig. 2.8(b) Ni(111) and Ni(200) peaks were observed at two theta values of 44.3° and 51.2° respectively and it confirmed the crystalline nature of the film.

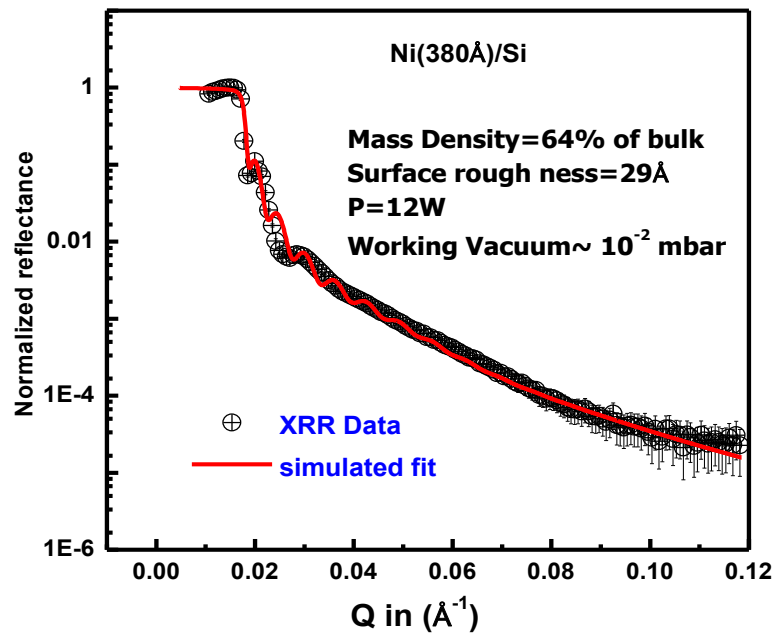


Figure 2.7: XRR profile of Ni(380Å)/Si.

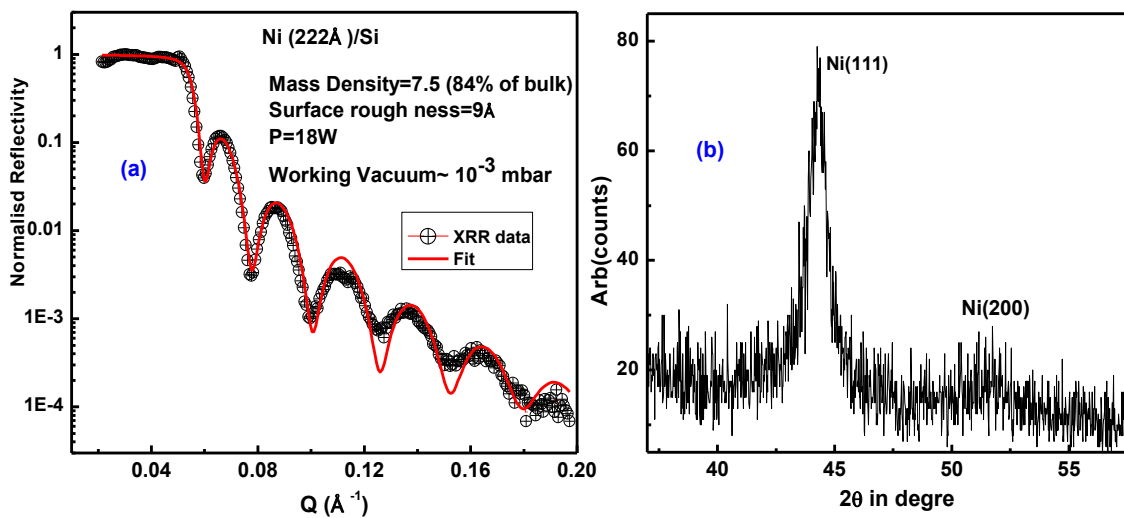


Figure 2.8: (a) XRR profile (b) XRD profile of the Ni film [Ni(222Å)/Si] deposited on Si substrate. The reflectivity data were fitted by a program using genetic algorithm and is discussed in detail in chapter 3.

2.5.3.2 Multilayer film of Cu-Ti

Copper-Titanium alloys are of great importance in various technical applications due to their suitable properties like higher conductivity, low resistance and higher mechanical strength

[50]. The interface quality significantly affected by the film deposition process and plays an important role in determination of the film quality [14]. We have deposited bilayers and multilayers of Cu-Ti and attempted to improve the quality of the films in terms of their physical density and interface roughness [47]. Two Cu-Ti bilayers with alternate Cu, Ti deposition sequence had been deposited by DC magnetron sputtering. We had also deposited a Cu-Ti multilayer consisting of 5 bilayers with a nominal structure Si (substrate)/[Cu(56Å)/Ti(76Å)]×5 [47].

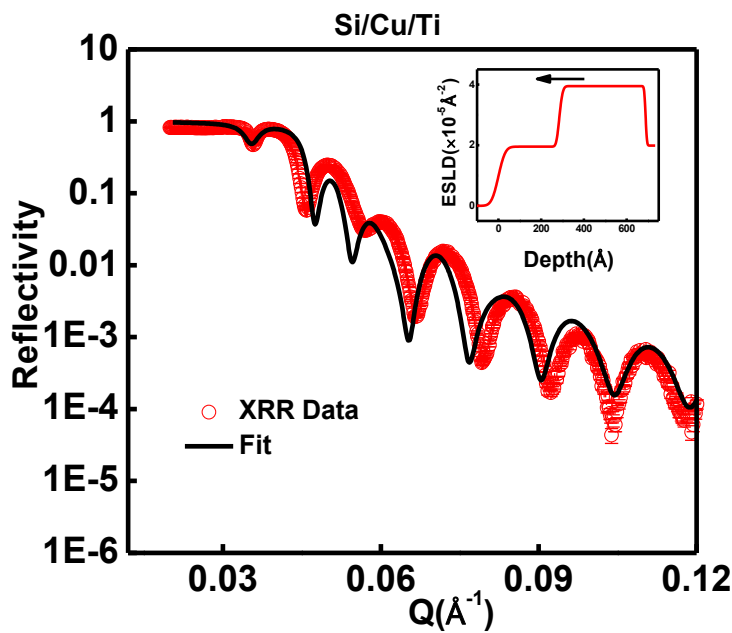


Figure 2.9: XRR of Si/Cu (405Å)/Ti (286Å)

The base vacuum was of the order of $\sim 4.7 \times 10^{-7}$ mbar and the working vacuum with the flow of Ar was $\sim 2.3 \times 10^{-2}$ mbar during the bilayer deposition. The TSD was fixed at 79.5 mm for the bilayer as well as for the multilayer deposition. XRR profile of a bilayer with nominal structure Si/Cu (405Å)/Ti (286Å) is given in Fig. 2.9. We observed that the ESLD of Cu and Ti layers were approximately 60% of their bulk density. It was also not possible to rule out the formation of oxide on exposure in the Ti layer, since the oxide layer also has a density close to 58 % of Ti. We tried to improve the base vacuum to $\sim 2.7 \times 10^{-7}$ mbar for deposition of the multilayer sample to reduce any in situ possible

oxidation of the Ti. Deposition rate of Cu was also reduced. The XRR data for the deposited multilayer is shown in Fig. 2.10. One can identify Bragg peaks up to 4th order for the sample demonstrating good interface quality of the sample. From XRR data fit we observed that the Cu layers have an average electronic scattering length density (ESLD) of $6.3 \times 10^{-5} \text{ \AA}^{-2}$ which is close to bulk density and the Ti layers also have an ESLD of $3.1 \times 10^{-5} \text{ \AA}^{-2}$ (90 % of bulk). The nominal thickness of the Cu layers was 56 \text{ \AA} and those of Ti layers were 76 \text{ \AA}. Thus by improving the base vacuum and by changing deposition rate we could improve the quality of the multilayer film [47].

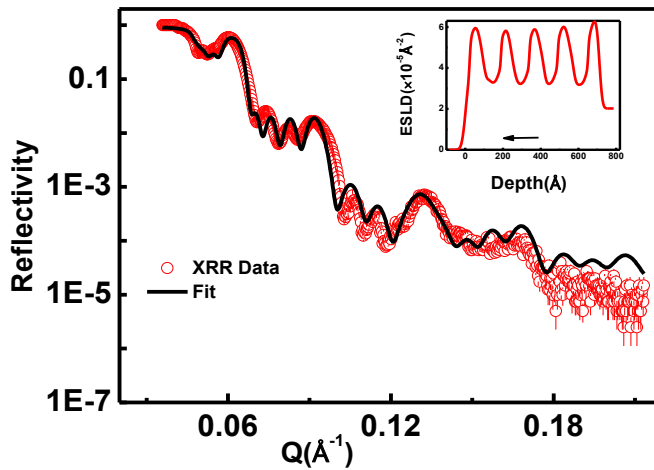


Figure 2.10: XRR of Cu-Ti multilayer [Si/[{Cu(56\text{ \AA})/Ti(76\text{ \AA})}\times 5]]

2.5.3.3 Ge films: Semiconducting layers

Installation of the third sputter gun as discussed in section 2.5.1 facilitates deposition of semiconductors through RF magnetron sputtering. Several thin films of Ge with varying TSD and sputter power has been deposited. The sputter power was varied between 5W to 50W and TSD was varied between 84mm to 90mm. Typical sputter power for RF sputtering (~ 40W) was observed to be larger compared to power for DC sputtering. The deposited films were characterized by XRR to examine the quality of the film in terms of its mass density and surface roughness. XRR profile of two Ge films with varying sputter power is given below

Fig. 2.11 (a) and (b). From XRR we observed that with increase in sputter power from 20W to 50 W the film quality improved substantially. The density of the Ge films increased from 80 % to 96 % of bulk with increase in sputter power and interface roughness decreased from 15 Å to 9 Å. This is evident from the XRR plots in Figs. 2.11 (a) and (b).

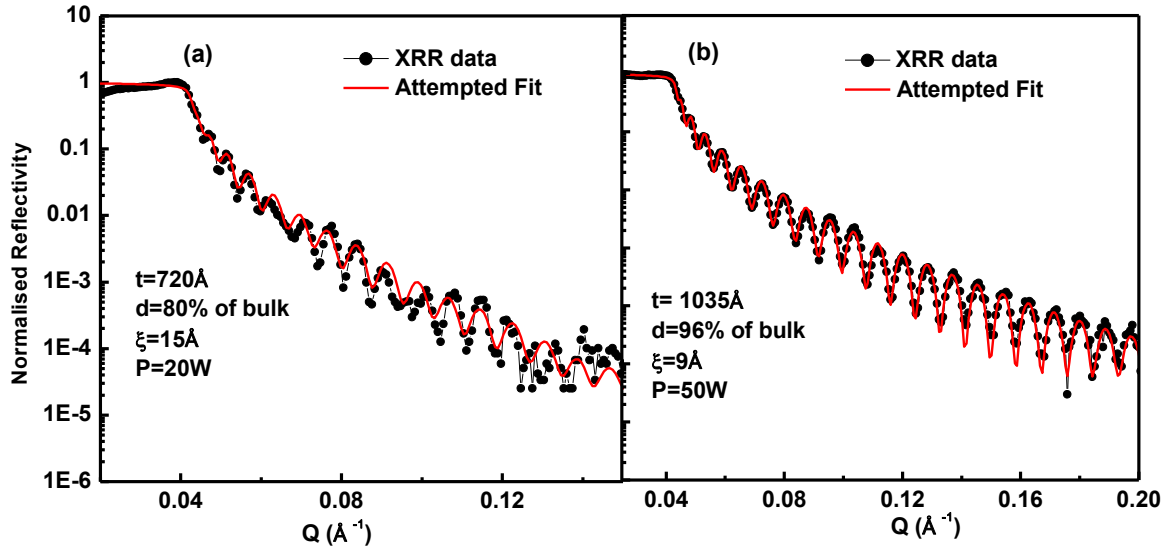


Figure 2.11: XRR profile of Ge films with varying sputter power (a) with 20W (b) with 50W.

We have also deposited and characterized bilayers of Ni-Ge before attempting to deposit a Ni/Ge multilayer film for polarized neutron reflectometry studies. The Ni and Ge layers were deposited with a deposition power of 18W and 40W respectively. The multilayer film was deposited on a boron doped p-type Si (111) substrate. XRR data of a Ni-Ge bilayer with the fitted profile (solid red line) is given in Fig. 2.12. Corresponding electron SLD (ESLD) profile of the bilayer is given as inset. The bilayer has a nominal structure of Si/Ni(93Å)/Ge(215Å) and density of both Ni and Ge were found to be close to their bulk density values with their respective roughness as 5Å and 4Å respectively. Following deposition of bilayers of Ni-Ge we fixed the deposition parameters and deposited a Ni-Ge multilayer. The base vacuum prior to deposition was $\sim 5 \times 10^{-7}$ mbar and the working vacuum with Ar flow was $\sim 4 \times 10^{-3}$ mbar during deposition.

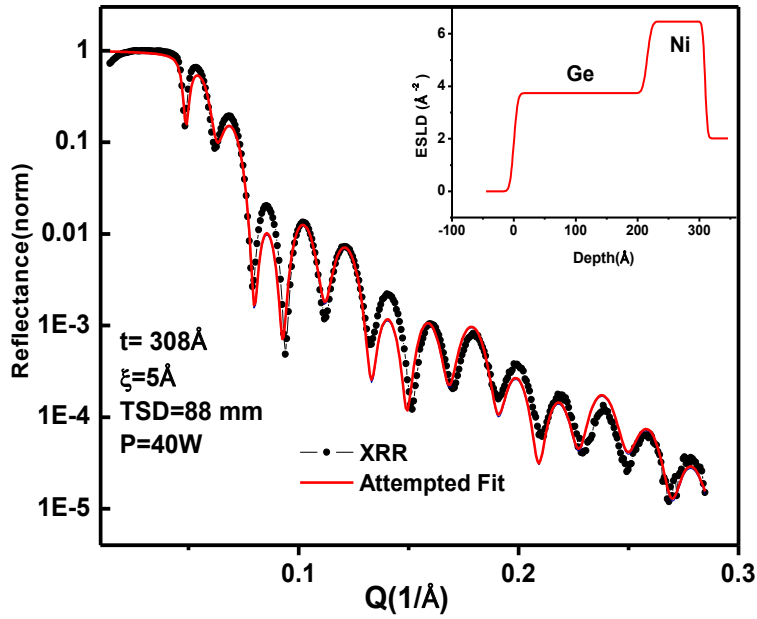


Figure 2.12: XRR profile of a Ni-Ge bilayer [Si/[Ni(93Å)/Ge(215Å)]]

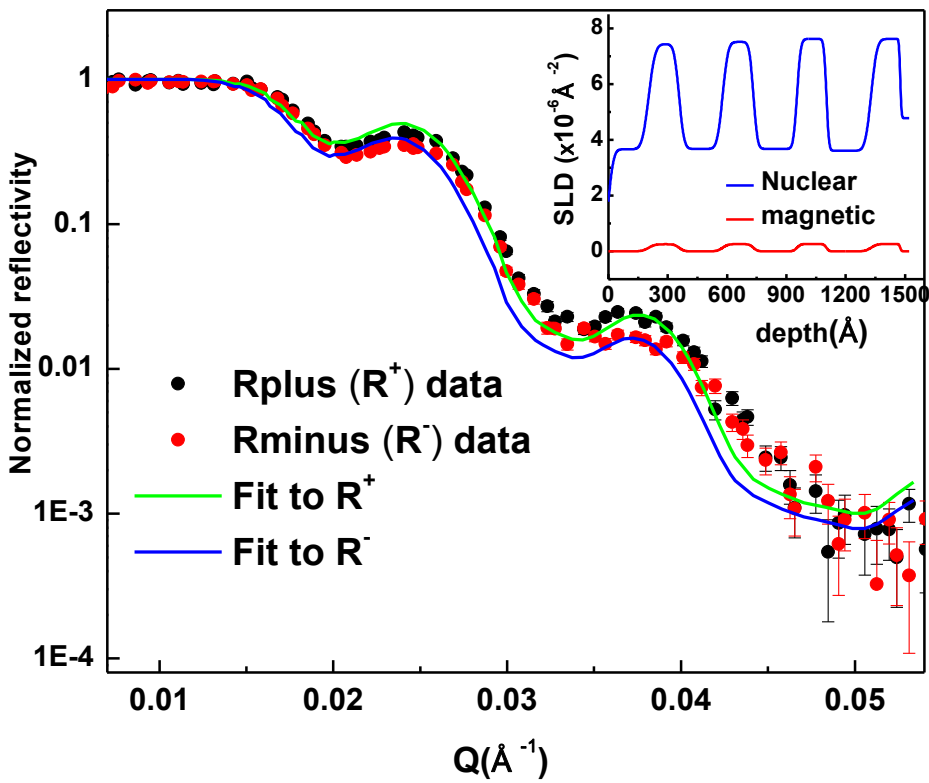


Figure 2.13: PNR profile of a Ni-Ge multilayer { Si (substrate) / [Ni_{100Å} / Ge_{200Å}]⁴}. Inset shows nuclear and magnetic scattering length density (NSLD and MSLD) profile of the multilayer. The Rplus and Rminus profiles were fitted simultaneously with same set of parameters.

Designed structure of the multilayer samples can be represented as: Si (substrate) / $[\text{Ni}_{100\text{\AA}}/\text{Ge}_{200\text{\AA}}] \times 4$. Detailed studies were carried out with this film using XRR, PNR, XRD and SQUID. We present the Polarized Neutron Reflectometry (PNR) profile of this sample along with the fits in Fig. 2.13 to highlight the quality of the film in the present section. R^+ and R^- profiles represents PNR pattern with respect to spin-up and spin-down neutrons respectively. Inset shows the nuclear and magnetic scattering length density profiles of the multilayer obtained from PNR fits. The density profile reveals clear periodic structure of the multilayer. The sample was annealed at 250°C under vacuum ($\sim 10^{-3}$ mbar) for time intervals of 0.5h, 1.5h and 4h. Details of these studies done on this multilayer is discussed in chapter 5 of this thesis. Micro-structural evolution in the multilayer on annealing has been included a separate work [51].

Chapter 3: Neutron and X-ray Reflectometry

- 3.1 Reflectometry at a glance
- 3.2 Theory of Neutron and X-ray Reflectometry
 - 3.2.1 Refractive index and Critical Angle
 - 3.2.2 Reflectometry from an ideal surface
- 3.3 Theory of Polarized Neutron Reflectometry
- 3.4 Neutron reflectometry at DHRUVA
 - 3.4.1 Description of the instrument
 - 3.4.2 Control and data acquisition system
 - 3.4.3 Resolution of the instrument
 - 3.4.4 Analysis of specular reflectometry data
 - 3.4.5 Estimation of errors in fitted parameter
- 3.5 Determining stoichiometry of interface alloy layer by XRR and PNR

3.1 Reflectometry at a glance

X-Ray and Neutron Reflectometry are based on the principle of reflection of x-ray or neutrons from the surface of a thin film. The reflected beam bears signature of the structure of the thin film at mesoscopic length scales [52]. Reflection is an optical phenomenon where electromagnetic radiation (e.g. visible light, x-rays) or matter waves (e.g. neutrons) are reflected from an interface between two media of different indices of refraction. For x-rays and neutrons, however, most materials have indices of refraction marginally less than one. This means that neutrons or x-rays impinging on a surface will undergo total external reflection up to a certain angle of incidence with respect to the reflecting surface. The real part of the refractive index of a medium for neutrons or x-rays can be represented as $1 - \delta$, where δ is typically $\sim 10^{-6}$ for neutrons and $\sim 10^{-5}$ for x-rays. This entails that total reflection of x-rays/neutrons can occur only when they impinge on a surface at a glancing angle. Reflectivity of the surface is unity up to the critical angle for total external reflection (similar to total internal reflection for visible light) and falls sharply when the incident angle is larger than the critical angle due to penetration of the radiation in the film. This reflected intensity as a function of angle carries information regarding structure of

the film at mesoscopic length scale in terms of its density, thickness, surface roughness from where it is reflected.

There are two possible types of reflections from a surface: (a) specular reflection, which obeys Snell's law, when the angle of reflection is equal to the angle of incidence ($\theta_i = \theta_r$ in Fig. 3(b)) and (b) off-specular reflection, where the above equality is not maintained. Fig 3.1(a) gives a sketch of specular and off-specular (or diffuse) reflection from a rough surface. Specifically, specular reflectivity can be used to reconstruct laterally averaged compositional depth profile along the normal to the surface of the film [53]. Specular neutron reflectivity in un-polarized mode can be used to determine the structural parameters of thin films in terms of individual layer thickness, interface roughness and the density of the layers (similar parameters are also given by x-ray reflectivity). In polarized mode neutron beam is spin-polarized with respect to sample magnetization, either parallel (reflectivity R^+) or anti parallel (reflectivity R^-) with a possibility of polarization analysis of the reflected beam (R^{++} , R^{+-} , R^{-+} , R^{--}). From R^+ and R^- we can obtain additional information of magnetic moment density profile of a magnetic layer along with the structural parameters [54,55]. If one carries out polarization analysis of the reflected beam then one can also obtain in-plane magnetic structure of the thin film [56]. In the present thesis we have used specular polarized neutron reflectivity (PNR) and x-ray reflectivity (XRR) only for characterizing thin samples. Specular reflectivity from a sample surface is measured as a function of the wave vector transfer $Q = 4\pi \sin(\theta)/\lambda$ along a direction perpendicular to the sample surface as shown in Fig.3.1(a), where 'θ' is the incident angle on the film and 'λ' is the wavelength of the incident radiation. Off-specular reflectivity introduces a component of wave vector along the surface of the sample providing information about the lateral in-homogenities in the sample. Hence it can be used to obtain the height-height correlation function on a surface,

which provides detail morphology of the surfaces and buried interfaces (in-plane structure) [56].

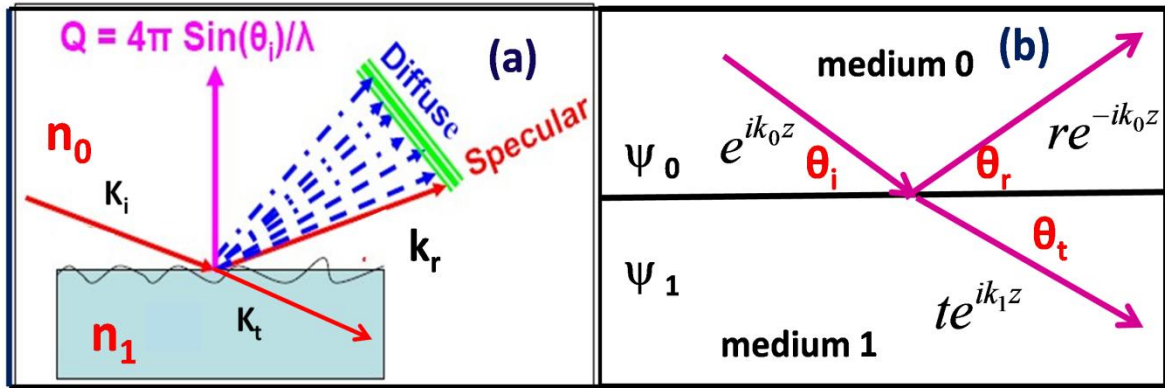


Figure 3.1: (a) Geometry of specular and off-specular (diffuse) reflectivity (b) Wave function at the interface

3.2 Neutron and X-ray Reflectometry at an interface

Treatment of neutron reflectometry considers the neutron beam as a particle wave and uses quantum mechanics to calculate reflection (r) and transmission (t) amplitudes at the interfaces [56]. For X-ray reflectometry (XRR) one uses Maxwell’s equations leading to continuity of electric field and its derivative, to evaluate the transmission and reflectivity amplitudes [57]. Here we consider an one dimensional potential that varies along the depth of the sample. Considering Ψ_0 and Ψ_1 , representing the neutron wave function outside (medium 0) and inside (medium 1) the reflecting sample (Fig. 3.1) we can write:

$$\psi_0(z) = e^{iK_0z} + re^{-iK_0z} \dots\dots\dots(3.1)$$

$$\psi_1(z) = te^{iK_1z}$$

Where K_0 and K_1 are the wave vectors in medium 0 and 1 respectively considering ‘Q’, the momentum transfer vector measured along z direction, normal to the sample surface. The

wave function $\Psi_0(z)$ comprises the incident and the reflected amplitudes. The Schrödinger equation for the wave function in a medium can be written as [56]:

$$\left[-\frac{\hbar^2}{2m_n} \frac{\partial^2}{\partial z^2} + V(z) \right] \psi(z) = E \psi(z) \quad \dots\dots\dots(3.2)$$

Where \hbar is Planck's constant divided by 2π , The potential $V(Z)$ is given by

$$V = \frac{2\pi\hbar^2}{m} Nb, N = \frac{dN_A}{M}$$

is the neutron-nucleus potential seen by the neutron in a medium,

m_n is the mass of the neutron, and $E = \frac{\hbar^2 k_0^2}{2m_n}$ is the neutron energy in vacuum and $k = 2\pi/\lambda$,

is its wave vector [58]. Where N, d, N_A, M, b are the atomic number density, atomic density, Avogadro's number, atomic (molecular) weight, and the coherent neutron scattering length respectively.

The intensity of the specularly reflected signal from an ideally flat surface can be calculated by considering continuity of the neutron wave function $\Psi(z)$ and its derivative (electric field $E(z)$ and its derivative for x-rays) at the interface. The result is known as *Fresnel relationships*, which gives the amplitude of specular reflection and the transmission coefficient of the beam.

Schrodinger's equation for the neutron wave function in a medium can be given by:

$$\left[\frac{\partial^2}{\partial z^2} + k_0^2 - 4\pi\rho(z) \right] \psi(z) = 0 \quad \dots\dots\dots(3.3)$$

From continuity of ψ and $d\psi/dz$ we can get: $I+r = t$; $q_1(1-r) = q_2 t$; where q_1 and q_2 are the normal components of the wave vector in vacuum and in the medium respectively and r, t are the reflection and transmission amplitudes. Solving these two equations for r and t , we can get :

$$r = \frac{q_1 - q_2}{q_1 + q_2}; \quad t = \frac{2q_1}{q_1 + q_2} \quad \dots\dots\dots(3.4)$$

Where, $q_1 = \frac{2\pi}{\lambda} \sin \theta$ and $q_2 = \sqrt{q_1^2 - 4\pi\rho b}$ and θ is the glancing angle. The *Fresnel* reflectivity for an ideally flat surface, is defined as :

$$r_f = |r|^2 = \left| \frac{q_1 - q_2}{q_1 + q_2} \right|^2 = \left| \frac{\sin \theta - \sqrt{n^2 - \cos^2 \theta}}{\sin \theta + \sqrt{n^2 - \cos^2 \theta}} \right|^2 \dots\dots(3.5)$$

From eqn. (3.5), when $\cos \theta > n$ then r is a complex number and the *Fresnel* reflectivity is unity, i.e. for $\theta < \theta_c$ there will be total external reflection of neutrons. Above the critical angle when $\theta \gg \theta_c$ the reflectivity drops off as θ^{-4} . Then r_f can be written as:

$$r_f = \frac{16\pi^2 \rho^2 \langle b \rangle^2}{Q^4} \dots\dots\dots(3.6)$$

This rapid drop in intensity beyond critical angle makes reflectivity experiment intensity limited at larger angles.

3.2.1 Refractive Index and Critical Angle

From equation (3.3), it can be shown:

$$k_1 = nk_0 = \sqrt{1 - \frac{4\pi\rho}{k_0^2}} k_0 \dots\dots\dots(3.7)$$

Where n is the index of refraction of the medium (R.I.) for neutrons [59].

According to Snell's law, at the interface between two media the R.I is defined as:

$$n = \frac{\cos \theta_i}{\cos \theta_t} \dots\dots\dots(3.8)$$

Where θ_i and θ_t are angle of incidence and transmission respectively (Fig.3.1 (b)). For total external reflection, at critical angle θ_c we have, $\theta_t = 0$,

Then,
$$n = \cos \theta_i = \cos \theta_c = 1 - \frac{\theta_c^2}{2} \dots\dots\dots(3.9)$$

Under the assumption that $\theta_c \rightarrow 0$. Comparing with (3.7) and putting value of k_0 for neutrons,

$$n = \sqrt{1 - \frac{4\pi\rho}{k_0^2}} = \left(1 - \frac{\lambda^2}{\pi} \sum_i N_i b_i\right)^{1/2} = \left(1 - \frac{\lambda^2}{2\pi} \sum_i N_i b_i\right)$$

This implies, $\theta_c = \lambda \sqrt{N_i b_i / \pi}$ (3.10)

This expression illustrates that the critical angle is dictated by the scattering length density of the medium ($N_i b_i$) for the i^{th} species. The refractive index for neutron is, in most cases, smaller than one except a few materials with negative scattering lengths (e.g. Ti and Mn). This means the neutrons will undergo total external reflection from most of the material surfaces.

Refractive index for neutron as well as for x-rays can be given by a general expression:

$$n = 1 - (\delta - i\beta)$$

Where ‘ δ ’ is the deviation from unity given by $\frac{\lambda^2}{2\pi} \sum_i N_i b_i$ and ‘ β ’ contains the absorption term. For most of the materials studied, the absorption coefficient ‘ β ’ is very small for neutrons and hence usually neglected. Similar treatment for x-rays yields:

$$n = 1 - \frac{\lambda^2 r_0}{2\pi} \sum_i N_i (Z_i + f_i)$$
(3.11)

Where r_0 is the classical electron radius = 2.81fm, N_i is the number density Z_i is the atomic number and ‘ f_i ’ is the energy dependent anomalous dispersion factor for the i^{th} species.

Now comparing with (3.9) critical angle for x-ray can be written as:

$$\theta_c = \lambda \sqrt{\frac{r_0}{\pi} N_i (Z_i + f_i)}$$
(3.12)

For most of the materials the critical angles are about few arc minute per Å wavelength. For x-ray the critical angle are somewhat larger compared to neutrons due to the larger value of δ for x-rays.

3.2.2 Reflectivity from a rough surface

Reflectivity from an ideal surface is given by equation 3.5. But perfectly flat interface or surface can't be achieved in reality and the modulation of the actual interface between the layers are modified by undulations with respect to the ideal interface (shown as inset in Fig.3.2) and termed as physical roughness.

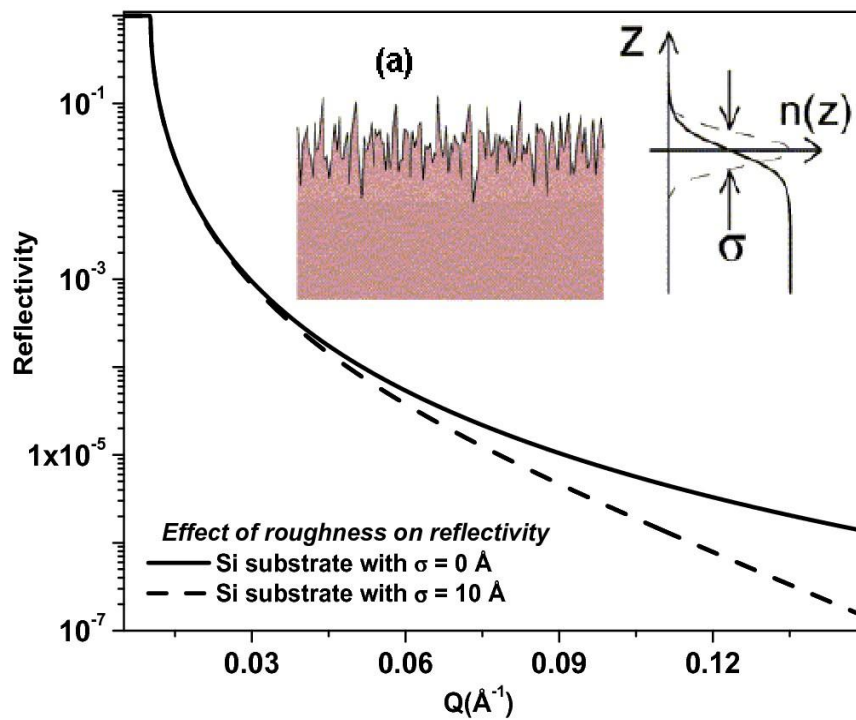


Figure 3.2 Effect of roughness on specular reflectivity from Si substrate with $\sigma = 0 \text{ \AA}$ (solid line) and $\sigma = 10 \text{ \AA}$ (dashed line). Inset (a) shows image of rough interface with Gaussian profile of height. The standard deviation of the Gaussian function describing the roughness represents the root mean square roughness, σ .

Another kind of in-homogeneity, which arises at the interface, is mixing of two materials due to inter-diffusion. These two components constitute the roughness at an interface. The

influence of the physical roughness and of the inter-diffusion is indistinguishable in specular reflectivity and both are categorized as the root mean square roughness to give a convoluted roughness parameter. For specular reflectivity calculations, they (the physical roughness and mixing due to inter-diffusion) to give an average σ . It is necessary to incorporate the roughness, i.e., the width of the interface for determining reflected intensity from a sample. Roughness has the effect of reducing the specular intensity at any given momentum transfer value. Inset (a) of Fig 3.2 shows a typical rough interface with the profile of the random height distribution, which is a Gaussian, centered on an average interface. The standard deviation of the Gaussian function describing the roughness represents the root mean square roughness, σ . The reflectance for a Gaussian rough surface after including the effect of roughness is defined as [60]:

$$r(Q) = r_F e^{-\frac{Q^2 \sigma^2}{2}} \dots \dots \dots (3.13)$$

Where, Q is the momentum transfer vector, given by $Q = \frac{4\pi}{\lambda} \sin \theta$ and r_F is *Fresnel* reflectance of the ideal surface given in Eqn. (3.5). Roughness adds an exponential damping factor ($e^{-\frac{Q^2 \sigma^2}{2}}$) to the reflectivity, similar to Debye-Waller factor in diffraction [60]. Above equation shows, reflectivity is very sensitive to the roughness of the sample at larger momentum transfer values. Even small roughness will cause a substantial deviation of the reflectivity from the ideal *Fresnel* case. Fig 3.2 shows the reflectivity of a Si substrate without any roughness (shown by continuous line) and with a roughness of 10 Å (shown by dashed line). Fig. 3.2 shows clearly how the reflectivity from a rough interface deviates from the reflectivity from an ideal smooth surface as a function of Q .

Equation 3.13 gives the reflected intensity from the surface of an infinitely thick layer. The reflectivity for a multiple layer or multilayer structure can be obtained by using Parrat's

formalism [15]. This formalism allows one to calculate the reflected intensity from an idealized stratified medium of known layer thickness and density.

Consider a neutron beam incident on a multilayer stack, i. e., a series of N layers ($N+1$ interfaces), where the i^{th} layer has thickness d_i , interfacial roughness σ_i , and refractive index n_i (defined in Eqns. (3.7) as shown in Fig. 3.3 The semi-infinite region below the film, the substrate, has refractive index n_s .

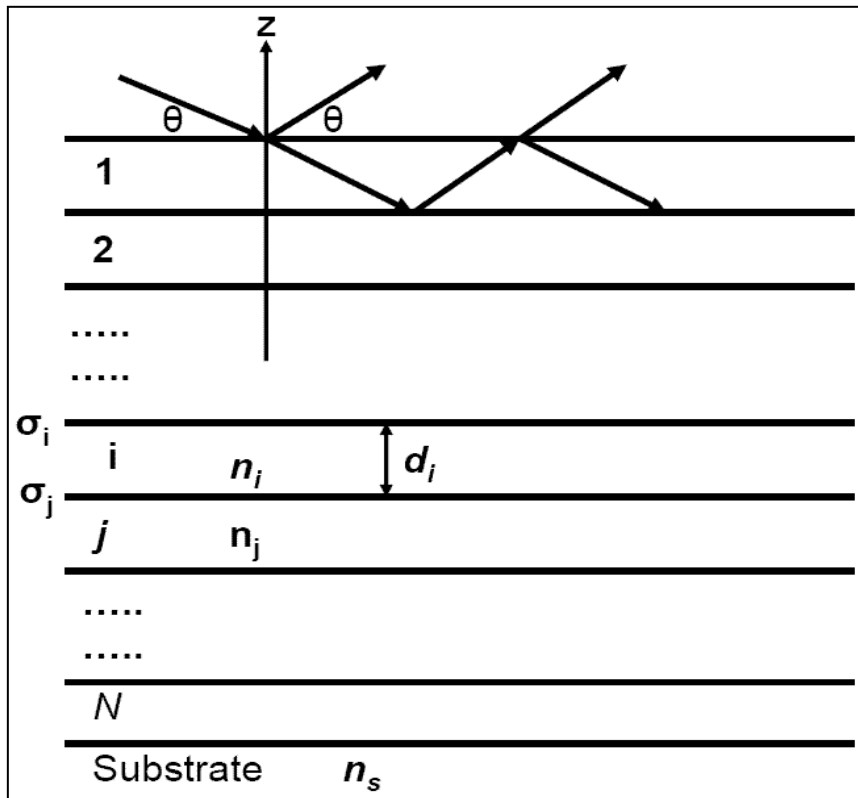


Figure 3.3: Diagram of a multilayer stack containing N layers, where the refractive index, thickness, propagation angle, and interface roughness parameter of the i^{th} layer are n_i , d_i , θ_i and σ_i , respectively.

To find the reflectance for a multilayer, the boundary conditions must be fulfilled at each interface. One needs to start from the bottom layer, which is the substrate (Fig. 3.3) and build the reflectivity upwards to the air-film interface by applying the continuity conditions at every interface. The ultimate goal is to find the reflectance on the top of the multilayer.

Parratt's formalism is used extensively to generate reflectivity pattern (both for x-ray and neutrons) from multilayer samples theoretically [15].

Consider a sample consisting of N layers $j = 1 \dots N$ as shown in Fig. 3.3. The *Fresnel* reflectance and transmittance between j^{th} layer and $j+1^{\text{th}}$ layer can be calculated from the continuity of wave function and its derivative at the interface. For smooth interface the *Fresnel* reflectance and transmission amplitude are $r_{j-1,j} = (k_{z,j-1} - k_{z,j}) / (k_{z,j-1} + k_{z,j})$ and $t_{j-1,j} = 2k_{z,j-1} / (k_{z,j-1} + k_{z,j})$, respectively [57], with $k_{z,j}$ the z component of the wave vector in medium j , which is determined by the law of refraction: $k_{z,j} = k(n_j^2 - \cos^2 \theta)^{1/2}$. The glancing angle of incidence is θ and $k = 2\pi / \lambda$ is the modulus of the incoming wave vector (λ is the wavelength of neutron/x-ray). The phase factor that is defined in the middle of two surface of j^{th} medium is $a_j = e^{ik_{z,j}d_j/2}$, with $d_j =$ thickness of j^{th} layer. We first consider a film on a substrate having a thickness d and uniform scattering length density. The film will have two-step changes in the refractive index, at the air/film and film/substrate interfaces, separated by a distance d . The reflection coefficient of the sample, in terms of the *Fresnel* reflection coefficients at the substrate/sample interface, $r_{1,2}$, and at the sample/air interface, $r_{0,1}$, can be written as:

$$r = \frac{r_{0,1} + r_{1,2} \exp(2ik_{z,1}d)}{1 + r_{0,1}r_{1,2} \exp(2ik_{z,1}d)} \dots\dots\dots(3.14)$$

We can easily extend the above calculation to the case of reflectivity for a system having N such thin layers (stratified homogeneous media), having smooth interfaces. A set of simultaneous equations similar to Eqn. (3.14) can be solved and one can arrive at a recursive formula [15] given by:

$$R_{j-1,j} = \exp(-2ik_{z,j-1}d_{j-1}) \frac{R_{j,j+1} + r_{j-1,j}}{1 + R_{j,j+1}r_{j-1,j}} \dots\dots\dots(3.15)$$

Where $r_{j-1,j}$ and $k_{z,j-1}$ are defined in the above paragraph. To obtain the reflectivity of this system, one solves this recursive relation given by Eqn. (3.15) from the bottom layer with the knowledge that $R_{n,n+1} = 0$ since the thickness of this medium (normally the substrate) can be taken as infinite. So the reflectivity of the system (smooth interfaces) is given by $I = |R_{0,1}|^2$.

The reflectivity for rough multilayer can be calculated by considering a static ‘Debye – Waller’ like factor (Eqn. 3.13) for reflectance at each interface in multilayer and using above recurrence relation. The *Fresnel* reflectance from $j-1^{\text{th}}$ layer and j^{th} layer for rough interface is

given by: $r_{j-1,j} = \exp(-2k_{z,j-1}k_{z,j}\sigma_j^2) \frac{k_{z,j-1} - k_{z,j}}{k_{z,j-1} + k_{z,j}}$. The Parratt formalism has the advantage of

providing the correct expression for all regions of scattering since no approximation is applied, and any density profile can be modeled by slicing the material in an arbitrary number of thin layers.

3.3 Polarized Neutron Reflectometry (PNR)

Polarized Neutron Reflectometry (PNR) is a tool to investigate the physical as well as magnetization depth profile in thin films and multilayers [61]. This technique is highly sensitive, being able to measure the absolute magnetization of a monolayer of iron ($\sim 10^{-4}$ emu) with 10% precision [62], and magnetization density as small as 30 emu/cm^3 with comparable precision. Detection of small moments (from samples with surfaces measuring $\sim \text{few cm}^2$ in area) is possible combined with excellent depth resolution of fractions of a nanometer even for films as thick as several hundreds of nanometer.

Neutrons have a spin $\vec{\sigma}$, related to the magnetic moment $\vec{\mu}_n$ of the neutron by the vector operator:

$$\vec{\mu}_n = \mu_n \vec{\sigma} \quad \dots\dots\dots (3.16)$$

With $\mu_n = -1.913 \beta_N$ [63] and β_N the nuclear magnetron equal to $e\hbar/2m_p c$, where, e is the elementary charge, m_p is the proton mass and ‘c’ is the speed of light in vacuum. From quantum mechanics it follows that the magnitude of the spin of a neutron is always $\hbar/2$, and only one component of the spin can be quantized along a chosen direction giving the values $\hbar/2$ or $-\hbar/2$. For convenience, however, in this thesis “spin up” and “spin down” convention has been used for the magnetic moment of the neutron beam parallel and anti-parallel to the applied field. The spin up component increases the neutron-nucleus scattering potential whereas the spin down component decreases it. Because of the magnetic moment, corresponding to the spin, the potential energy of a neutron in a magnetic medium contains a nuclear and a magnetic term

$$V = V_n + V_m \quad \dots\dots\dots (3.17)$$

The nuclear part of V is defined in Eqn. (3.2). The magnetic part of the potential may be written as [64]:

$$V_m = \pm \mu_n B \quad \dots\dots\dots (3.18)$$

Where, B is the magnitude of magnetic induction and the $+(-)$ applies for the spin component parallel (anti parallel) [i.e. spin up (spin down)] to the induction. In reflectivity the difference in potential energy ΔV (i.e. change in refractive index at interface) at an interface, rather than potential energy itself is of importance.

In the experiments described in this thesis, the magnetic field is usually applied in the y-direction (see Fig. 3.4 for direction conventions used in this thesis). Further, if it is assumed

that the in-plane magnetization in the sample is parallel to the applied field direction, the magnitude of the magnetic potential can be written as [64].

$$|\Delta V_m| = \mu_n |B_y - B_0| = \mu_0 \mu_n |M_y| \quad \dots\dots\dots(3.19)$$

Where B_0 is the magnetic induction outside the sample and μ_0 is the magnetic permeability of vacuum.

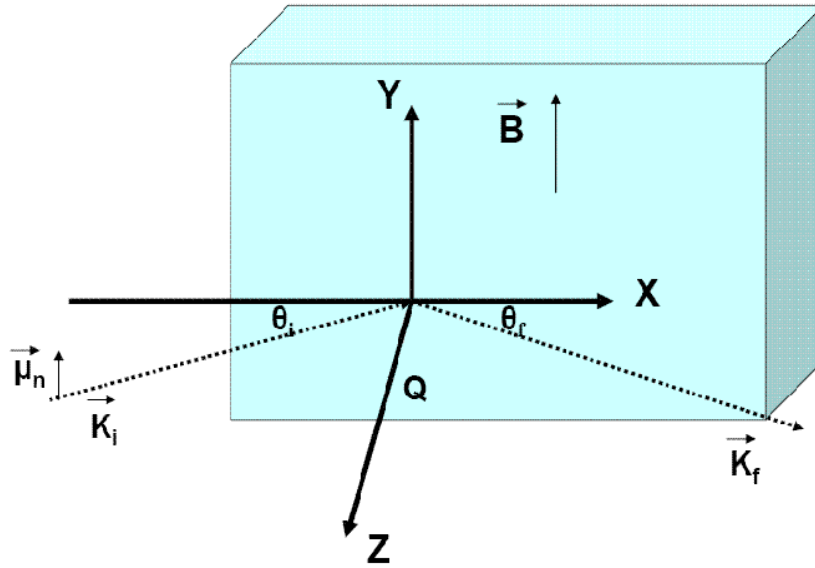


Figure 3.4: Schematic, representation of the scattering geometry, for polarized neutron reflectivity measurements, used in the present thesis.

Analogous to the nuclear scattering length b , a magnetic scattering length p can be defined. This magnetic scattering length is related to μ_s the magnetic moment per atom expressed in units of Bohr magnetons, by the relation:

$$p = \frac{m_n \mu_n \mu_0}{2\pi \hbar^2} \mu_s \quad \dots\dots\dots(3.20)$$

So the magnitude of magnetic potential difference when entering a sample (which is saturated along in-plane direction, i.e. y-axis in Fig. 3.4) can now be written in terms of p , the magnetic scattering length:

$$|\Delta V_m| = \frac{2\pi \hbar^2}{m_n} Np \quad \dots\dots\dots(3.21)$$

Where, N is same as defined in Eqn. (3.3). So, the total interaction potential for neutron in a magnetic medium can be written in the form

$$V = V_n + V_m = \frac{2\pi\hbar^2}{m_n} N(b \pm p) \dots\dots\dots(3.22)$$

Where (+) and (-) signs corresponds to the spin up and spin down neutrons with respect to sample magnetization. Now using Eqn. (3.4) and (3.8) the refractive index and critical angle for a neutron in magnetic medium can be written as:

$$n = 1 - \frac{\lambda^2}{2\pi} N(b \pm p); \theta_c = \lambda \sqrt{\frac{N(b \pm p)}{\pi}} \dots\dots\dots(3.23)$$

Magnetizing the sample to saturation in the direction perpendicular to the surface of the sample (i.e. along z-axis, which is also the direction of momentum transfer (Q) makes B_x and B_y vanish. Because $\nabla \cdot \vec{B} = 0$, B_z is the same inside and outside the sample. Therefore, in this case, neutrons hitting the sample experience changes only in nuclear part of potential and one gets pure nuclear contribution to neutron reflectivity.

Fig. 3.5 (a) and (b) shows simulated un-polarized and polarized neutron reflectivity pattern respectively, for a Ni/Al multilayer as a function of wave vector transfer Q generated using Parrat's formalism explained above. For simulating polarized reflectivity pattern we have used the bulk magnetic moment ($0.60\mu_B$) for Ni atom.

The difference in the reflectivity pattern of the sample for spin up and spin down neutrons is due to the difference in the step potential due to magnetic part of the Ni layers for the spin up and spins down neutrons. The change in critical angle (Eqn. 3.23) for the two spins is also evident in Fig. 3.5.

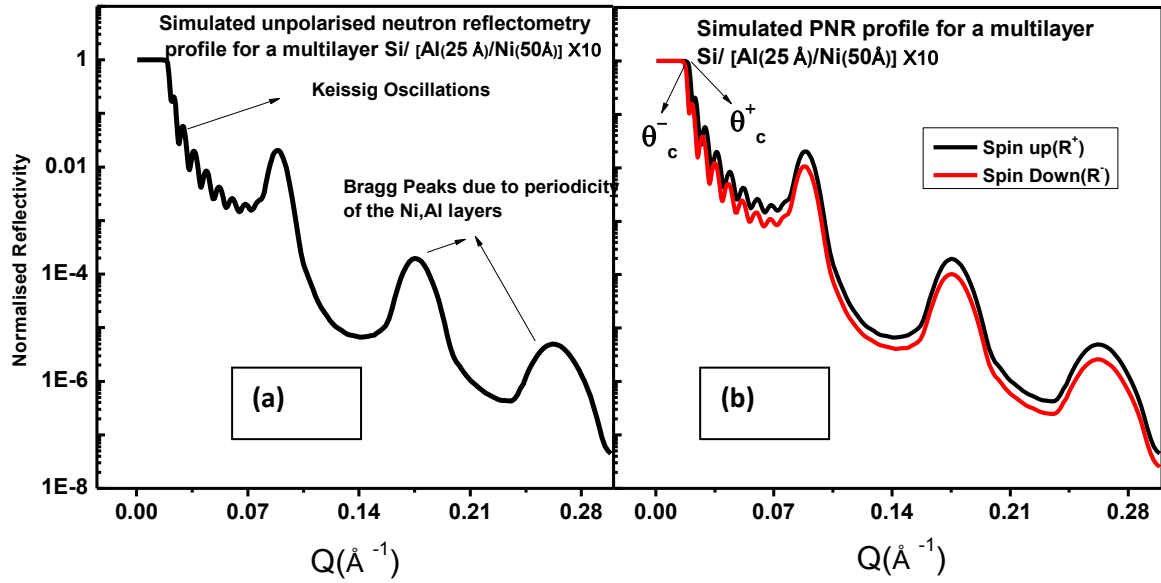


Figure 3.5: Simulated (a) Un polarized and (b) Polarised neutron reflectivity pattern for a Ni/Al multilayer, θ_c^\pm denotes critical angle due to spin up an spin down neutrons respectively.

3.4 Polarized Neutron Reflectometer at DHRUVA

In case of polarized neutron reflectometry one measures the specularly reflected intensity as a function of wave vector transfer ' Q '. The wave vector transfer Q is scanned either by collecting the data by varying θ with a fixed λ (monochromatic beam reflectometer) or by using a white beam with varying λ and collecting the data at a fixed angle θ (time of flight (TOF) reflectometer). In the present case we used a monochromatic beam reflectometer at DHRUVA reactor, BARC, INDIA. In this type of reflectometer it is desirable to use neutrons of longer wavelength, preferably in the range of 2-5 Å. A monochromator with a large mosaic spread (0.5° corresponding to $\delta\lambda/\lambda \sim 1\%$) and high reflectivity should be chosen. For specular reflectivity measurements the sample and the detector are moved in θ - 2θ mode to cover the desired Q range. This can also be achieved by using a linear position sensitive detector (PSD), where only sample table is rotated to cover the desired Q range and the

reflected beam is detected on the PSD without moving the detector. This rotation stage needs to have resolution in the range of tens of arc seconds. A constant wavelength instrument is the simplest and probably the cheapest type of reflectometer that can be built.

3.4.1 Description of the instrument

The schematic diagram of the PNR set up is shown in Fig. 3.6 (a). Neutron beam from a reactor beam tube is carried to an adjacent laboratory using a curved neutron guide tube (GT) which can transport neutrons out from the reactor hall. The reflectometer is located on a thermal neutron guide tube with a radius of curvature of 3.3 km (critical wavelength 2.2 Å). The [119] reflection from a cylindrical Si single crystal monochromator gives a monochromatic neutron beam of 2.5 Å reflected at approximately 99 degree angle with respect to the guide tube axis. The chosen reflection [Si(113)] does not have any second order contamination and comes out nearly normal to the guide axis, which is desirable. The beam from the monochromator enters a collimator, consisting of two vertical cadmium slits located at a distance of 800 mm from each other, that gives the initial collimation of the beam. The Cd slits have heights of 40 mm and horizontal width varying from 0.1 to 1 mm. Following the collimator there is a non-polarizer/polarizer mirror assembly on a translation and rotation stage combination. Two such non-polarizer/polarizer super mirror assemblies along with their rotation and translation stages had been procured from PNPI, St Petersburg, Russia. The assembly consists of two neutron mirrors, a non-polarizing supermirror and a polarizing neutron supermirror in a permanent magnetic field with their reflecting planes vertical, placed nearly parallel to each other at a distance of approximately 10 mm. One can switch from un-polarized to polarized beam mode quite easily by predetermined rotation and translation to bring the required mirror in the neutron beam.

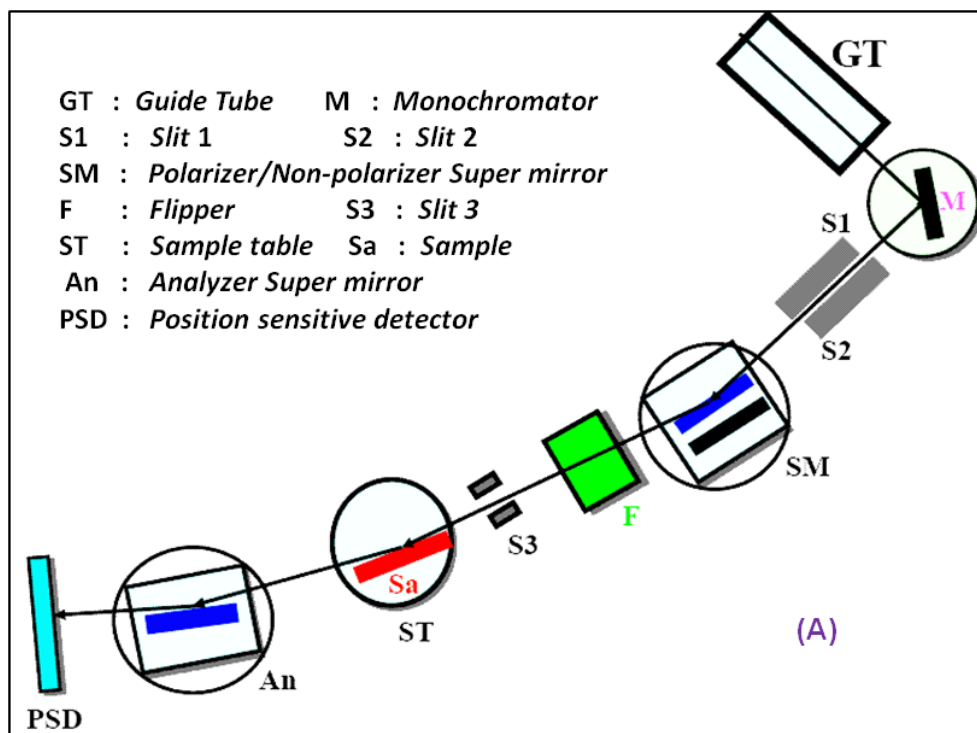


Figure 3.6 (a): The schematic of polarized neutron Reflectometer at Dhruva

A D.C. (Mezei) flipper [65] for flipping the spin of the polarized neutron beam is located after the polarizer. Following the flipper there is a third Cd-slit, close to the sample stage for final collimation. A neutron beam of horizontal divergence in the range of 0.8–5 arc min can be delivered on the sample using several combinations of Cd-slits. The sample is placed on a translation stage which itself is located on top of a high precision rotation stage. The smallest step size of the rotation 0.001° with an accuracy of 15 arc min. There is also an absolute encoder at the bottom of the rotation stage to provide true rotation. The sample is placed between the pole pieces of a permanent magnet of 2 kG strength (vertical) for in-plane magnetization of the samples during polarized runs. A Position Sensitive Detector (PSD) allows one to collect specular as well as off-specular (or diffuse) data simultaneously around any specular peak. This configuration overcomes the intensity problem for collecting off-specular (diffuse scattering) reflectivity data in a medium-flux reactor. Data collected on the PSD, beyond specular peak, correspond to conventional detector scan for diffuse scattering.

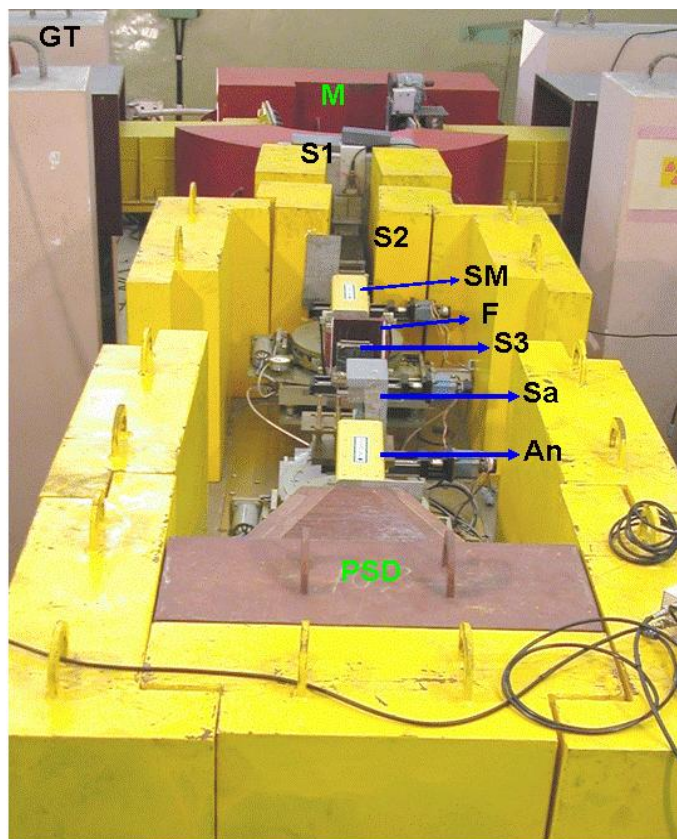


Figure 3.6: (b) Photograph of the polarized neutron Reflectometer at Dhruva reactor

The entire spectrometer assembly, surrounded by shielding blocks, is located on a stainless steel table made from 8mm thick stainless steel plate. Fig. 3.6 (b) shows the photograph of the spectrometer. The total weight of the table along with the shielding blocks and parts of the spectrometer is about six metric tons, which makes the spectrometer table nearly vibration free. The specifications of the instrument are given in table 3.1.

3.4.2 Control and data acquisition system

A stepper motor-based control system has been designed for the high precision translation and rotation stages. The monochromator is mounted on a tilt and rotation stage assembly. The spectrometer table can rotate around the monochromator to facilitate θ - 2θ coupling between the monochromator and the table. This allows changing the incident wavelength, if required.

Table 3.1: Specification of PNR instrument

(i) Guide tube	Critical wavelength λ_c 2.2 Å with a radius of curvature 3452 m.
(ii) Scattering plane	Horizontal (vertical sample)
(iii) Monochromator	Cylindrical Si single crystal [113] plane with 50mm diameter and 100mm height, mosaic: 15 arc min
(v) Incident wavelength	2.5 Å
(vi) Collimation using Cd slits	0.8–5.0 arc min. Variable horizontal width
(vii) Distance between slit S1 and slit S3	1340mm
(viii) Beam size and divergence at sample	0.8 to 5 arcmin
(ix) Neutron flux at sample	10^4 n/cm ² /s
(x) Polarizer/analyzer supermirror	FeCo/TiZr based supermirror of dimension 200 mm × 70 mm
(xi) Non-polarizer supermirror	NiMo/Ti based supermirror of dimension 200mm × 70mm
(xii) Reflectivity of supermirrors	90% at an angle of incidence of 20 arc min
(xiii) Polarization efficiency of super mirror	95% at an angle of incidence of 20 arc min
(xiv) Efficiency of DC flipper	92%
(xv) Sample to detector distance	1085mm
(xvi) Typical sample size	$\geq 2 \times 2$ cm ²
(xvii) Detector	³ He gas filled linear PSD of 200mm length
(xviii) Detector resolution	3mm
(xix) Q-range	0.007–0.10 Å ⁻¹
(xx) Dynamic range	$1:10^4$

The collimator is mounted on a high precision linear stage, which can move the collimator in steps of 10 microns across the beam. A similar linear stage to move the second slit in the collimator across the first slit is present. These two stages were used initially to align the neutron beam on the sample table centre. The sample and the magnet are mounted on a linear stage with one-micron step size on top of a rotation stage. Sample surface is brought to the centre of the rotation stage with the help of this linear stage. In the high precision rotation stage an optical encoder is located at the bottom of the rotation table that allows one to monitor true rotation of the table with a resolution of 0.001 °. The control system for all the stepper motors is an integral unit with the drivers and the power supplies located in it. It is operated from the instrument's PC through a serial port communication. Options exist for

collecting data either for a fixed number of monitor counts or for a fixed time. The data acquisition software allows one to select the number of steps in the reflectivity scan and the angular step size. Once a run starts, the system collects data for fixed monitor counts (or time), saves the data channel wise in a file, moves to the new reflection angle and restarts the run [66].

3.4.3 Resolution of the instrument

In the present reflectometer, a Si single crystal (113) monochromator delivers 2.5Å neutrons. There is no second order contamination for the chosen reflecting plane. The monochromator crystal has a mosaic spread of about 15 arc min. For the chosen wavelength the Bragg angle is nearly 49 degrees, giving (0.1%), where λ is the spread in wavelength. The coherence length is 625Å for the neutron wave packet. Lateral inhomogeneities in a film are averaged over this length scale in a reflectivity measurement. The resolution of the instrument for small angles of scattering, as in case of reflectometry, is given by:

$$\frac{\Delta Q}{Q} \approx \sqrt{\left(\frac{\Delta\lambda}{\lambda}\right)^2 + \left(\frac{\Delta\theta}{\theta}\right)^2} \quad (3.24)$$

Where, $\Delta\theta$ is the angular divergence of the beam, which can be varied from 0.8 to 5 arc min with various combinations of Cd slits, in our instrument. The values of ΔQ are typically in the range of 0.001–0.006 Å⁻¹ [66]. The reflectivity patterns is usually taken with nearly same $\Delta Q/Q$ by changing the slit combination, as the angle of incidence increases. The reflectometer works in a unique configuration of step scan mode coupled to a linear PSD. While the sample stage rotates to scan various angles of incidence (or Q_z values), the detector is fixed, causing the reflected beam “walk” on the PSD. At each angle of incidence, the reflected beam is a Gaussian profile on the detector. This Gaussian is a convolution of the angular divergence of the beam with the position resolution of the detector. To get the

reflected intensity at one particular angle, we integrate over the Gaussian profile and subtract the background counts below it. This allows us to remove the off-specular background under the specular peak and gives true specular intensity.

3.4.4 Analysis of Specular Reflectometry data

Analysis of specular neutron reflectivity data has two major obstacles. Firstly, the phase of the scattered wave, which is required to reconstruct the scattering potential in a unique way, cannot be measured directly. Secondly, once the phase is known, the scattering potential must be recovered from the complex reflection coefficient by solving the inverse problem for 1D quantum scattering. But we can usually measure the reflected intensity only over a limited range of scattering angles. Hence we must usually opt for an indirect method, to postulate a model and then to calculate the amplitude of the reflection coefficient and compare its modulus square with the measured intensity. Using the model, we simulate the neutron reflectivity profile and calculate the difference between experimental and simulated data using some error function E_r (e.g. χ^2 minimization) [67,68]. The model can accordingly be adjusted by some optimization method to get closer agreement with the experimental data. A variety of data fitting and parameter optimization strategies exist. These techniques include Direct search, Downhill simplex, Levenberg-Marquardt method, Simulated annealing and Genetic algorithm [69].

All of the above methods run into difficulties when fitting x-ray and neutron reflectivity data. The downhill simplex and Levenberg-Marquardt methods work well for nonlinear problems because they are guided by the geometry of the error function in parameter space. However, the initial estimate of parameter values need to be very close to the optimum values. If local minima are present, the error function will be trapped in the first local minimum that it encounters. The Monte Carlo based simulated annealing methods do

not get trapped in local minima. However, they are very inefficient at searching the parameter space, since they search it randomly without taking into account the geometry of the error function. Genetic algorithms are efficient and robust technique, since they start from a large set of parameters (population) to find the global minima in parameter space. We have implemented a Genetic algorithm technique based program that has been used to analyze the neutron reflectivity data in this thesis [67].

Genetic Algorithms (GA) are the heuristic search and optimization techniques that mimic the process of natural evolution. It is based on the principle of selecting the best and discarding the poorer solutions, similar to survival of the fittest in Darwinian theory of evolution and hence draws its name from the similarity. It implements the optimization strategies by simulating evolution of species through various selection processes such as natural selection, crossover and mutation. GA is the most efficient and robust technique to find the global minima in a large parameter space [67]. A GA based optimization technique has been used to analyze the neutron and x-ray reflectivity data in this thesis.

Initially a fitness function is defined that quantifies the quality of a solution corresponding to a model with adjustable parameters. The value of this fitness function is used to rank a particular solution against all other possible solutions within a physically reasonable range of the physical parameters. The GA process determines which solutions are to be preserved and allowed to reproduce a next generation of solutions and which ones deserve to die out. The primary objective of the selection operator is to emphasize the good solutions and improve on them after eliminating the bad solutions in a population (set of solutions) while keeping the population size constant. The crossover operator is used to create new solutions from the existing solutions available in the mating pool after applying selection operator. Mutation is the occasional introduction of new features in to the solution strings of the population pool to maintain diversity in the population. Though crossover has

the main responsibility to search for the optimal solution, mutation is also used for this purpose. The mutation probability is generally kept low for steady convergence. The steps involved in working of GA is given in Fig.3.7.

For, fitting the neutron and x-ray reflectivity data, the error function should have some desirable properties like: (a) there should be a single deep global minimum and local minima, which are much less deep than the global minimum (b) It should be fast and simple to calculate (c) It should have relative insensitivity to the absolute magnitude of the data, since reflectivity data often spans many orders of magnitude.

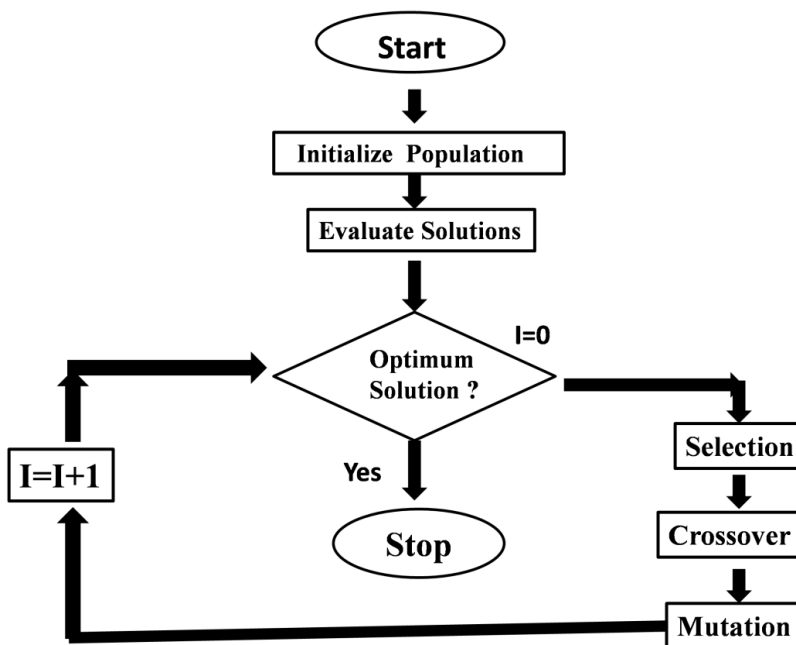


Figure 3.7: Steps involved in working of GA. (I is the number of iteration).

There are number of error functions [70] that have been applied successfully to fitting problems. Following are the functions, which we have adopted in our analysis program.

$$E_r = \frac{1}{N-1} \sum_{j=1}^N [R_{exp} - R_{cal}]^2 \quad \dots\dots\dots (3.25)$$

And
$$E_r = \frac{1}{N-1} \sum_{j=1}^N [\log R_{\text{exp}} - \log R_{\text{cal}}]^2 \dots\dots\dots (3.26)$$

With R_{exp} and R_{cal} are the measured and calculated intensity, respectively. N is the number of measured data points. The logarithmic function, Eqn. (3.26), could cope with large “Q” (momentum transfer) adequately, since the intensity of reflected neutrons falls rapidly at large Q.

The actual reflected intensity detected in an experiment is convoluted with instrumental resolution function. Therefore, for obtaining the error function, (comparing the experimental data with theatrical profile for a model) defined above, we have to either convolute the theoretical profile with instrument resolution or to de-convolute the experimental data for instrument resolution. For comparing the experimental specular reflectivity data with calculated intensity for a model, we have convoluted the theoretical intensity, $R_{\text{th}}(Q_r)$ with an appropriate instrumental resolution function [71]:

$$R_{\text{cal}}(Q) = \frac{\int_{-\infty}^{\infty} R_{\text{th}}(Q_r) \exp\{-4(\ln 2)(Q - Q_r)^2 / \beta^2\} dQ_r}{\int_{-\infty}^{\infty} \exp\{-4(\ln 2)(Q - Q_r)^2 / \beta^2\} dQ_r} \dots\dots\dots(3.27)$$

Where, β and Q are the FWHM of the Gaussian resolution function and the wave vector transfer defined as $Q = (4\pi/\lambda) \sin \theta$, where θ is the incident angle on the film and λ is the wavelength of the neutron. We compare $R_{\text{con}}(Q_r)$ with the background-corrected and normalized experimental data in the χ^2 minimization program.

3.4.5 Estimation of errors in fitted parameter

It is essential to assess the accuracy and reliability of best-fit parameter values resulted from data fitting procedure and it is an important part of the data analysis. It is difficult and computationally intensive problem to calculate the errors in each parameter with

respect to all other parameters. In the present case we have adapted technique known as “*Bootstrap method*” [69]. In this technique we generate a number of “*synthetic data set*” $\{D_i\}$ from the experimental data by randomly changing the data points within the experimental error bars in the data. The sets of synthetic data are fitted using the same optimization techniques discussed above and sets of physical parameters $\{a_i, b_i, \dots\}$ are generated. Now one can estimate average values of physical parameters $\{a_{av}, b_{av}, \dots\}$ from the sets of parameters and the fluctuation around them. The fluctuation is an estimate of the error on a particular parameter. This method is especially successful for counting experiments like reflectometry that are inherently statistical in nature

3.5 Determining stoichiometry of interface alloy layer by XRR and PNR

The present thesis has dealt extensively in characterization of interface alloy formed at mesoscopic length scale. Often these alloy layers, though crystalline, being typically few nanometers thick may not produce any diffraction peaks or the diffraction peaks are too broad to characterize the alloy phase uniquely. We have used a technique where simultaneous measurement of XRR and PNR allows one to obtain exact composition of the alloy layer [10,14].

Consider a binary system consisting of elements A and B as shown in Fig.3.8. When we anneal the system, solid state reaction occurs between the consecutive layers and an alloy layer forms at the interface, which is a mixture of both A and B. The alloy layer is of composition $mA+nB$, where values of m, n can vary from 0 to 1 and decides the stoichiometry of the alloy layer (Fig 3.8).

An XRR data reveals the electron scattering length density or ESLD as it interacts with the atomic electrons only. PNR gives the nuclear as well as magnetic scattering length density (NSLD and MSLD) for the same sample. But both the SLDs (NSLD and ESLD)

originates from the same number density (no. of scatterers per unit volume) in a medium. Hence for the binary system forming an alloy layer (A: B as $m:n$) due to inter diffusion (schematic shown below), we can have the set of equations for the alloy layer as:

$$\begin{aligned} \rho_{neutron} &= mN_A b_A + nN_B b_B \\ \rho_{x-ray} &= mr_0 N_A Z_A + nr_0 N_B Z_B \end{aligned} \quad \dots\dots\dots(3.28)$$

Where ‘ ρ ’ is the respective SLD values for x-ray and neutrons. N , b , Z are the number density, coherence scattering length for neutrons and atomic no. of reacting elements and ‘ r_0 ’ is the classical electron radius. Once ‘ $\rho_{x-ray/neutrons}$ ’ values are known, above set of linear equations can be solved for ‘ m ’ and ‘ n ’ giving the ratio of A atoms vs B to form the alloy at the interface. Neutron reflectometry together with XRR on a sample gives the stoichiometry of the alloy layer. PNR also gives the additional information of magnetization depth profile in the sample in terms of MSLD.

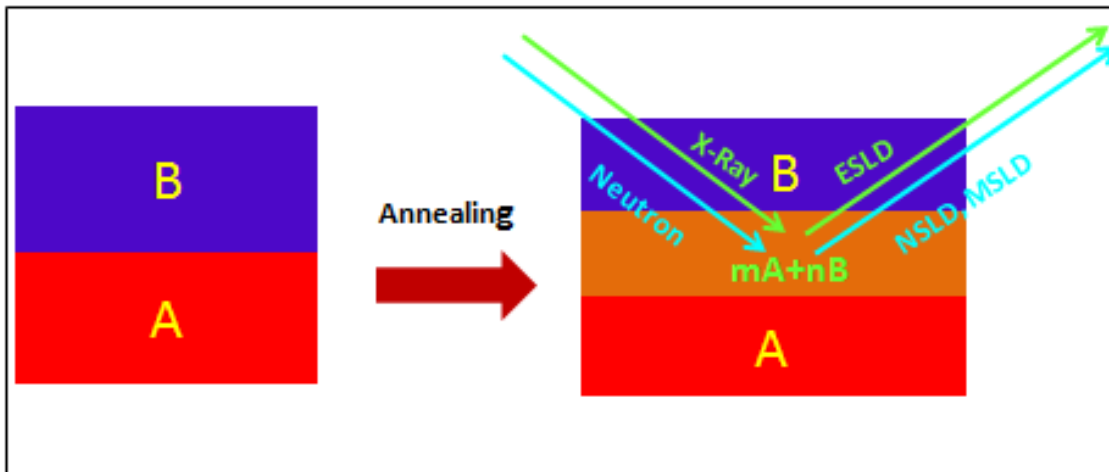


Figure 3.8: Schematic of alloy layer formation in a bilayer

Chapter 4: Nickel Aluminides (Effect of interface morphology, kinetics of alloy formation and stoichiometry dependant inter diffusion)

- 4.1 Introduction
- 4.2 Sample preparation and characterization techniques
- 4.3 Effect of interface morphology on interface alloy formation
- 4.4 Identification of a kinetic length scale
- 4.5 Stoichiometry dependent inter diffusion and structural evolution

4.1. Introduction

Nickel aluminides form an important class of intermetallics [72-76] for obvious technological interest in these compounds, since their application ranges from aeronautical industries to corrosion resistant coatings [2,71-79]. Intermetallics can be produced by several methods like cold rolling [80,81], ball milling or mechanical alloying [82,83], shock compaction and self sustained reactions [84] etc. Thermal annealing in vacuum is one of the suitable methods for inducing solid state reactions between Ni and Al with short bilayer periods to produce nickel aluminides in a multilayer thin film with alternating Ni and Al layers [7,11]. Several studies regarding nickel aluminides had been carried out theoretically [8] as well as experimentally [31] regarding sequence of phase formation in these classes of intermetallics [8,80-87]. They form several ordered intermetallics viz. Al_3Ni , Al_3Ni_2 , AlNi , and AlNi_3 in order of increasing Ni concentration according to the equilibrium phase diagram [30]. But special care has to be taken during first phase evolution in the system as it is affected by many surface and interface effects. The first alloy phase formation also affects the sequencing of subsequent phase formation in the system [31,88]. The phase diagram and the intermetallics of Ni-Al have been studied extensively and they form an

excellent platform for studying the process of alloy phase formation at the interfaces and its dependence on various physical parameters of the binary system. We have considered several Ni-Al systems in order to observe the role of interface structure in deciding the alloy phase [14], to understand the sequence of alloy phase formation and their kinetics at microscopic length scale [10]. Stoichiometry dependant diffusion mechanism and its impact on the structural parameters of the system has also been studied in details in this chapter [89].

We have taken three different Ni-Al systems for the work presented in this thesis. For observing the role of an interface, a multilayer of smaller bilayer thickness of Ni and Al was chosen. The system had a designed structure of: Si/[Ni(50Å) /Al(25Å) ×10]. In this study we observed, how the interface property leads to asymmetric alloy phase formation at the interfaces, on annealing because of different *local density* (defined as number of atoms of the reacting species available for reaction at an interface) [8,14].

Interface diffusion in thin films was mediated by annealing at lower temperatures (range ~150°C- 400°C) for fixed durations (~20 minutes – 8 hrs) [7,11]. Ni and Al both are iso-structural (fcc) at room temperature with cell parameters 3.52 Å and 4.05 Å, respectively. The melting point of Al is ~ 600°C whereas of Ni is ~1455°C. Ni and Al have different degree of diffusivity and have widely different activation energies for their diffusion [88,89]. In case of multilayer stacks, we find that thickness ratio of the respective components is an important parameter in order to obtain alloy of particular composition [88]. To prepare an alloy with 1:1 atomic ratio in a multilayer stack, we should have a thickness ratio $d(\text{Al})/d(\text{Ni})$ of 1.5:1 [11], derived from the ratio of densities of the components, where 'd' is the thickness of each layer in the multilayer stack. We have studied two Ni-Al multilayers with nominal structure (a) Si/[Ni(200Å)/Al(100Å)]×5 (sample S1) and (b)

Si/[Ni(50Å)/Al(227Å)]×5 (sample S2) with over all atomic stoichiometry in Ni:Al as 3:1 and 1:3 respectively. The aim was to study the impact of stoichiometry on the kinetics of alloy formation of Ni and Al during their inter-diffusion on annealing (150°C- 300°C). We identified a *kinetic length scale* for these systems in terms of *diffusion length* obtained from PNR and XRR reflectometry data [10]. We quantified the stoichiometry dependant micro-structural evolution in these two Ni/Al systems during annealing and obtained activation energy for alloy formation for above Ni/Al systems from Arrhenius plots in a separate study [89].

4.2 Sample preparation and characterization techniques

All the multilayer samples of Ni and Al were grown by ion beam sputtering (IBS) technique on Si single crystal substrates. The base pressure prior to deposition of the samples was about 2×10^{-9} mbar and during deposition the pressure was about 5×10^{-4} mbar with flow of Ar (purity 99.9995%). Ar^+ ions of energy 1.00 keV, produced using a radio-frequency (RF) ion beam source (Veeco 3cm RF source), were used for sputtering. The thickness of the layers were calibrated using a water cooled quartz crystal monitor prior to the deposition. The first Ni-Al multilayer sample was prepared with a nominal structure of Si/[Al(25Å)/Ni(50Å)]×10. The deposition rate for both the elements was 0.1 Å/sec. The sample was annealed at 160°C for time intervals of 1hr, 4 hrs and 8 hrs respectively. X-ray reflectivity (XRR) and Polarized Neutron Reflectivity (PNR) data were collected after each successive annealing. The XRR data were taken in a Bruker's D8 advanced laboratory source and the PNR data were collected in the NG-1 Reflectometer at NIST Centre for Neutron Research (NCNR), USA [14].

Other two multilayers a) Si/[Ni(200Å)/Al(100Å)]×5 (S1) and b) Si/[Ni(50Å)/Al(227Å)]×5 (S2), prepared by ion beam sputtering at a base pressure of

$\sim 2 \times 10^{-8}$ mbar on Si (001) substrates were chosen for studying kinetics of alloy formation and for the stoichiometry dependant studies. The samples S1 and S2 have atomic stoichiometry in Ni:Al as 3:1 and 1:3 respectively, making S1 Ni-rich and S2 Al-rich. The multilayers were annealed at 150°C, 200°C and 300°C under vacuum $\sim 10^{-4}$ mbar for a time period of ~ 40 minutes. The as-deposited and annealed samples were characterized primarily by reflectometry techniques: XRR and PNR. Other characterization techniques viz. x-ray diffraction (XRD), secondary ion mass spectrometry (SIMS), and atomic force microscopy (AFM) were also carried out to support the findings of reflectometry in different studies. Detailed characterization of the samples was carried out after each anneal. The XRR and XRD data were collected on a RIGAKU powder diffractometer with 1.54 \AA CuK_α source for these samples. SIMS measurements were performed using a HIDEN SIMS work station equipped with a quadruple mass spectrometer. The atomic force microscopy (AFM) data presented in this thesis were collected on samples of $2 \times 2 \text{ \mu m}^2$ size using a 'Solver P47H' microscope. Surface morphology of the as deposited and annealed samples at 300°C has been quantified in terms of fractal parameters [90,91] obtained from fits to height difference correlation function. A NSG10_DLC super sharp DLC tip grown on silicon with curvature 1-3 nm has been utilized in semi-contact mode. During AFM operation cantilever's resonant frequency & force constants were 213 kHz and 10 N/m respectively. The PNR data were collected at the neutron reflectometer beam line with incident wave length 2.5 \AA at DHRUVA reactor, INDIA [66].

In case of specular reflectivity the reflected intensity is measured from a sample as a function of wave vector transfer [$Q = 4\pi \sin(\theta)/\lambda$] perpendicular to the sample surface where ' λ ' is the wavelength of the incident radiation (x-ray or neutron) and ' θ ' is the angle of incidence with respect to the sample surface. The

reflectivity pattern in ‘Q’ space is the Fourier transform of the depth profile $\rho(z)$ of scattering length density (SLD) averaged over the sample area. For XRR $\rho(z)$ is proportional to electron SLD and in case of PNR, $\rho(z)$ consists of nuclear and magnetic SLDs such that $\rho(z) = \rho_n(z) \pm M(z)$ [11], where $C = 2.853 \times 10^{-9} \text{ \AA}^{-2} \text{ m/kA}$, and $M(z)$ is the magnetization (in kA/m) depth profile [11,22]. The sign (\pm) denotes the condition, whether the neutron beam polarization is parallel or anti-parallel to the applied field (sample magnetization) and are represented by the reflectivity patterns R^+ and R^- respectively.

PNR and XRR data obtained from as-deposited and annealed samples were independently analyzed by fitting model $\rho(z)$ profiles that best fits the data. The reflectivity was calculated using the dynamical formalism of Parratt [15] and parameters of the model were adjusted to minimize the value of weighted measure of goodness of fit, χ^2 [69]. By simultaneously fitting the R^+ and R^- data, the $\rho(z)^+$ and $\rho(z)^-$ SLD’s are generated, and the nuclear profiles can be extracted from $\rho_n = (\rho^+ + \rho^-)/2$. Both the reflectivity data (XRR, PNR) were fitted to obtain scattering length density (SLD) model in terms of structural parameters of the system such as, layer thickness, interface roughness and density [11,14]. Combining $\rho_n(z)$ obtained from PNR and $\rho_x(z)$ obtained from XRR data, the stoichiometry or chemical composition of the binary alloys formed at the interfaces can be obtained [11,14]. In all our measurements the specular reflectivity profile has the ‘Q’ vector normal to the film surface and the information obtained is along the depth of the film.

4.3 Effect of interface morphology on alloy phase formation

Surface energy of the reacting elements is an important parameter that affects formation of the first interface alloy phase on annealing [8]. In case of a Ni-Al

multilayer comprising 10 bilayers, with nominal structure Si/[Ni(50Å) /Al(25Å) ×10], we have observed, different surface energies of Ni and Al leads to different surface roughness at Ni on Al (Ni/Al) and Al on Ni (Al/Ni) interfaces. The Ni/Al interfaces showed higher roughness compared to Al/Ni interfaces in the as-deposited state obtained from reflectometry data. We annealed the sample at 160 °C for 1 hr, 4 hr and 8 hr and looked for the alloy composition at the interfaces. We found that asymmetry in interface roughness affects the *local density* (total number of atoms available for reaction at the reacting interfaces) leading to asymmetric alloy formation at the interfaces viz. Al₃Ni at Al/Ni and Al₃Ni₂ at Ni/Al interfaces. Effective heat of formation rule predicts that the first interface alloy layer should be Al₃Ni [8]. According to Colgan et al. [23] formation of interface alloy depends on kinetics as well as interface composition. Current work specifically highlights this issue. These interface alloy layers were found to be magnetically dead from the PNR data.

4.3.1 Results and Discussion:

Fig. 4.1 shows the PNR (R^+ and R^-) data from as-deposited and annealed Al-Ni multilayer. Closed (red) and open (blue) circles (in Fig. 4.1) depict the experimental spin dependent reflectivities R^+ and R^- , respectively. Fig. 4.1(a) show the PNR profile for as-deposited multilayer sample. PNR profiles for sample annealed at 160 °C for 1hr, 4hrs and 8hrs are shown in Fig. 4.1(b), (c) and (d), respectively. Reflectivity plots were normalized to the large Q limit of Fresnel reflectivity ($R_F = \frac{16\pi^2}{Q^4}$).

Fig. 4.2 shows the model nuclear SLD and magnetization depth profiles which fitted the measured PNR data (solid black and green lines in Fig. 4.1) from as-deposited and annealed sample. The observed Bragg peaks in PNR data clearly shows a periodic multilayer system.

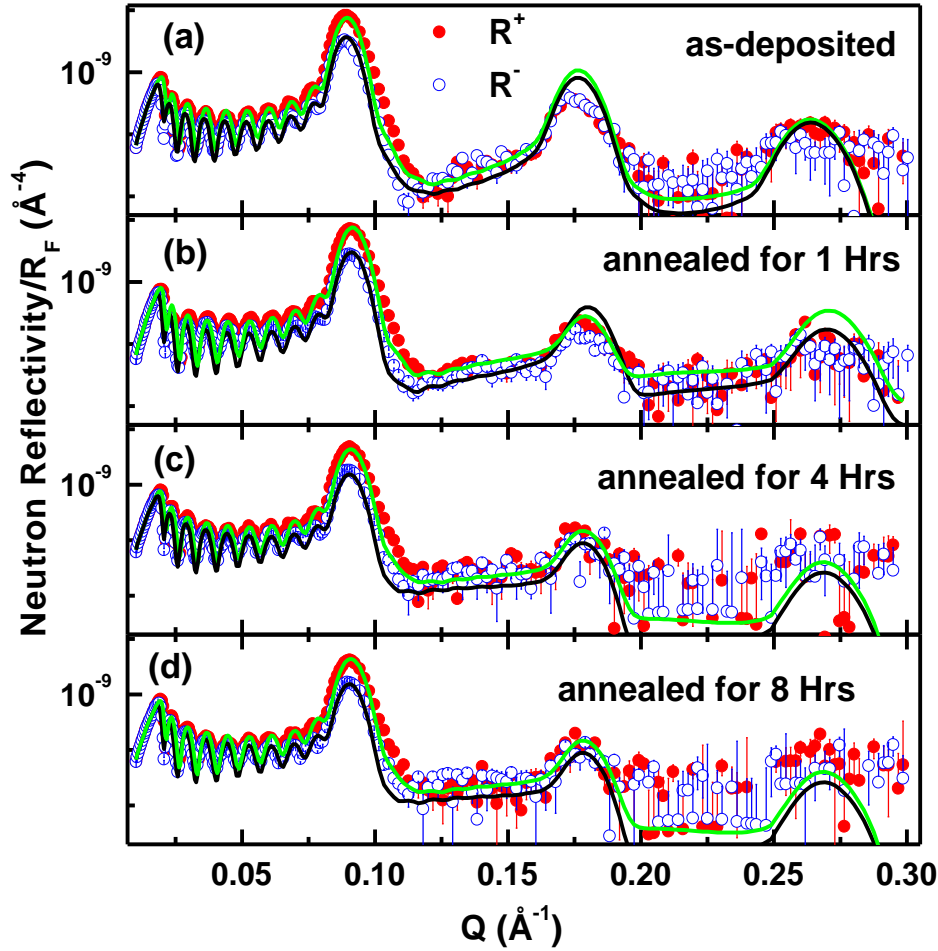


Figure 4.1: Polarised Neutron Reflectivities, R^+ (solid circles) and R^- (open circles) for as deposited (a) and sample annealed at 160°C for 1hr (b), 4hr (c) and 8hr (d) along with fits (solid lines) to the data.

We obtained an average thickness of $47 \pm 2 \text{ \AA}$ and $23 \pm 1 \text{ \AA}$ for Ni and Al layer in as-deposited sample respectively. The nuclear SLD for both the layers, Ni and Al, in as-deposited sample are close to their bulk values. We obtained a roughness of $13 \pm 2 \text{ \AA}$ and $4 \pm 2 \text{ \AA}$ for Ni on Al (Ni/Al) interface and Al on Ni (Al/Ni) interface respectively for the as-deposited sample. The fitted PNR data gives a magnetization density of $396 \pm 20 \text{ kA/m}$ for Ni layer for as deposited film, which is less than the bulk magnetic moment density of Ni ($\sim 486 \text{ kA/m}$) [92]. On annealing the multilayer at 160°C for one hour changes in neutron reflectivity pattern could be seen. There is a small shift

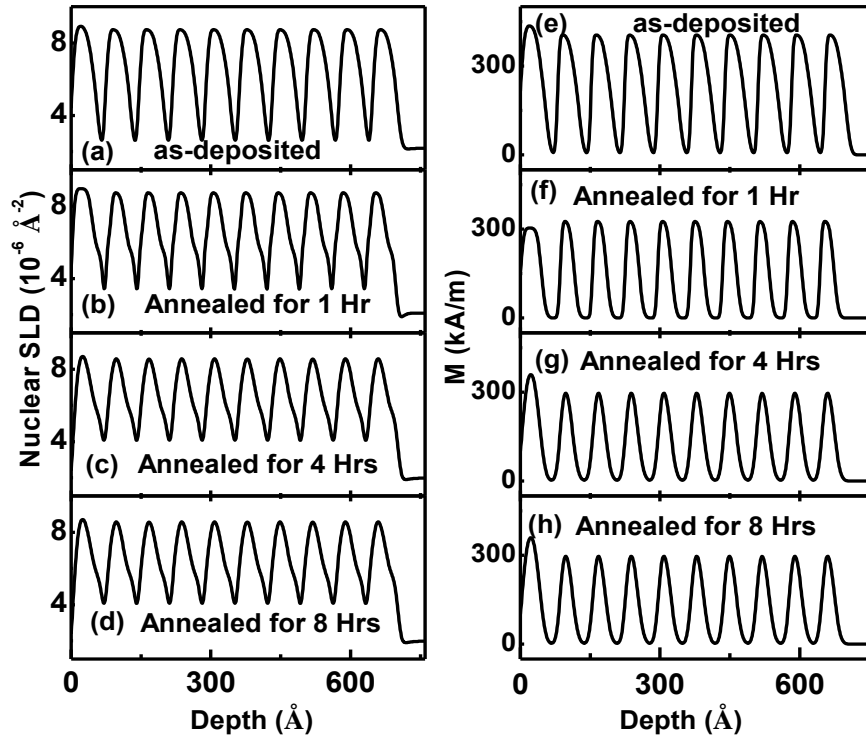


Figure 4.2: Nuclear scattering length density (SLD) profiles (a) for as deposited sample and sample annealed at 160°C for (b) 1hr, (c) 4hrs (d) 8hrs, and (e)-(h) show the corresponding magnetization (M) depth profiles.

of PNR data to higher Q value and reduction in the intensity of the Bragg peaks. This shift in PNR data on annealing is due to reduction of bilayer thicknesses due to alloying at the interfaces of the sample. The nuclear and magnetic density profile, obtained from the fits, were expanded for a single Al-Ni bilayer in Figs. 4.3 (a) and (b) respectively to highlight the change in density profiles at the interfaces due to annealing. Formation of alloy layers at interfaces occur at the expense of reduction in thickness of pure Ni and Al layer on annealing the sample. This is clear from the profiles at the interfaces. Importantly the density profiles and the alloys formed are different at the two interfaces, viz., Ni/Al and Al/Ni. Up to 4 hrs of annealing we observed increase in the thickness of interface alloy layers. However on annealing further for 8 hrs we didn't get any change in reflectivity profile, suggesting a blocking

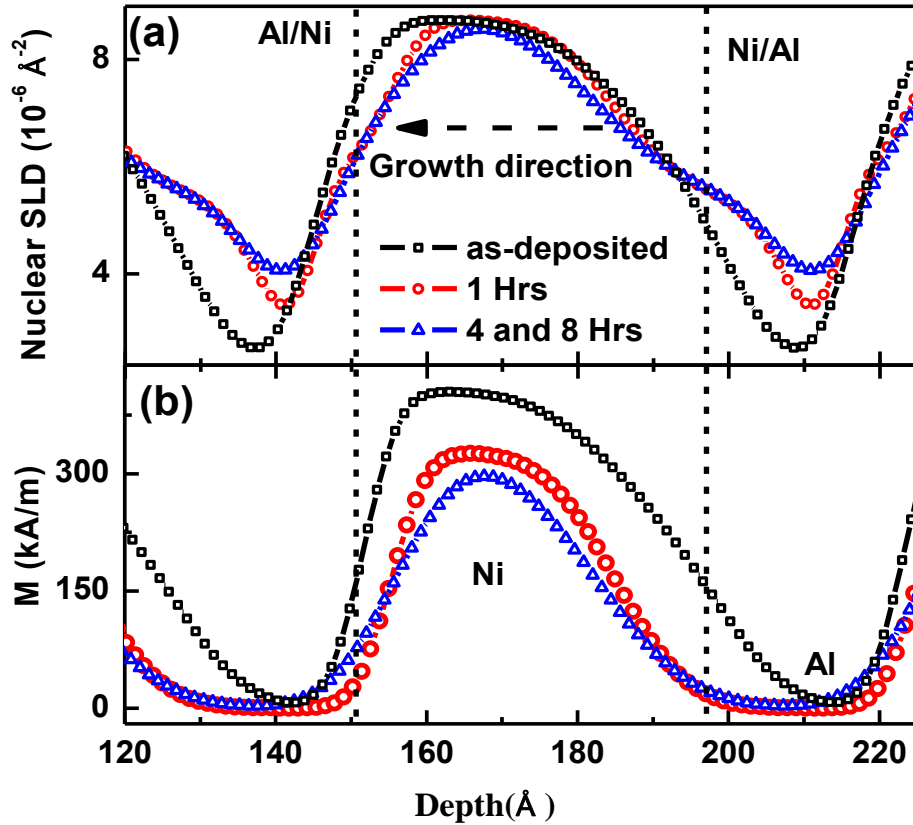


Figure 4.3: Nuclear scattering length density (SLD) depth (a) and magnetization (M) depth (b) profiles across Ni on Al (Ni/Al) and Al on Ni (Al/Ni) interfaces of the Ni-Al bilayer.

of diffusion of elements on formation of alloy layer at interfaces [11]. We consider the sample after 8 hr of annealing time has reached a stable composition at the interfaces for the given annealing temperature of 160°C.

Fig. 4.4 shows the XRR data from the as-deposited sample and sample annealed at 160°C for 8 hrs. Fig. 4.4(a) shows the experimental XRR data (closed circles) along with the fits (solid lines). Fig. 4.4(b) shows the electron SLD model for as-deposited and annealed sample obtained from the XRR data fits (solid lines in Fig. 4.4(a)). Fig. 4.4(c) shows the expanded electron SLD profile of a bilayer indicating the modification of SLD at interfaces on annealing. We obtained a thickness of 49 ± 3 Å and 22 ± 2 Å for Ni and Al layer in as-deposited sample from XRR. The electron SLD of both

layers in the as-deposited sample are nearly same as their bulk values. We obtained a roughness of $6\pm 1 \text{ \AA}$ and $12\pm 2 \text{ \AA}$ for Al/Ni and Ni/Al interfaces respectively for the as-deposited sample. The Ni/Al interface showed higher roughness compared to Al/Ni interface in both PNR and XRR. On annealing the multilayer at 160°C for 8 hrs the Ni and Al layer thickness reduced to 24 and 8 \AA , respectively. The parameters obtained from PNR as well as XRR measurements for as-deposited and sample annealed for 8 hrs at 160°C , when the interfaces have stabilized, are given in Table 4.1. It is evident from this table that the structural parameters obtained from these two independent measurements (XRR and PNR) are in good agreement with each other within error bars.

Analysis of XRR and PNR measurements on as-deposited Al-Ni multilayer clearly suggested asymmetric density profiles at Ni/Al and Al/Ni interfaces (Fig. 4.3(a) and Fig. 4.4(c)) which we can attribute to the difference in surface energy of Ni and Al. Al has a lesser surface energy (1.20 J/m^2) than Ni (2.45 J/m^2) [93]. Hence when Al is deposited on Ni, it tends to form smoother interface compared to when Ni is deposited on Al. The Ni/Al interface found to have ~ 2 times higher roughness ($\sim 12 \text{ \AA}$) as compared to Al/Ni interface ($\sim 5 \text{ \AA}$). Such asymmetric structure at interfaces is also consistent with the interface asymmetry found in Al-transition-metal bilayers [94] and Ni/Au system [95]. Bigault et al. [95] suggested that such an asymmetry is also probable due to dynamical segregation of element during the growth of the film, which means island formation of two components, causing density variance.

We observed alloy formation at interfaces after one hour of annealing. On further annealing the sample up to 4 hrs at the same temperature, the alloy layer grew in thickness without change in composition of the alloy. However we didn't observe further change in multilayer structure on annealing the sample beyond 4 hrs. This is similar to

Table 4.1: Physical parameters obtained from PNR and XRR measurements of as-deposited sample and sample annealed at 160°C for 8Hrs. The errors on the parameters are in the range of 5-10%.

Parameters from PNR measurements							Parameters from XRR measurements					
[d = thickness (Å), ρ_n = nuclear scattering length density (10^{-6} \AA^{-2}), σ = roughness(Å)]							[d = thickness (Å), ρ_x = electron scattering length density (10^{-5} \AA^{-2}), σ = roughness(Å)]					
Layers	As-deposited			Annealed			As-deposited			Annealed		
	d	ρ_n	σ	d	ρ_n	σ	d	ρ_x	σ	d	ρ_x	σ
Alloy	-	-	-	10	6.2	6	-	-	-	12	5.1	8
Ni	47	8.9	4	26	8.9	6	49	6.1	6	24	6.0	6
Alloy	-	-	-	27	5.6	6	-	-	-	26	4.3	7
Al	23	2.2	13	6	2.3	5	22	2.2	12	8	2.1	7

the blocking effect we observed in our previous study [11]. As mentioned earlier, using the electron SLD (from XRR) and nuclear SLD (from PNR) for alloy layers at interfaces we calculated the exact composition of alloys. We found the Al:Ni ratio of alloy layers at Al/Ni and Ni/Al interfaces are $\sim 3:1$ and $3:2$, respectively, suggesting formation of Al_3Ni and Al_3Ni_2 alloys at these interfaces. Such asymmetric alloy formation at interfaces in present sample is in contrast to our previous study on Al-Ni multilayer with thickness ratio, $d(\text{Al})/d(\text{Ni})$ of 1:1[11], where we observed symmetric alloy (Al_3Ni) formation at the interfaces in first hour of annealing. The sample in our previous study also did not show any difference in roughness for the two interfaces. This strongly indicates that the two different phases we observed at the two interfaces are due to the difference in their roughness.

We forward an explanation based on effective heat of formation where Pretorius et al. [8] has shown clearly that the effective heat of formation depends on the

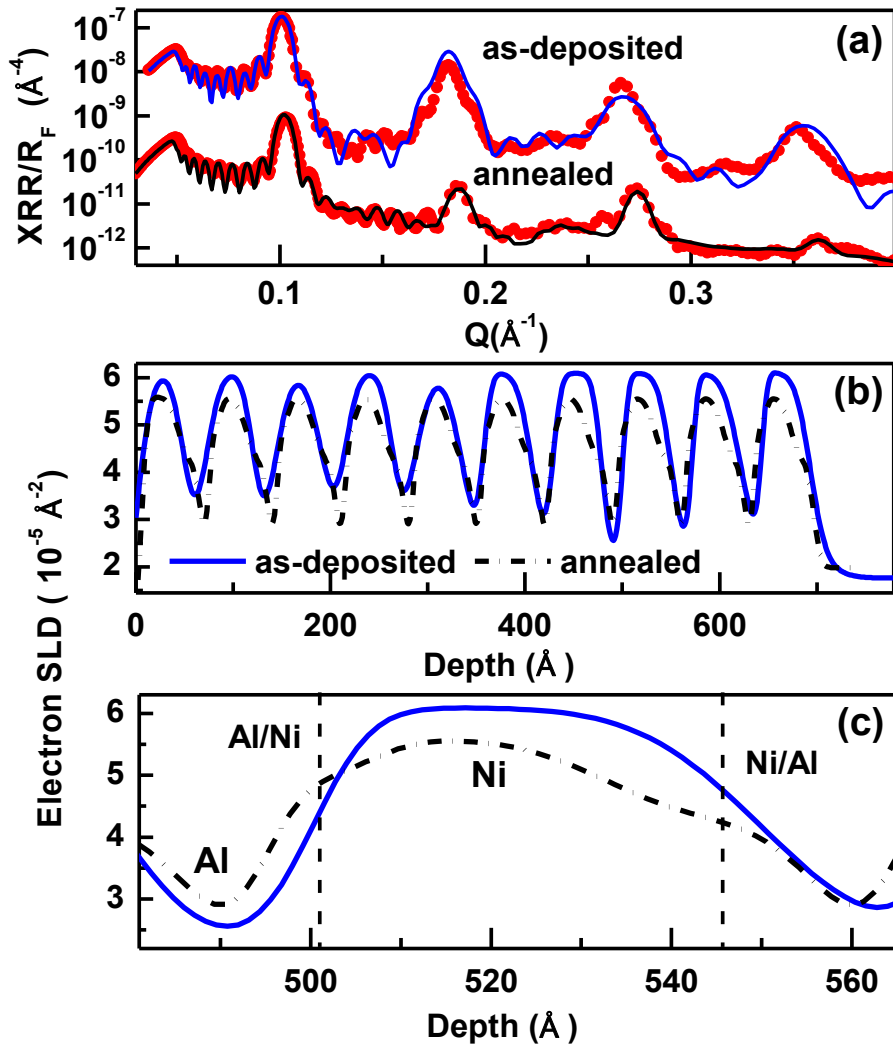


Figure 4.4: (a) X-ray reflectivity (XRR) data from the as-deposited sample and sample annealed at 160°C for 8 hrs. (b) Electron scattering length density (SLD) profile of the sample which gave best fit to XRR data (Fig. (a)). (c) represents the Electron SLD profile across Ni/Al and Al/Ni interfaces of a Ni-Al bilayer.

relative concentration of Ni and Al at the interfaces. They showed that for a relative atomic ratio of 96.5:3.5 for Al:Ni, same as that for the lowest temperature eutectic in Ni-Al phase diagram, Al_3Ni phase forms first. Since Al is more mobile species of the two, it is reasonable to assume that supply of Al will maintain this ratio during low temperature annealing. In the present sample the overall atomic ratio is 1:3 for Al:Ni for the designed bilayer. If such a concentration ratio is available to the interface for alloy formation, the

effective heat of formation is -23.75 kJ/g at. for Al_3Ni_2 and -12.7 kJ/g at. for Al_3Ni [8]. This makes formation of Al_3Ni_2 more favourable. Though for the stoichiometric ratio of Al:Ni equal to 1:3, Ni_3Al has the lowest effective heat of formation (-41 kJ/g at.), there is a large thermal barrier towards formation of this Ni rich phase. Interestingly even if there are 10% Ni atoms to 90% Al atoms present at the Ni/Al interface the effective heat of formation for Al_3Ni and Al_3Ni_2 are quite close, approximately -15 kJ/g at., if we use the argument of Pretorius et al. [8] for evaluating heat of formation based on local density.

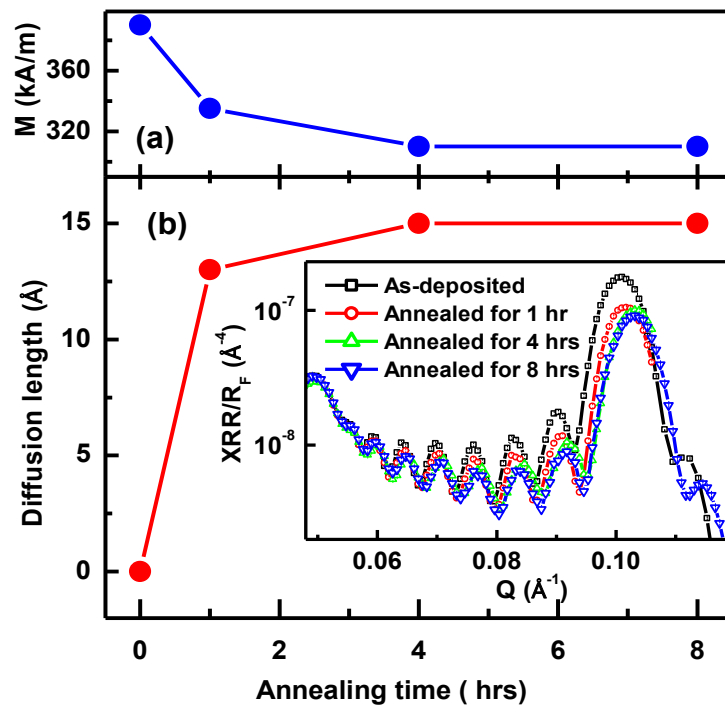


Figure 4.5: Variation of magnetization (M) of Ni layer (a) and diffusion length (b) as a function of annealing time. Inset of (b) shows the X-ray reflectivity (XRR) data across first order Bragg peak for as-deposited sample and sample annealed at 160°C for different times.

The authors feel that the large roughness of Ni/Al interface does not allow a smooth layering of Ni on Al and might give rise to a local density fluctuation favouring formation of Al_3Ni_2 at this interface. This is how the interface roughness and the phases form in the present experiment are possibly related. Fig. 4.5 (a) show the variation of magnetization of pure Ni layer vs. annealing time obtained from PNR measurements. We observed a

reduction of Ni magnetization from 396 kA/m (in case of as-deposited sample) to 335 kA/m within first hour of annealing of the sample, which further reduces to 311 kA/m on annealing the sample at the same temperature for 4 hours. Magnetization in the Ni layer decreased on annealing due to diffusion of non-magnetic Al atoms in the Ni layers. The total change in magnetization of Ni in bulk of Ni layer is ~ 21%. PNR results also suggested that the alloy layer at interfaces are magnetically dead. On further annealing the sample for four hours, thickness of Ni and Al layers reduced by of 44% and 74%.

Reflectometry techniques are useful to study the diffusion at the microscopic level (for smaller diffusion lengths ~ tens of Å) and can be used to obtain diffusivity at the interfaces [94,95]. Diffusion length is an important quantity for diffusion studies describing the average displacement of atoms during an isothermal anneal of time period 't' which is given as $\sqrt{6Dt}$, where 'D' is the diffusion constant. Isothermal annealing of the multilayers in an inert atmosphere at elevated temperatures leads to inter-diffusion of the two elements (Ni and Al), with changes in the composition (formation of alloy layer at interface) of sample at interface. Once interface alloy layer starts forming, the contrast in scattering length density between the layers reduces. This is the cause of decrease in Bragg peak intensity in XRR data as shown in the inset of Fig. 4.5 (b). From the decrease in intensity of the Bragg peak, diffusivity (D) can be calculated according to the expression, $\ln[I(t)/I(0)] = -8n^2\pi^2Dt/d_{bl}^2$ [9,96,97], where $I(t)$ and $I(0)$ are the intensities of the n^{th} order Bragg peak after annealing for time 't' and in the as-deposited sample respectively, d_{bl} is the bilayer thickness. We have used first Bragg peak in XRR measurements (inset of Fig. 4.5(b)) to calculate the diffusion length of elements at the interfaces. Diffusion lengths of ~13Å and ~15 Å were obtained after annealing the sample for 1 hr and 4 hrs respectively, which is consistent with the thickness of alloy

formed on annealing. Fig. 4.5(b) shows the variation of diffusion length as a function of annealing time. The diffusion of elements was rapid for first 1 hr of annealing which significantly slowed down after 4 hrs of annealing. The “blocking effect” is most likely due to the thermal barrier, which inhibits Ni diffusion at such low temperature of annealing.

4.3.2 Summary

We carried out depth dependent structure and magnetic properties of a Al-Ni multilayer (with thickness ratio of $d(\text{Al})/d(\text{Ni}) = 1:2$) in as-deposited and annealed conditions (at 160°C for 1-8 hrs) using XRR and PNR in the present work. The as-deposited multilayer showed asymmetric roughness at the interfaces. On annealing the sample at 160°C for 1hr we observed asymmetric alloy formation at interfaces, which might have resulted from asymmetric roughness in the as-deposited sample. Detailed analysis of XRR and PNR suggested the compositions of alloys are Al_3Ni and Al_3Ni_2 at Al/Ni and Ni/Al interfaces respectively. PNR results suggested that alloy layers are magnetically dead. Present study also shows that how the interface roughness might cause changes in effective heat of formation and dictates the possible interface alloy phases.

4.4 Identification of a kinetic length scale

In a series of experiments Colgan et.al. demonstrated that the first phase formed in Ni-Al systems is always NiAl_3 in line with Bené’s rule [31,87]. In case of annealing at low temperature, the mobility of an element dictates its availability for alloy formation at a certain depth. Between Ni and Al, Al has higher mobility compared to Ni. This suggests kinetics rather than thermodynamics is responsible for deciding the interface alloy phase [23]. Our previous study also states, the heat of formation of an intermetallic depends on the *local density* of the component, instead of the bulk value, to form an alloy phase at the

interface [8,14]. An important question arises from the above studies that can one define the “*local density*” in terms of a kinetic length scale? One possible answer is that at any temperature this length scale will be related to the “*diffusion length*” of the reacting species (here Ni and Al). However, a detail depth dependent structure and as a function of annealing temperature with samples of different Ni:Al stoichiometry is required to quantify this conjecture.

Two multilayer samples comprising five periodic bilayers of Ni and Al on Si substrate with nominal structure: a).Si/[Ni(200Å)/Al(100Å)]×5 (sample S1) and b).Si/[Ni(50Å)/Al(227Å)]×5 (sample S2) were studied. The thickness ratio of Ni, Al were chosen such that the overall stoichiometry of Ni:Al were 3:1 and 1:3 in S1 and S2 respectively. This means the systems S1 and S2 will form intermetallics Ni₃Al and NiAl₃, if we make homogenous alloy from these multilayers by heating. XRD measurements from as-deposited and annealed samples indicated crystalline phase of intermetallic alloys, however the Bragg peaks were too broad to identify their exact composition. XRR and PNR measurements were used to identify the exact composition of alloy at the interfaces after annealing the samples. We calculated the diffusion length from PNR Bragg peaks and observed that the thickness of the interface alloy phase matched well with this diffusion length scale for both the samples. We estimated the diffusion lengths for Ni and Al separately, from Darken’s combined diffusion expression [98]. It is observed that even over short length scales, kinetics of the components takes precedence over thermodynamics at low temperatures annealing and the first phase formed was NiAl₃ in both the samples [23].

4.4.1 Results and Discussion

XRD data from sample S1 and S2 are shown in Fig. 4.6. We have marked the Bragg

peaks corresponding to Ni, Al and also from different binary alloys of Ni and Al at the bottom of Fig. 4.6. XRD pattern for as-deposited and annealed (150°C and 300°C) samples of S1 and S2 are shown in Fig. 4.6(a) and (b), respectively. We have performed SIMS on our samples to observe qualitatively how the periodic structure gets modified by annealing [99-101]. The SIMS data is shown in Fig. 4.6 (c) and (d) for the as deposited states of S1 and S2 respectively. Corresponding annealed profiles are given below in Fig. 4.6(e) and (f) respectively. The Bragg peaks for as-deposited samples corresponds to fcc Ni and fcc Al [102] in the XRD profile. The SIMS pattern from samples S1 (Ni-rich) and S2 (Al-rich) show oscillations of Ni and Al densities indicating periodic structure of the multilayer for the as-deposited samples. The SIMS pattern (in Fig. 4.6(c)-(f)) clearly shows that Al mobility at 300°C completely destroys the periodic oscillations corresponding to Al layers in both S1 and S2. Since S1 is rich in Ni, oscillations due to Ni layers can be seen in SIMS, even after annealing at 300°C. This is corroborated in XRD data by the presence of a strong Ni peak after annealing S1 at 300°C. In the Al-rich sample S2, the structure gets strongly modified after the first anneal at 150°C. Both Ni and Al peaks disappear from XRD pattern of sample S2 after annealing and peaks corresponding to alloy phases appeared. The peaks corresponding to alloy phases are broad for both S1 and S2 in the XRD pattern and the possible phases are indicated in Figs. 4.6(a) and (b), respectively.

Further annealing at 300° C does not show any significant structural change in S2, but indicates sharpening of the crystallographic Bragg peaks signifying growth in grain size. The XRD patterns are able to identify the modifications in the samples on annealing. However the exact composition of alloy is difficult to identify from XRD pattern for such thin films. XRR and PNR have been used simultaneously to obtain the composition of the interface alloys as described below. PNR

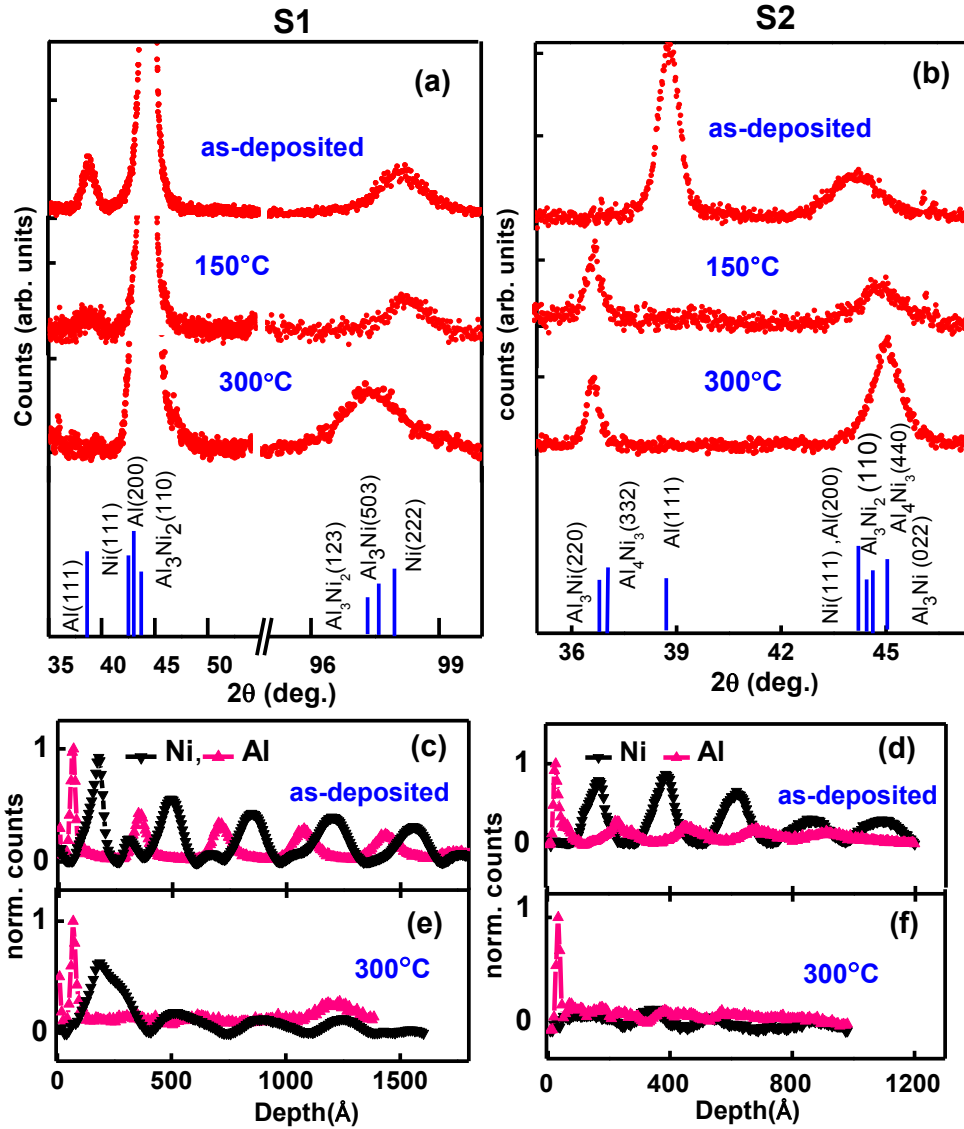


Figure 4.6: (a) and (b) shows x-ray diffraction (XRD) pattern from as-deposited and annealed (at 150°C and 300°C) samples S1 and S2, respectively, (c),(d) shows SIMS profiles for as-deposited samples for S1 and S2 respectively, (e),(f) shows corresponding annealed profiles for SIMS at 300°C.

also allows one to obtain magnetic depth profile of the sample and to find out the magnetic properties of the interface alloy layer. XRR measurements for as-deposited and annealed samples of S1 and S2 are shown in Fig. 4.7(a) and (b), respectively. The solid lines are fits to the XRR data. XRR measurements have been carried out on larger samples as compared to the incident beam size. Therefore no geometrical correction (e.g. foot print effect) on data was required.

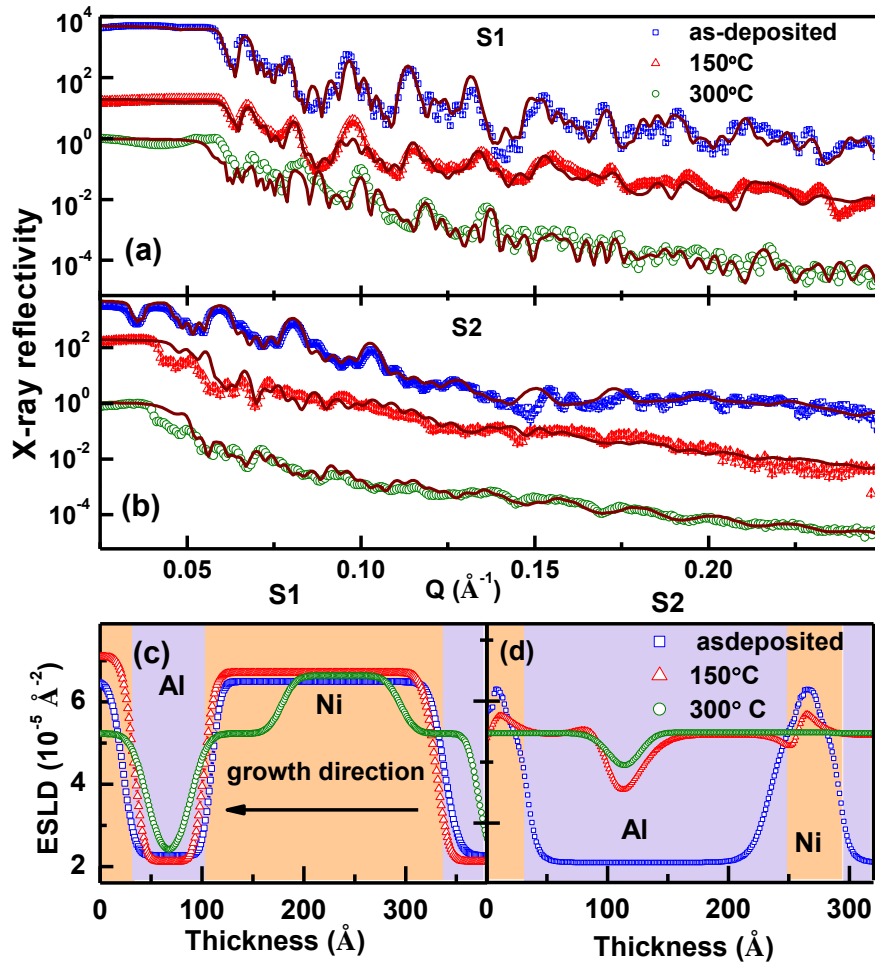


Figure 4.7: (a) and (b) show x-ray reflectivity (XRR) profile from as-deposited and annealed (at 150°C and 300°C) samples S1 and S2 respectively, (c) and (d) show corresponding electron scattering length density (ESLD) profiles from fits to the XRR data.

The fitted electron scattering length density (ESLD) profile of one bilayer (our multilayer samples consisted of 5 such bilayers) for samples S1 and S2 are shown in Fig. 4.7(c) and (d), respectively. We obtained a thickness of 210 ± 10 Å and 95 ± 5 Å for Ni and Al layer in as-deposited sample S1 from the analysis of XRR data. The thickness of Ni and Al layers in as-deposited sample S2 was 45 ± 4 Å and 212 ± 7 Å respectively while the ESLD for Ni and Al layers in both the samples were close to their bulk values. The XRR and PNR data were analyzed using a Genetic Algorithm based optimization program developed by us [103]. The XRR and PNR data were fitted independently using the same

physical model, so that that the density profiles obtained from both the measurement were matching within allowed error bars (5-10%).

In case of XRR the data was recorded over a much larger 'Q' range and we ensured that we obtained a reasonable fit over the entire 'Q' range for both PNR and XRR with the same physical model. Also one needs to fit the data over 3 to 4 orders of magnitude in XRR and PNR. In this attempt we have accepted marginal deviations between the fitted data and the experimental data in XRR for some data sets near the critical edge. On annealing sample S1 at 150°C we observed small reduction in intensity of multilayer Bragg peaks and shift to higher Q values in XRR pattern. This indicates an overall compaction of the bilayers in the sample, which is possibly due to elimination of microscopic voids that are present in the as-deposited film [104,105]. The Bragg peaks remained well defined up to higher order on annealing the sample, indicating that the periodic structure was retained in S1, similar to the observation from SIMS measurements. The ESLD model for annealed sample S1 at 150°C [Fig. 4.7(c)] suggest a small reduction in thickness of Ni and Al layers as a result of densification of the layers [104].

However, the modulations of oscillations in XRR pattern at higher Q suggest increase in interface roughness as we move away from the substrate interface towards the surface. On further annealing the sample S1 at 300°C we observed alloy layers forming at interfaces with an ESLD of $(5.2 \pm 0.36) \times 10^{-5} \text{ \AA}^{-2}$ and thickness $80 \pm 4 \text{ \AA}$. The thickness of the remaining Ni and Al layers reduced to $120 \pm 6 \text{ \AA}$ and $40 \pm 5 \text{ \AA}$ respectively.

On the other hand a rapid alloying at interfaces was obtained on annealing the sample S2 at 150°C itself. We get poor fittings near critical angle for annealed sample of S2 to obtain an overall fit within allowed error bars of PNR fit. ESLD profile for annealed sample S2 at 150°C shows formation of alloy layer with thickness $110 \pm 7 \text{ \AA}$ at

the interfaces, which was not seen in S1. As a result the thickness of Ni and Al layers reduces to 6 ± 2 Å and 15 ± 2 Å respectively. The ESLD of the alloy layer was found to be $(5.15\pm 0.33)\times 10^{-5}$ Å⁻². For S2 the interface alloy formation was nearly complete after annealing at 150°C [Fig. 4.7(d), red symbols]. On annealing the sample S2 further at 300°C the film becomes more homogeneous. Except a small signature of the remaining Al layer of thickness 6 ± 2 Å and Ni layer thickness was almost zero [green symbols in Fig. 4.7(d)]. The difference between S1 and S2 is understandably due to their overall composition and higher mobility of Al with respect to Ni. We obtained the ESLD value as $(5.2\pm 0.37)\times 10^{-5}$ Å⁻² for the alloy layer in S2 after annealing at 300°C, similar to what we obtained in S1.

The PNR data from as-deposited and annealed samples, S1 and S2 are shown in Figs. 4.8(a) and (b), respectively. Figs. 4.8(c) and (d), show the fitted model nuclear scattering length density (NSLD) depth profiles for S1 and S2 respectively. Figs. 4.8(e) and (f), shows the corresponding magnetisation profiles. These SLD depth profiles fit the measured PNR data (solid black and green lines in Fig. 4.8(a) and (b)) from as-deposited and annealed samples. Since the ESLD in XRR and the NSLD in PNR both originate from the actual physical density profile in the samples, they should be consistent with each other. The thicknesses of Ni, Al and alloy layers obtained from PNR data for as-deposited and annealed samples of S1 and S2 are in good agreement with XRR measurements. For S1 the magnetisation of Ni in the as-deposited state found to be 278 ± 16 kA/m which increased to 319 ± 19 kA/m after annealing at 150°C, possibly due to densification of the system [105]. But after annealing at 300°C the magnetisation of Ni decreased to 192 ± 13 kA/m due to higher degree of alloying.

In case of S2 the magnetisation of Ni on annealing reduced to almost zero from from 481 ± 28 kA/m for as-deposited sample. These magnetisation values

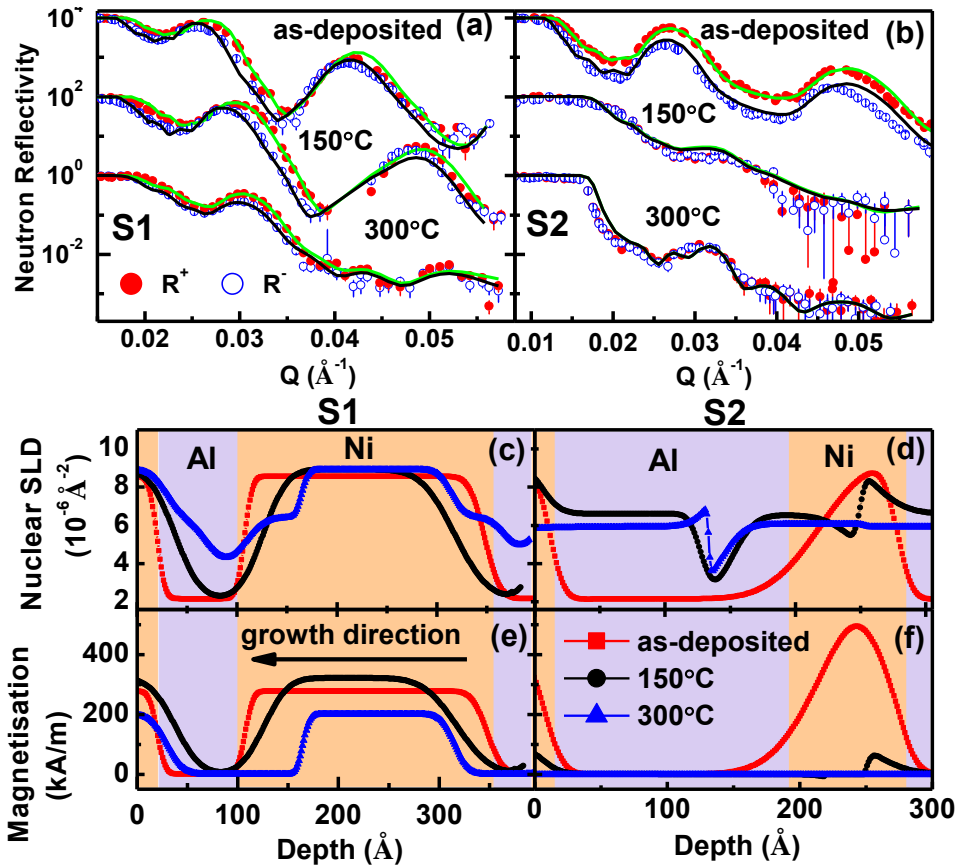


Figure 4. 8: (a) and (b) show polarized neutron reflectivity (PNR) profiles R^+ (red solid circles) and R^- (blue open circles) from as-deposited and annealed (at 150°C and 300°C) samples S1 and S2 respectively, (c) and (d) show corresponding nuclear scattering length density (NSLD) profiles for samples S1 and S2, respectively, (e) and (f) show magnetization depth profiles for samples S1 and S2, respectively.

obtained from PNR data analysis reveal that being richer in Al, S2 experiences a sharp fall in magnetisation value of Ni due to higher degree of inter-diffusion of Al in Ni on annealing, whereas this fall is lesser in S1.

We had shown in our earlier work using the ESLD and NSLD from independent XRR and PNR measurements, one can obtain exact value of the interface alloy composition [equation 2 in Ref. 13]. Using same formalism we could identify the interface alloy phase as NiAl_3 for both the samples after annealing. NiAl_3 formed at 150°C for S2 and continued to be the only interface alloy even after annealing at 300°C.

There are no significant changes in the structural parameters obtained after annealing at these two temperatures. Albeit in sample S2 the alloy formation is nearly complete after annealing at 150°C, but in S1 the interface alloy formed only at 300°C. This distinction is due to the difference in amount of Al present in the two systems which is the major diffusing species in these samples. We may conclude that the first alloy phase formation in both these systems are in agreement with Benés rule [87]. However, the heat of formation in case of S1 should favour formation of Ni₃Al thermodynamically [8], if we consider the over all stoichiometry. But in both S1 and S2, the interface alloy layer found to be NiAl₃ and the kinetics of the constituents dictate the alloy at the interface as observed by Colgan et al., [23,31] instead of thermodynamics. This interface alloy layer found to be magnetically dead (zero magnetisation) for both the systems from PNR analysis

This brings the question to the fore, whether a length scale exists, decided by the kinetics, which dictates the local density? We attempt to resolve this issue. In case of periodic multilayers, the interface alloying causes reduction of the Bragg peak intensity in reflectivity data. It is evident from the PNR profile of S1 and S2 in Fig. 4. 8(a) and (b). One can estimate the overall diffusion constant of a system using the relation $I(Q) = I_0 e^{-DQ^2t}$ [9] where I_0 was the intensity of the Bragg peak before annealing and $I(Q)$ is the intensity after annealing. ‘ D ’ is the diffusion constant and ‘ Q ’ is the momentum transfer and ‘ t ’ is the annealing time. This equation had been used extensively for estimating diffusion constants [11,14]. In the present case the diffusion constant is due to both the diffusing species Ni (D_{Ni}) and Al (D_{Al}) and is a composite one (D). This allows one to compute a diffusion length L_D given by: $L_D = \sqrt{6Dt}$ [9,96]. We obtained the diffusion lengths as $\sim 78 \text{ \AA}$ and $\sim 122 \text{ \AA}$ from the above relation for S1 and S2

respectively. These estimates are close to the fitted thickness of the interface alloy layers from the reflectivity data, $\sim 80 \text{ \AA}$ and $\sim 110 \text{ \AA}$ for S1 and S2 respectively. This observation indicates that at the initial stage of diffusion, the growth of interface alloy layer is decided primarily by the diffusion length. We also obtained approximate values of individual diffusion lengths of Ni and Al, for the systems neglecting the effect of all other parameters. To find these individual diffusion lengths we used Darken's equation [98]. It states that the composite diffusion constant (D) of a binary system is related to that of the constituent elements by the equation: $D = N_{Ni}D_{Ni} + N_{Al}D_{Al}$ where N_{Ni} and N_{Al} are the respective fractions of the atoms taking part in diffusion and D_{Ni} and D_{Al} are the corresponding diffusion constants. To calculate D_{Ni} and D_{Al} knowledge of the participating fractions N_{Ni} and N_{Al} are required. In absence of any other indicator, we used the overall stoichiometry ratio in our samples, which will provide an upper bound for the diffusion constant of Ni, which has lesser mobility at the temperatures of annealing. We obtained a value of L_D as $\sim 33 \text{ \AA}$ and $\sim 140 \text{ \AA}$ for Ni and Al respectively using Darken's equation and from the estimates of the composite ' D ' for S1 and S2. In light of these estimates, we conclude that even if the thickness of Ni layer is approximately $\sim 210 \text{ \AA}$ and thickness of Al layer is $\sim 95 \text{ \AA}$ for S1 in the as-deposited state, the diffusion length of Ni is at best $\sim 33 \text{ \AA}$. This length dictates the local density of Ni at the alloying front since Ni migration can occur only from this depth of Ni layer and favours formation of NiAl_3 initially. This length scale is decided by the kinetics of the components that is Ni and Al in the present case. This Diffusion length modifies the heat of formation as the local density is different from the overall stoichiometry following the assumption of Pretorius et al. [8]. It indicates that the formation of NiAl_3 is due to kinetics even if Ni_3Al is thermodynamically favoured in S1. Formation of NiAl_3 in S2 is quite evident as it is favored by both kinetics and thermodynamics [23,87]. This study clearly demonstrates

that diffusion length is the unique length scale, obtained from kinetics of the constituents, which decides the local density and governs composition of the interface alloy.

Another interesting aspect has been shown in a schematic of the constituent layers for the as-deposited and for the samples annealed at 300°C in Fig. 4.9. In this diagram we have shown the thickness variation of Ni and Al layers for a bilayer in the as-deposited and annealed state at 300° C, assuming the film/substrate interface as a fixed reference line at the right. The length of each block has been drawn proportional to the corresponding thickness of the layers in the multilayer film. We assumed sharp boundaries at the interfaces, ignoring interface roughness. The film/substrate interface provides a reference boundary, which does not shift due to alloying, to compare the as-deposited and the annealed films with respect to the growth of the alloy layers. The vertical black dashed lines, at the interfaces of the as-deposited films may be considered as “*virtual Kirkendall markers* [106,107]. After annealing, keeping the film/substrate interface fixed, we have again shown the Ni layer, alloy layer and the Al layer for both S1 and S2 along with the markers. We observed interesting differences between S1 and S2 with respect to these virtual markers.

In this case the Al layer has shrunk fairly symmetrically with respect to the markers after annealing. It is predicted that since in case of S1, the thickness of the Al layer was less than its diffusion length, it could diffuse to either direction (left or right of the Al layer in Fig. 4.9) limited by its diffusion length. It is also observed that higher amount of Al consumption for alloy formation was from Al present close to Ni/Al interface than from Al/Ni interface, which is understandable from surface energy considerations [10]. Since Al has a lower surface energy than Ni, [93]. Al/Ni interface has lower energy and hence more stable than Ni/Al interface. But in case of S2, the Al layer thickness was $\sim 212 \text{ \AA}$

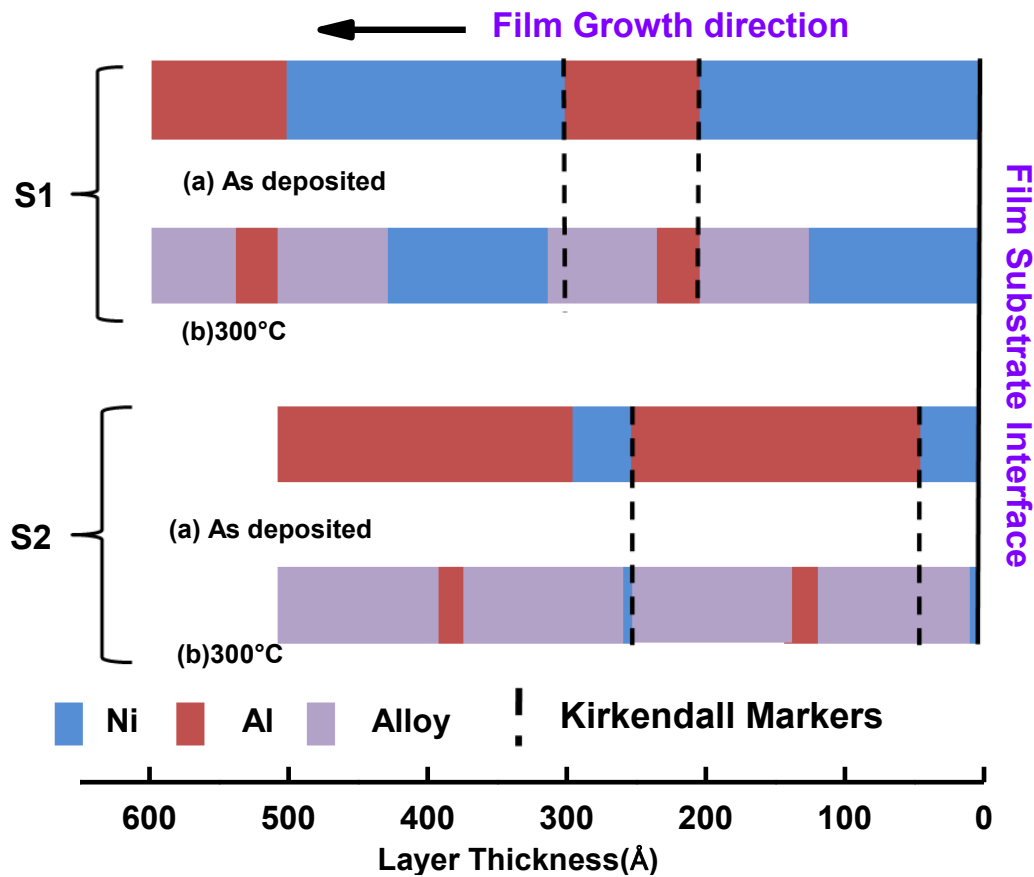


Figure 4.9: Block diagrams for two bilayers in S1 and S2 for the as-deposited samples and after annealing the same at 300°C. Lengths of the coloured blocks are proportional to the thickness of the corresponding elements and the alloy layers (after annealing). The ‘virtual Kirkendall markers’ allows to compare the position of the interfaces before annealing and the growth of the alloy layers after annealing with the substrate-film interface as a fixed reference line.

(larger than its diffusion length), hence the formation of alloy layer consumed Al from nearer interfaces and the reduction of Al layer was fairly symmetric.

4.4.2 Summary

In current work, we have studied two ultra-thin multilayer films of Ni and Al alternating layers, with thickness ratios such that the overall stoichiometry of these films were that of Ni_3Al and NiAl_3 . These films were annealed at temperatures in the range of 150°C to 300°C. Using x-ray and neutron reflectivity we could obtain the exact stoichiometry of

the interface alloy layer as NiAl_3 . Moreover from PNR Bragg peak intensities we estimated the diffusion constant at the Ni-Al interfaces and individual diffusion lengths for Ni and Al from Darken's equation. The diffusion length of Ni was about 33 Å, compared to 140 Å for Al. It is observed that, this diffusion length (L_D) decides the availability of the elements at the alloying front and changes the local density favouring the phase which is kinetically favoured i.e. NiAl_3 for both our samples compared to thermodynamically favoured phase (Ni_3Al in S1). This allows us to conclude that the definition of local density should be the material available within diffusion length of the element under consideration. Also in case of the sample with Al layer thickness less than its estimated diffusion length, we showed with the help of "Kirkendall markers" that the Al consumption is asymmetric with respect to the two interfaces of the Al layer.

4.5 Stoichiometry dependent inter diffusion and structural evolution

Nickel and Aluminum are both iso-structural (fcc) at room temperature and the lattice constant of Ni is 13% smaller than Al. The melting point of Al is ~ 600°C whereas of Ni is ~1455°C, hence they have widely different activation energies for their diffusion [88]. This makes the diffusion constant strongly dependent on overall stoichiometry of the multilayer sample, which in turn gives rise to different kinetics of phase formation, depending on stoichiometry. We attempted to quantify the changes in structural parameters of two Ni-Al systems (discussed in section 4.4) at different annealing temperatures in this study.

Here we report the evolution of crystallite size, alloy layer thickness at the interfaces and magnetic moment of Ni atoms in individual layers as a function of annealing temperature, using XRD, XRR and PNR measurements. Using XRD we estimated the increase in crystallite size of alloy phase from 50Å to 170Å in Ni rich

sample (S1) and 60Å to 88Å in Al rich sample (S2) on increasing the annealing temperature from 150°C to 300°C. Surface morphology of the samples before and after annealing was obtained by AFM technique. The observed changes in crystallite sizes obtained from XRD analysis are proportional to the corresponding changes in height-height correlation length as measured from AFM. Using PNR we also measured the changes in the magnetic properties of samples on annealing which clearly suggest formation of a nonmagnetic alloy layers at the interfaces. Diffusion constants, obtained from PNR measurements at different temperatures of annealing, have been used to measure the activation energy of the systems. Diffusion constant of the Al-Ni multilayer systems, depends strongly on the overall stoichiometry in the films, leading to widely different activation energies for alloy formation in the two multilayers studied in this part of our work.

4.5.1. Results and Discussion

Fig. 4.10 shows the XRD patterns from samples S1 and S2. XRD data from as-deposited and annealed samples at 150°C, 200°C and 300°C for S1 and S2 are shown in Fig. 4.10 (a) and Fig. 4.10 (b), respectively. For the as-deposited sample S1, we observed Bragg peaks at $2\theta \sim 38.8^\circ$, 44.3° and 98.2° corresponding to Al (111), Ni (111)/Al (200) and Ni(222) reflections, respectively, as marked in Fig. 4.10(a). The XRD profiles show that the Ni peaks at $2\theta \sim 44.3^\circ$ (111) and $\sim 98.2^\circ$ (222) appear even up to the highest temperature of annealing, 300°C. On the contrary the Al (111) peak at 38.8° starts disappearing after the first annealing at 150° C. The modification in XRD pattern for annealed sample S1, in temperature range 150°C to 300°C, suggests the presence of possible intermetallic phases Al_3Ni_2 (110), Al_3Ni_2 (123), Al_3Ni (503) from peaks at 2θ values $\sim 44.65^\circ$, 97.32° , 97.6° and have been marked as green squares (■) in Fig. 4.10(a).

The width of the XRD peaks for Al and Ni and the intermetallics for S1 are much broader compared to bulk, since the samples have layer thickness in typically tens of nanometer and the interface alloy crystallites are also in the range few nanometers.

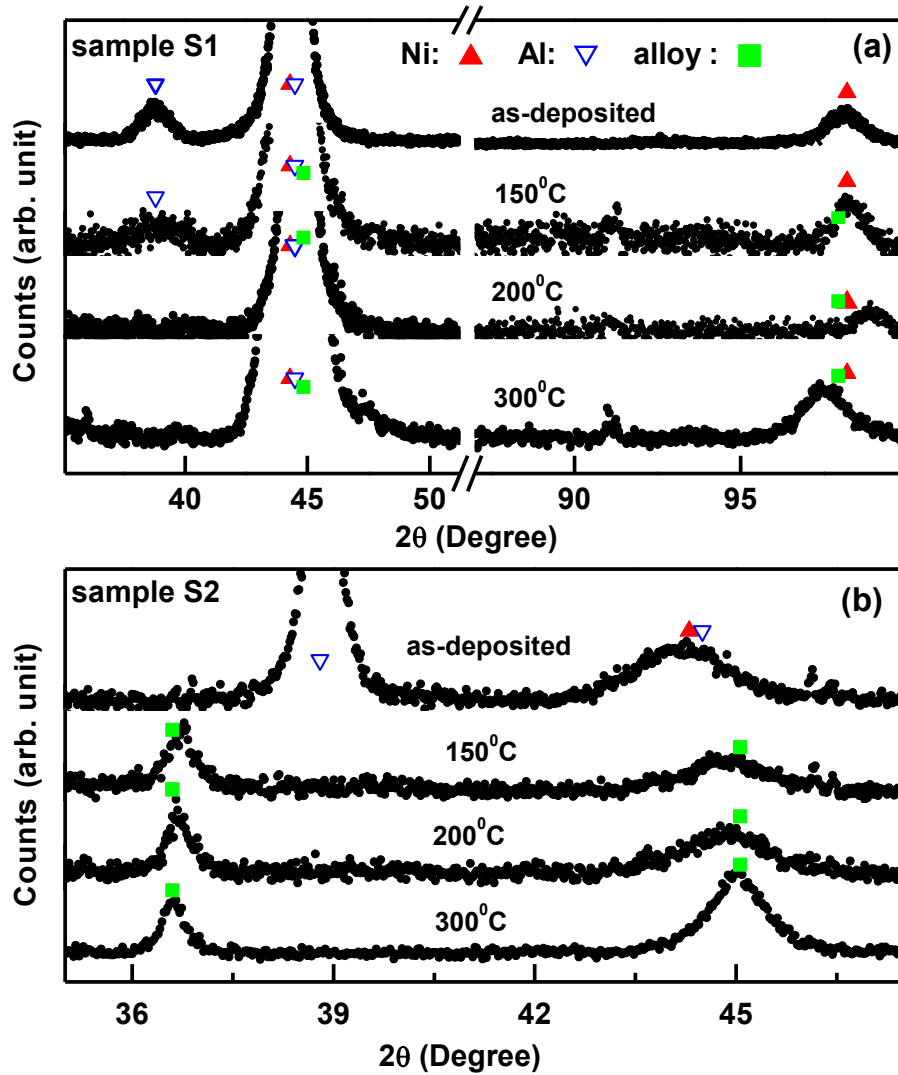


Figure 4.10: X-ray diffraction (XRD) pattern for as-deposited and annealed (150°C, 200°C, 300°C) states for samples S1(a) and S2(b), respectively. Open triangles, solid triangles and solid squares mark the possible Bragg peaks for alloy phases.

In case of as-deposited sample S2 (Al-rich) we observed a strong Bragg peak at $2\theta \sim 38.8^\circ$, [Fig. 4.10 (b)] which corresponds to Al(111) reflection and indicates that the film is textured in (111) direction. One can also see a broad peak at 44.2° , which corresponds

to Al (200) as well as to Ni (111). In this Al-rich multilayer, all the Bragg peaks corresponding to pure Al and Ni disappear after the first anneal at 150 °C. Two new peaks emerge after annealing one occurs at lower angle of scattering, $2\theta \sim 36.7^\circ$, corresponding to Al_3Ni (220) or Al_4Ni_3 (332). The second one is a broad Bragg peak appearing at higher angle ($\sim 44.85^\circ$) which can be identified with Al_3Ni_2 (110), Al_3Ni (022) or Al_4Ni_3 (440). These peaks are shown as green squares (■) in Fig. 4.10(b). The disappearance of the Ni and Al peaks in S2 after the first anneal clearly indicates faster kinetics of alloy formation in this multilayer. This is attributed to higher concentration of Al, the more mobile species, in this multilayer.

After further annealing of sample S2 at 200 °C and 300°C the Bragg peak at $2\theta \sim 44.85^\circ$ becomes sharper, indicating growth of alloy grains. XRD data clearly indicates that the growth kinetics of the alloy phases are strongly dependent on the stoichiometry. While we are able to conclude that the alloy phases are crystalline, from XRD data, the exact composition of the alloy phases was identified from XRR and PNR and found to be Al_3Ni in both the samples [10].

Growth of the alloy grain (Al_3Ni) was estimated in the samples S1 and S2 from the width of the XRD Bragg peaks that have gradually become narrower on annealing. We have considered the peaks at $2\theta \sim 98.2$ in S1 and at $2\theta \sim 44.8$ in S2 for estimating the grain size. We attempted to fit both Ni and Al_3Ni phases for the samples S1 and S2 at various stages of annealing. The fitted Bragg peaks at different temperatures of annealing are shown in Fig. 4.11: left panel for S1 and right panel for S2. Crystallite size (L) was calculated from Debye-Scherrer formula [108] using width of the corresponding peaks. In case of sample S1, we could get sizable fraction of Ni even after the final anneal but in case of S2 the fraction of Ni became nearly zero even after the first anneal at 150 °C.

This is also supported by XRR and PNR data [10]. In case of S1, alloy grain size increased from $\sim 50\text{\AA}$ to 170\AA and in S2 the grain size increased from $\sim 60\text{\AA}$ to 88\AA on annealing.

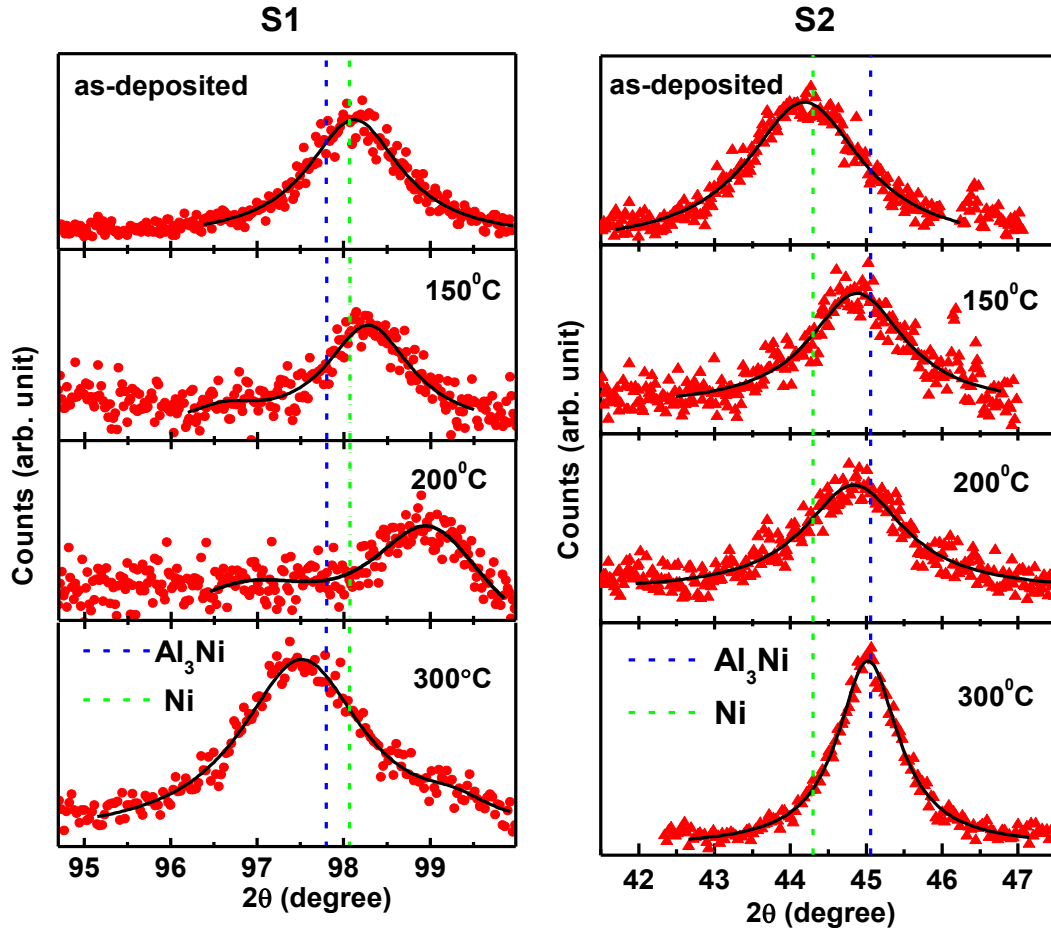


Figure 4. 11: Variation of alloy peak as a function of annealing temperatures (150°C, 200°C, 300°C) for samples, S1 (left panel) and S2 (right panel) respectively.

Morphological changes for the as-deposited and annealed samples (at 300° C) were studied by AFM. Inset of Fig. 4.12 shows the AFM images from samples S1 and S2. To study the effect of annealing on morphology of the surface we measured the height difference correlation function ($g(r)=\langle [h(r) - h(0)]^2 \rangle$), where the angular brackets, $\langle \rangle$, denote ensemble average [91]. We used height data from AFM and fitted the height difference function for the self-affine fractals [90,91]:

$$g(r) = 2\sigma^2 \left(1 - \exp\left(-\left(r/\xi\right)^{2H}\right) \right) \dots\dots(4.1)$$

Where ‘ ξ ’ is the correlation length and is a measure of the lateral length scale of roughness, ‘ σ ’ is uncorrelated roughness and ‘ H ’ is the Hurst parameter which defines the fractal dimensionality (d) of the surface as: $d = 3-H$. Fig. 4.12 shows the height difference correlation function (open circles) with corresponding fit (solid lines) for as deposited and annealed samples at 300°C for S1 and S2.

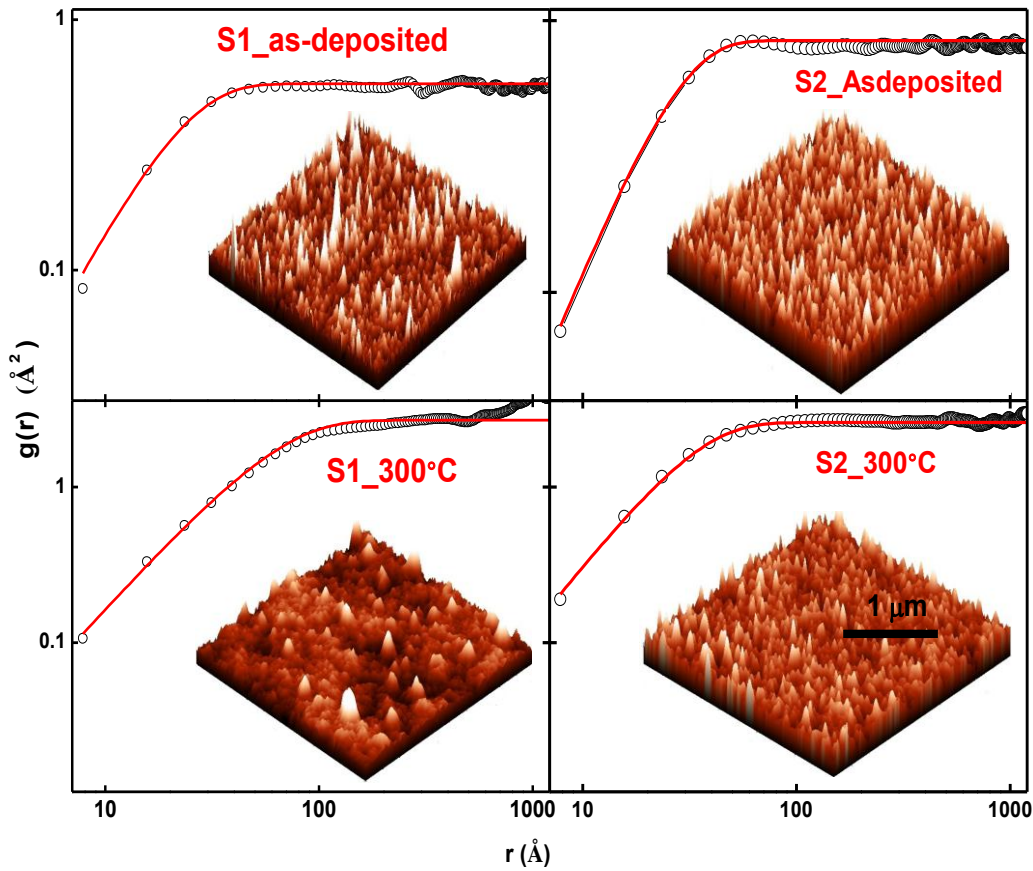


Figure.4.12: Height difference correlation function ($g(r)$, open circles) with the fit (solid lines) from samples, S1 and S2 for as deposited and annealed state obtained from AFM. Inset shows corresponding 3-dimensional AFM images of size $2 \mu\text{m} \times 2 \mu\text{m}$.

We obtained a correlation length (surface roughness) of 215Å (5Å) and 620Å (11Å), for as-deposited and annealed sample S1 at 300°C, respectively, from AFM data. An increase in surface roughness implies that morphology has become more granular

after annealing at 300°C as evident from the AFM image. For S2 we obtained the correlation lengths (surface roughness) as 270Å (6Å) and 330Å (11Å) respectively for the as-deposited and annealed state. We also obtained similar Hurst parameter (H) of ~ 0.8 for both samples S1 and S2 in the as-deposited and annealed state, suggesting nearly two-dimensional surface growth. The increase in correlation length of both samples on annealing corroborates the increase in grain size of crystallites as measured by XRD.

From XRR and PNR we obtained Ni:Al for alloy layers about 1:3 (NiAl_3) for both the systems (S1 and S2). PNR data were also used to investigate the evolution of magnetization as a function of annealing temperature for these samples. The spin ASYM function is defined as the ratio between the difference and sum of spin dependent reflectivity [$\text{ASYM} = (R^+ - R^-)/(R^+ + R^-)$], where R^+ and R^- are neutron reflectivities for neutron with polarization parallel and anti-parallel respectively to the sample magnetization [109,110]. Variation of the ASYM function (closed circles, red) as a function of annealing temperature along with the fits (solid lines) is given in Fig. 4.13 for S1 (left panel: (a)-(d)) and for S2 (right panel: (e)-(h)), respectively.

Oscillations observed in the ASYM profiles are due to the layer thickness while the amplitude of the oscillations arises because of the contrast between the spin-up and spin-down reflectivities [109,110]. The large amplitude of oscillations in the ASYM parameter in the upper panels of Fig. 4.13 [(a) and (e)] are due to magnetic moment in the as-deposited Ni layer. Flattening of the ASYM parameter with annealing corroborates the formation of non-magnetic alloy layer. It is observed that even after the final anneal (at 300 °C) the ASYM parameter for S1 shows clear oscillations with Q , indicating presence of magnetism in the remaining Ni layer. In case of S2, R^+ and R^- profiles almost merged

after the first anneal giving rise to a flat behaviour in asymmetry parameter indicating complete alloying and loss of magnetization in this sample.

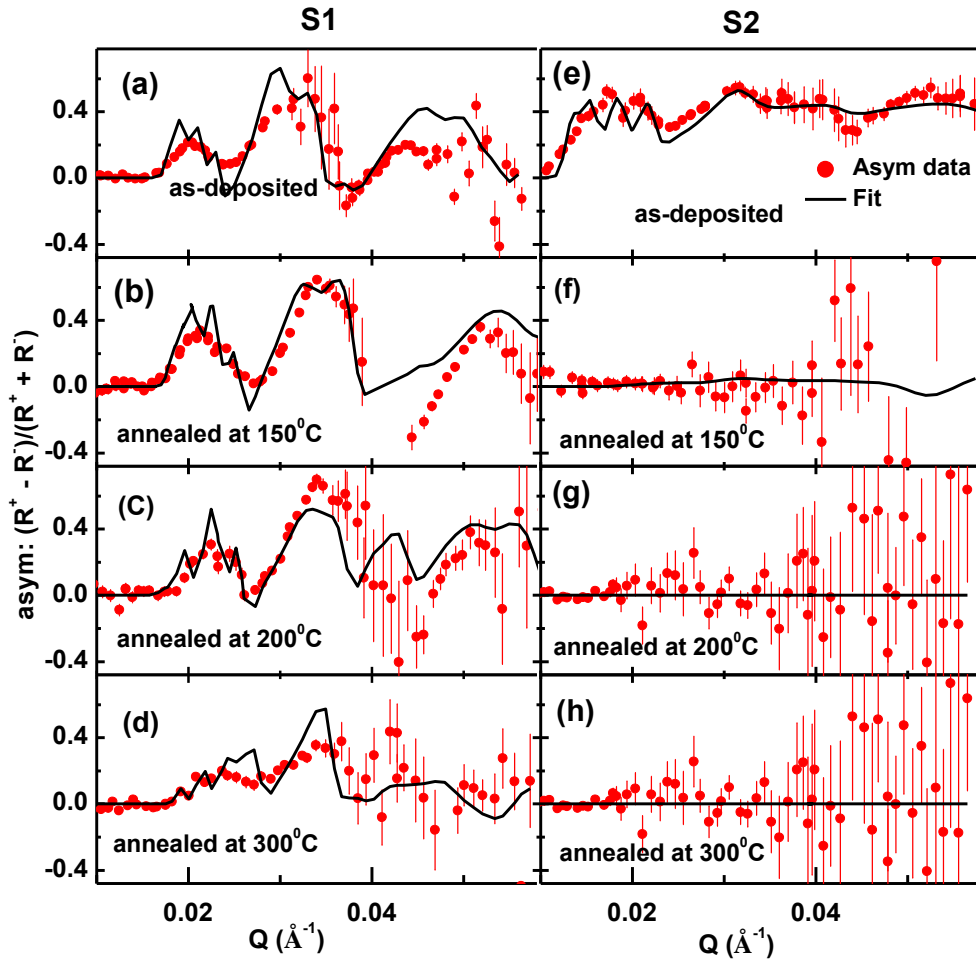


Figure 4.13: Spin ASYM $[(R^+ - R^-)/(R^+ + R^-)]$ function (closed circles) with fit (solid lines) at different temperature of annealing for S1 [(a)-(d)] and S2 [(e)-(h)].

The intensity of Bragg reflection in PNR measurements as a function of annealing temperature can be used to estimate diffusion constants [9,96,97]. With the growth of interface alloy due to mixing caused by annealing, the Bragg peak due to the periodicity of the multilayers become less intense because of loss in contrast. After each anneal, the reflectivity pattern of a sample gives a snap-shot of the kinetics of alloying. One can use the following relation between intensity ratio of the Bragg peaks before and after annealing with the diffusion constant at the temperature of annealing and the duration of

annealing (t) to estimate the diffusion constant [9,96,97]:

$$\ln[I(t) / I(0)] = -\frac{8\pi^2 n^2 D t}{d_{bl}^2} \dots\dots(4.2)$$

Where $I(t)$ and $I(0)$ are the intensities of the n^{th} order Bragg peak after annealing for time ' t ' and in the as-deposited sample respectively, ' d_{bl} ' is the bilayer thickness and ' D ' is the diffusion constant.

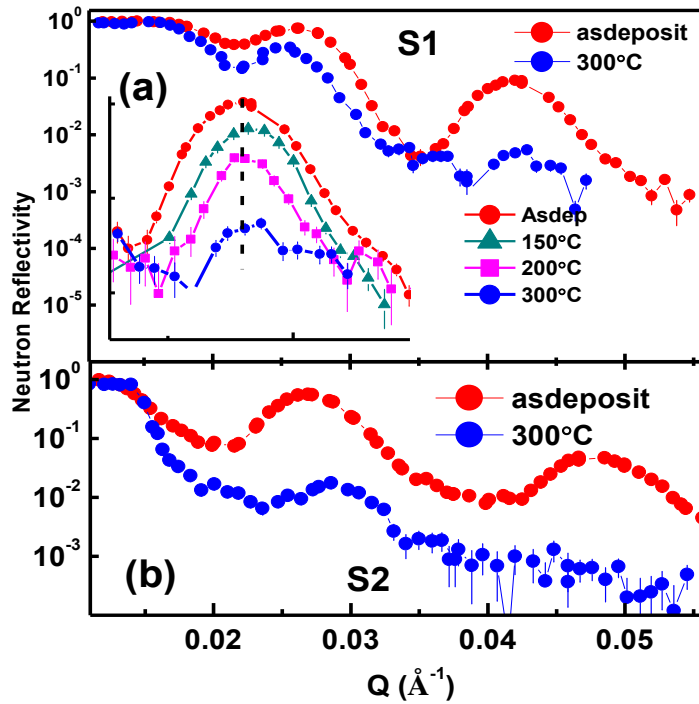


Figure 4.14: Measured reflectivity profiles for spin up (R^+) neutrons for as deposited and annealed state at 300°C for samples S1 (a) and S2 (b) respectively. Inset of (a) shows Bragg Peak intensity variation as a function of different annealing temperature for S1.

Fig. 4.14 (a) and (b) show the measured reflectivity profiles of the spin up (R^+) neutrons for as-deposited and annealed samples at 300°C for S1 and S2, respectively. The inset in Fig. 4.14(a) shows the variation of Bragg peak intensity as a function of annealing temperatures for S1, to highlight the loss of intensity after each anneal. Thus we can estimate the diffusion constant using Bragg intensity of PNR data at different annealing temperatures. Further in diffusion controlled kinetics we can write the diffusion constant

as a function of temperature: $D = D_0 \exp(-E_a/KT)$ [23], where ‘ E_a ’ is the activation energy required for diffusion and ‘ T ’ is the annealing temperature. Using the Arrhenius plot ($\ln(D)$ vs. $1000/T$) as shown in Fig. 4.15, we obtained the activation energies (E_a) for these systems [S1 and S2] from the slopes of the plots.

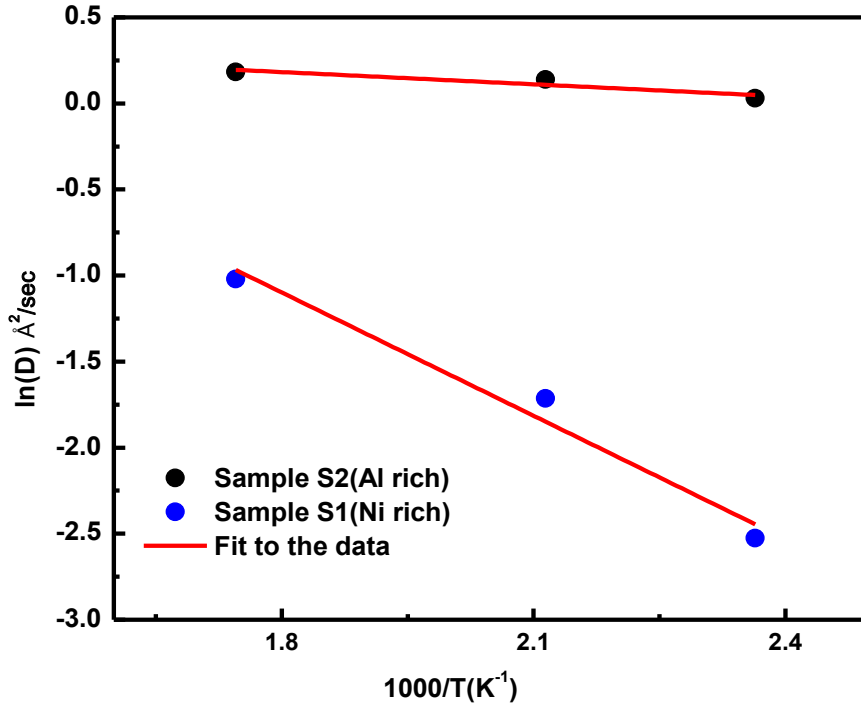


Figure 4.15: Arrhenius plot for growth of alloy phase in sample S1 and S2.

Interestingly, the activation energy is widely different in these two samples. We found E_a values as ~ 205 meV and ~ 20 meV for S1 and S2, respectively. In case of the Ni-rich stoichiometry (S1), the activation energy is nearly 10 times higher than the activation energy obtained for the Al-rich sample (S2). This is clearly due to the difference in mobility between Al and Ni at the temperatures of annealing, which suggests that higher energy is required for diffusion in the Ni rich environment than in Al rich environment. This result also allows us to compare the stability of the two systems against thermal treatment.

The key findings from the measurements XRD, XRR and PNR are plotted in Fig. 4.16.

We have shown the variation in crystallite size (from XRD), thickness of alloy layer at interfaces (from XRR and PNR) and average magnetic moment of Ni atom (from PNR) as a function of annealing temperature in Fig. 4.16 (a), (b) and (c), respectively.

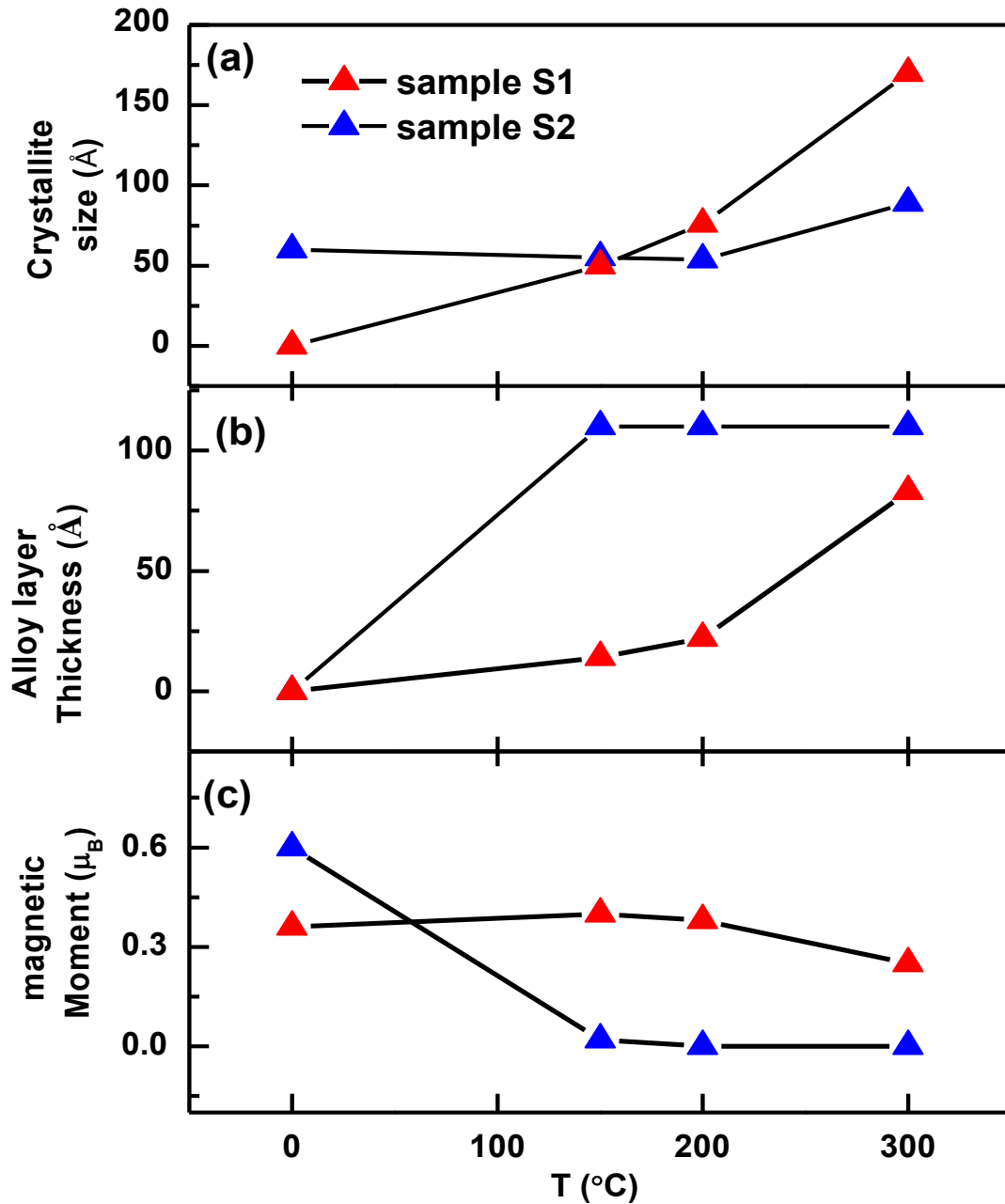


Figure 4.16: Variation of (a) crystallite size (b) alloy layer thickness (c) average magnetic moment of Ni atom in individual layers as a function of annealing temperature for S1 and S2. Lines drawn are just a guide to visualization.

Clear increase in crystallite sizes of alloy phase on annealing in the range of 150°C-300°C was accompanied by increase in the thickness of the alloy layer [Fig.4.16 (a), Fig 4.16(b)]. We obtained maximum alloy layer thickness of $\sim 80 \text{ \AA}$ at the interface on annealing sample S1 at 300°C. However, on annealing sample S2 at 150°C, a rapid alloying resulted in growth of alloy layer thickness of $\sim 110 \text{ \AA}$ at interface. On further annealing at higher temperature no significant increase in alloy layer thickness was observed, showing saturation after rapid alloying at 150 °C. This growth is accompanied by rapid drop in average magnetic moment unlike in sample S1, which shows nearly uniform magnetic moment over the entire range of annealing temperature [Fig. 4.16(c)]. Slow variation in magnetization (Fig. 4.16(c)) of Ni on annealing of sample S1 also suggest slow growth of alloy (nonmagnetic) layer at interfaces which doesn't destroy the magnetization of Ni significantly.

4.5.2 Summary

In the present work, we have studied two ultra-thin multilayers of Ni and Al, consisting of periodic bilayer, with overall stoichiometry of Ni_3Al and NiAl_3 . The impact of stoichiometric difference on structural parameters like crystallite size, alloy layer thickness and magnetization on annealing has been discussed in detail. We observed that Al rich sample is prone to rapid changes in structural and magnetic properties upon annealing, in the temperature range of 150 °C to 300°C. Whereas the Ni rich sample is more stable when subjected to annealing confirming its thermal stability. We observed that the systems have widely different values of activation energy, which is responsible for different degrees of diffusion in both the systems. We obtained the activation energy for S1 and S2 as 205 meV and 20 meV respectively from the Arrhenius plot ($\log D \sim 1/T$).

Chapter 4: Nickel Aluminides

Morphological study of the samples by AFM showed that the surface morphology is two dimensional after annealing for both S1 and S2. The Al rich sample (S2) has a more uniform morphology as compared to the Ni rich sample (S1) as observed from AFM.

Chapter 5: Nickel Germanides (Micro-structural characterization of low resistive metallic Nickel-Germanide growth on annealing of Ni/Ge multilayer)

- 5.1 Introduction
- 5.2 Sample preparation and experimental details
- 5.3 Results and discussion
- 5.4 Summary

5.1 Introduction

The areas of thin magnetic films and magnetic hetero-structures have witnessed remarkable development in recent years [111]. Current interest in the magnetism and transport behavior of ultrathin films and multilayers is driven by their manifold applications in the field of microelectronics, as interconnects in spintronics and as magnetic sensors in information storage devices [36,112]. Among these magnetic hetero-structures, ferromagnetic metal-semiconductor (FM/SC) systems are an important class, because of their wide range of applications in microelectronics [32-34]. Due to charge / spin transport across the interfaces these combinations (FM/SC) display attractive properties which have motivated many experimental and theoretical studies in the field of magnetism and nanotechnology [12,113,114]. Structure and magnetic properties of a FM/SC system, strongly depend on the structure and morphology of the interfaces [115-118].

Germanium is an important material for metal oxide semiconductor field effect transistor (MOSFET) applications because of its high intrinsic mobility (two times higher for electrons and four times higher for holes as compared to those in Si [34,119]). Similarly, Ni has the advantage of forming germanides for Ge MOSFET applications over other transition metals [34]. In correspondence with the current Si-based technology, where metal

silicides are used as contacts for the source, drain, and gate of the transistors, metal germanides appear as natural candidates for making Ge contacts [32]. Hence, developing optimal contact materials is of supreme importance. In current design and processing of transistors, the contact material should exhibit low contact resistances, good stability under heat treatment, and should be formed at a low temperature to avoid thermal degradation of the gate material.

Nickel germanides are suitable candidates for inter-connects in the field of microelectronics as they form low resistive phases (mono-germanide: NiGe) on annealing at relatively low temperature (~270°C) as compared to other transition metal germanides [32,35] and such low processing temperature is effective to prevent thermal degradation of the gate material [34]. These advantages make nickel germanide contacts more suitable for Ge device fabrication and especially mono germanide is of substantial research interest [120].

Thermal annealing is one of the suitable methods for inducing solid state reactions between Ni and Ge with short bilayer periods to produce nickel germanides [34,121]. Formation of NiGe upon annealing mainly depends on the thickness ratio of individual Ni and Ge layers in the as-deposited state with the required atomic number ratio of Ni to Ge [7,14]. Considering the number density (no. of atoms per unit volume) of Ni as $9.1 \times 10^{22} \text{ cm}^{-3}$ and of Ge as $4.41 \times 10^{22} \text{ cm}^{-3}$, in bulk, to get an alloy with 1:1 atomic ratio in a multilayer stack we should have a thickness ratio $d(\text{Ge})/d(\text{Ni})$ of 2.1:1 [7,14]. Based on this estimate, we deposited a Ni-Ge multilayer with designed thickness of Ni as 100Å and of Ge as 200Å with four bilayers. The multilayer was annealed at 250°C in vacuum for different time intervals: 0.5h, 1.5h and 4h and then characterized by several experimental techniques.

We have studied the physical and magnetic depth profiles in the multilayer film and their correlation with charge transport property in the Ni/Ge multilayer as a function of

time of annealing at a temperature of 250°C. The resistance of the multilayer film was measured by four probe method over a temperature range of 10 K-300 K after each anneal. There was a large drop in resistance of the multilayer by a factor of about two after the final anneal. We found that this drop was a consequence of formation of a low resistive phase at the interfaces of Ni/Ge on annealing [32]. Grazing angle x-ray diffraction (GIXRD) measurements have been used to map the evolution of new alloy phases. Formation of an interface alloy has been correlated with the morphological properties of the surface of the sample using Atomic force microscopy (AFM) measurements. Depth dependent structural and magnetisation profiles have been obtained using X-ray reflectivity (XRR) and polarized neutron reflectivity (PNR) techniques[11,15,22] The XRR and PNR results showed that low resistive alloy phase that grew at the interfaces on annealing the system is NiGe. Information regarding bulk magnetization of the sample has also been obtained from Superconducting Quantum Interference Device (SQUID) magnetometry.

5.2 Sample preparation and experimental details

The Ni/Ge multilayers was grown by DC/RF sputtering technique at SSPD, BARC, INDIA [18]. The base vacuum prior to deposition was $\sim 5 \times 10^{-7}$ Torr in the deposition chamber. The working vacuum with flowing Ar gas was $\sim 4 \times 10^{-3}$ Torr during deposition. The Ni layers were deposited with 1.5 kW DC power supply whereas the Ge layers were deposited with a frequency of 13.56 MHz RF power supply (300W). The films were deposited on boron doped p-type Si (111) substrate. Designed structure of the multilayer samples can be represented as: Si (substrate) / [Ni_{100Å} / Ge_{200Å}] \times 4. After deposition, the sample was annealed at 250°C under vacuum ($\sim 10^{-3}$ Torr) for time intervals of 0.5h, 1.5h and 4h.

Resistance measurements of the as-deposited and annealed stages were carried out by four probe method [122]. Bulk magnetization measurements of the sample was carried

out by MPMS5-SQUID magnetometer on samples of dimension 5×6 mm. Crystallographic structure determination and phase identification were carried out using X-ray diffraction with Cu K α ($\lambda = 1.54 \text{ \AA}$) laboratory source in a θ -2 θ geometry. Quantitative information about the structural parameters (thickness, roughness, scattering length density) of the systems were obtained from reflectometry analysis (XRR, PNR) that uses a scattering length density (SLD) model based on χ^2 minimization method [22,11,15,69]. This method uses genetic algorithm based on Parrat's formalism [15]. The PNR data were collected at the reflectometer beam line with incident wavelength (λ) of 2.5 \AA at DHRUVA reactor, BARC, INDIA [66]. X-ray can reveal the electron SLD in a scattering experiment and neutrons can reveal the nuclear SLD. But both the electron scattering length density (ESLD) and nuclear scattering length density (NSLD) values originates from same number density in the sample. Using ESLD and NSLD values together we obtained the interface alloy stoichiometry for Ni-Ge systems [11,14]. Depth dependant magnetic SLD profile for the sample was also obtained by PNR. The interface alloy layer formed due to annealing is magnetically dead from PNR analysis as we could not see any ferromagnetic behavior.

Morphology of the film was examined by AFM in order to monitor the changes in surface morphology during annealing [91]. The quality of the surface is important for making electrical contacts on a film's surface as required in devices. The AFM data were collected on a sample of 2×2 μm^2 size at a 'Solver P47H' microscope. NSG10_DLC super sharp DLC tip grown on Silicon with curvature 1-3 nanometer has been utilized in semi-contact mode. In AFM operation cantilever's resonant frequency & force constants were 213 kHz and 10 N/m respectively.

5.3 Results and discussion

Resistance profiles of the Ni/Ge multilayer as a function of temperature in the range 10 K-300 K , for the as-deposited and for samples annealed at 250°C for 0.5h, 1.5h , 4h

respectively are shown in Fig.5.1. All the measurements were carried out on samples of same geometrical dimension ($\sim 5 \times 5 \text{ mm}^2$).

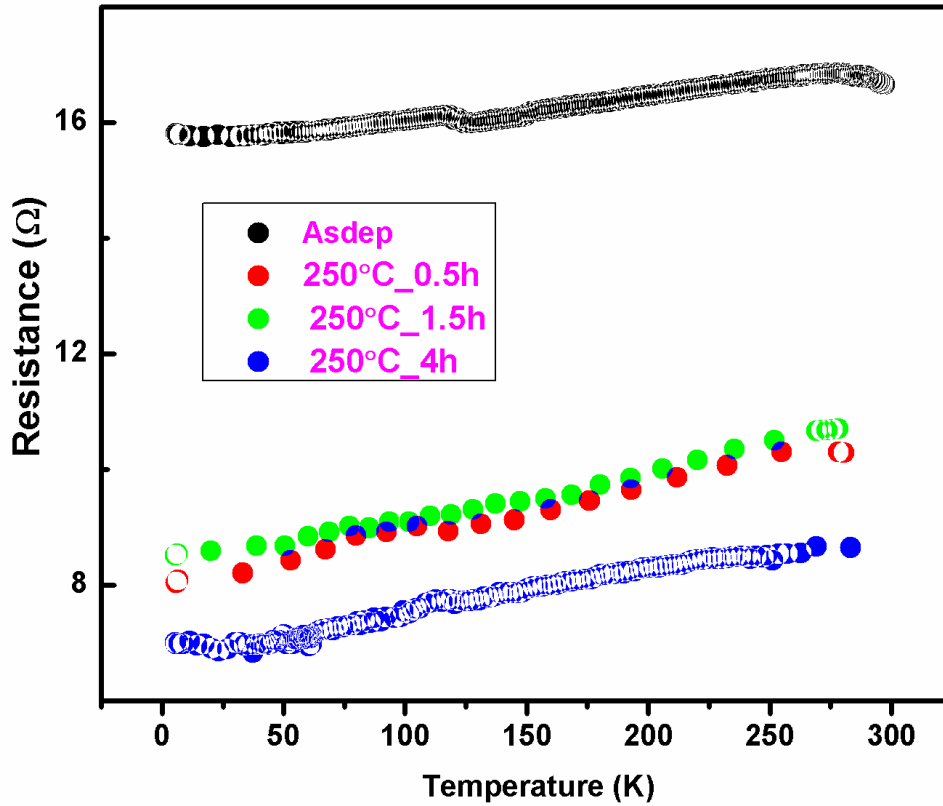


Figure 5.1: Resistance measurement of the Ni-Ge multilayer at different stages of annealing by Fourprobe method. All the measurements were carried out on samples of same geometry.

Measured resistance profiles show a metallic trend over the above temperature range. Resistances of annealed samples were observed to be lower than the resistance of as-deposited sample over the entire temperature range. The resistance profiles show nearly flat behavior for the temperature range of measurement. Hence one can compare the average resistance of the samples as a function of annealing temperature. We obtained an average value of $R \sim 17 \Omega$ for the as-deposited Ni-Ge multilayer sample. However there is a significant drop to $\sim 10 \Omega$ in the average resistance after annealing for 0.5h at 250 °C. The resistance remains almost same on further annealing the sample for 1.5 h. But after

annealing up to 4h the average resistance profile further dropped to 8Ω . This fall in resistance on annealing is due to formation of a low resistive phase in the sample i.e., NiGe [32,123] as shown in the following analysis. Grazing angle XRD profiles of the as-deposited and the sample annealed at 250°C for 4h are shown in Fig. 5.2. Position of possible XRD Bragg peaks are marked as vertical line on x-axis in the panel below.

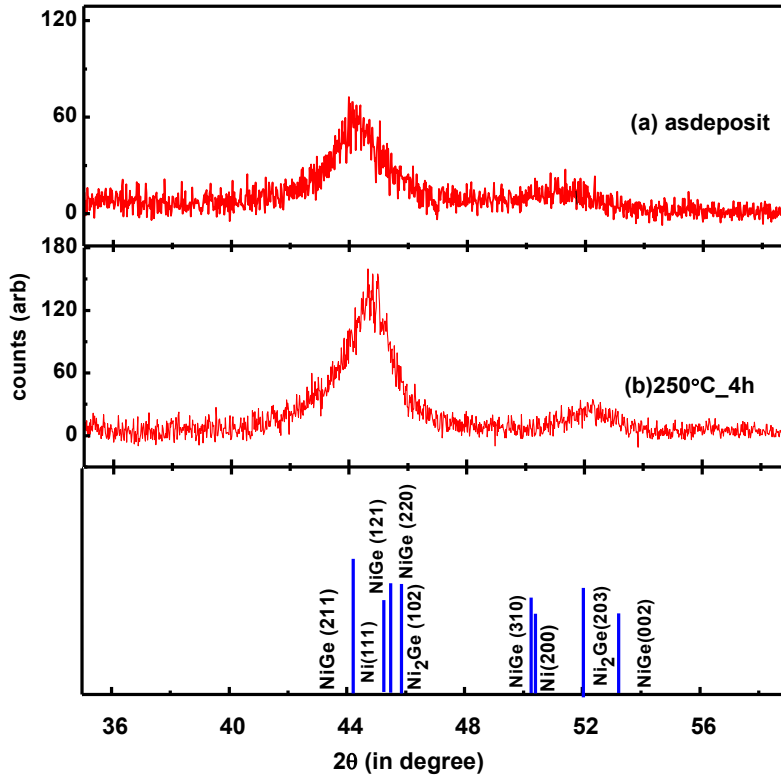


Figure 5.2: X-Ray diffraction of the sample for the (a) as deposit and (b) annealed stage at 250°C for 4h, Panel below shows the possible XRD Bragg peaks.

For the as-deposited state, there are Bragg reflections from Ni(111) and Ni (200) at 2θ values $\sim 44.3^\circ$ and 51.6° respectively. There are no peaks due to Ge, indicating that it is possibly in amorphous phase. There are new narrower peaks at higher angles due to alloy phase evolution in the system. Narrowing of peaks is perhaps due to growth in crystallite size. We have indicated the possible alloy peaks of Ni and Ge (NiGe, Ni₂Ge), in the panel below (Fig. 5.2). It is evident from the XRD profile that, it is not promising to uniquely

identify the alloy phase. However, the exact alloy phase composition formed at the interfaces has been determined from two reflectometry data, both XRR and PNR. This will be discussed later. Ge was found to be amorphous in both the as-deposited and annealed state of this sample.

To quantify the effect of annealing on morphology of the film surface we carried out AFM measurements on the samples. We evaluated the height difference correlation function (HDCF) defined as [91],

$$g(r) = \langle [h(r) - h(0)]^2 \rangle = 2\sigma^2 \left(1 - \exp\left(-\left(\frac{r}{\xi}\right)^{2H}\right) \right) \dots\dots\dots (5.1)$$

Using the height data from AFM and above expression, we tried to fit 'g(r)' for the self-affine fractals.

Where 'ξ' is the correlation length and is a measure of the lateral correlation length on the sample surface, 'σ' is the uncorrelated roughness and 'H' is the Hurst parameter which defines the fractal dimensionality (d) of the surface as: $d = 3 - H$. Fig 5.3 shows the height difference correlation function (solid circles) with corresponding fits (solid lines) for as-deposited and samples annealed at 250°C for 4h. Inset shows three dimensional (3d) AFM images for as deposited and annealed states.

We obtained estimates of correlation length 'ξ': 620 Å and 640 Å, uncorrelated surface roughness 'σ': 13 Å (13Å) and 15Å, for as-deposited and annealed sample respectively, from AFM data. These values imply that morphology of the sample did not change significantly after annealing, indicating that there is no morphological degradation of the sample due to the relatively low-temperature annealing. We also obtained similar Hurst parameter ('H') of ~0.8 for both as deposited and annealed state, suggesting nearly two-dimensional surface morphology for both as-deposited and annealed samples [91].

Detailed structural and magnetic characterization of the system at nanometer resolution was carried out using both XRR and PNR techniques. The data are shown in Fig. 5.4. Fig. 5.4(a) shows PNR profiles from the as-deposited and sample annealed at 250°C for 0.5h, 1.5h, 4h along with their fits (solid lines). The R plus (R^+) and R minus (R^-) profiles (red and black circles) are reflectivity due to polarized neutrons with their spins parallel (+) and anti-parallel (-) respectively with respect to sample magnetization direction. Reflectivity in y-axis (Fig. 5.4(a)) was offset for different stages of annealing, for better visualization.

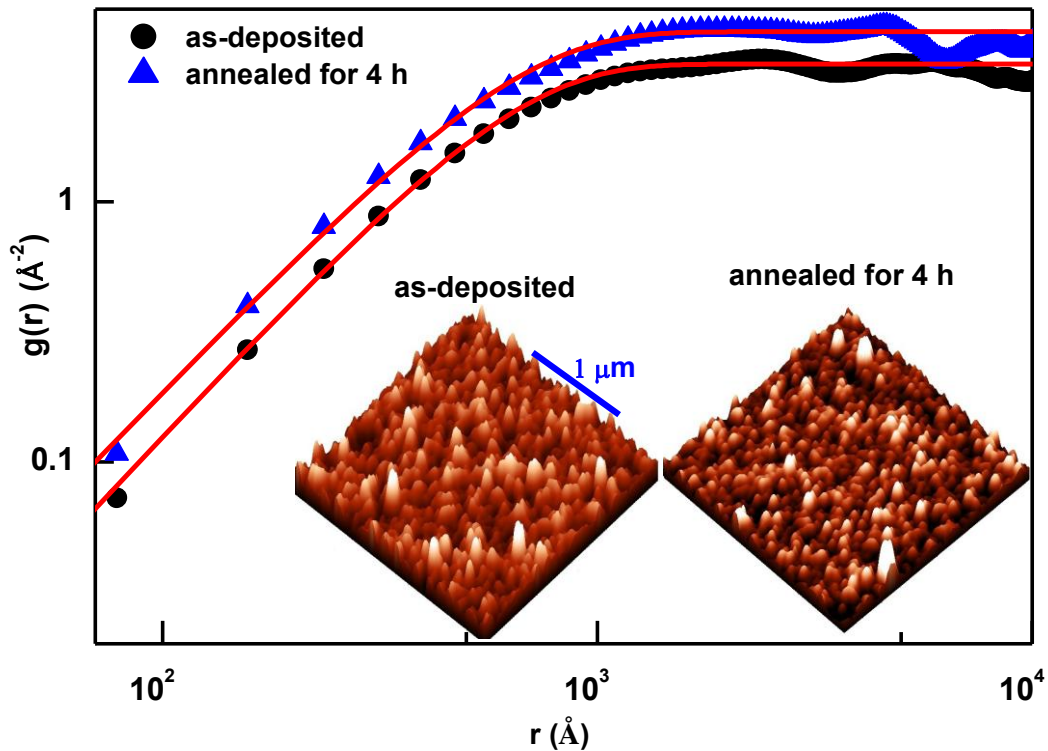


Figure 5.3: Height-height correlation function for the as deposited and sample annealed for 4h (Inset shows respective 3d-AFM image of the film surface ($2 \times 2 \mu\text{m}^2$)).

It is observed from the PNR profiles (Fig.5.4 (a)) that, after annealing at 0.5h the Bragg peaks become well defined as compared to the as deposited state. This is possibly due to elimination of microscopic voids or impurities during initial annealing that were present in

the film in the as-deposited state [104,105]. We observed a shift of the 2nd order Bragg peaks towards higher Q value for the annealed states. This implies reduction in bilayer thickness due to elimination of the defects in the sample, causing compaction of the bilayer.

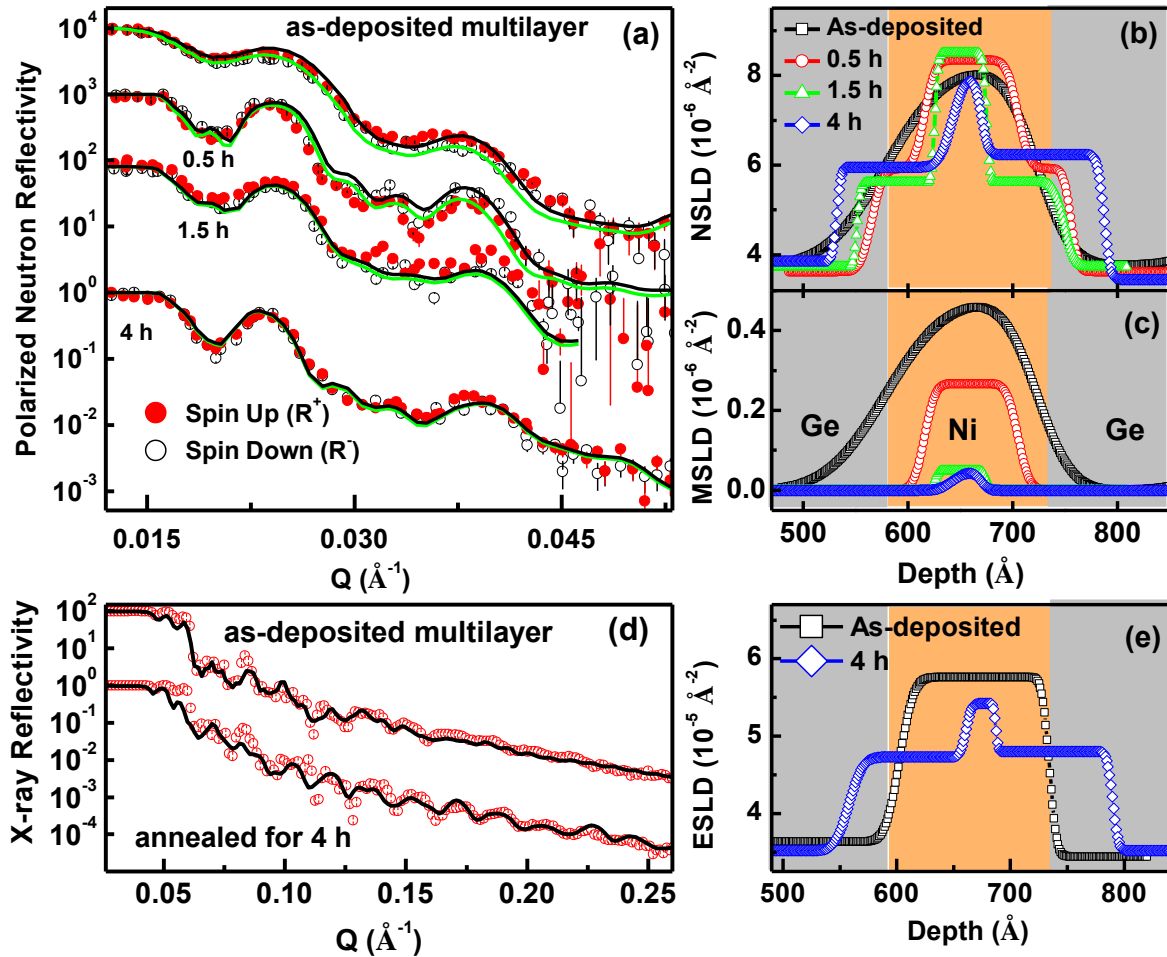


Figure 5.4: (a) PNR measurements from the as-deposited and annealed samples along with fits (solid lines) (b) Nuclear scattering length density (NSLD) and (c) magnetic scattering length density (MSLD) depth profile of a single Ni-Ge bilayer, that fits the PNR data shown in 2(a). (d) XRR profiles for as-deposited and annealed sample along with fits and (e) corresponding electron scattering length density (ESLD) profile of a single Ni-Ge bilayer.

Thickness of the Ni and Ge layer were obtained as 145Å and 216Å respectively in the as-deposited state from PNR analysis. However after annealing of 4h at 250°C, a respective thickness of Ni and Ge reduced to 26Å and 111Å. An alloy layer of 113Å developed at

the interfaces at the expense of reduced thickness of Ni and Ge after annealing. We obtained nuclear (NSLD) profiles and magnetization profiles (MSLD) from the PNR data for all the annealed states. Fig 5.4(b) and 5.4 (c) shows the fitted nuclear and magnetic SLD profiles respectively for a single Ni/Ge bilayer for as deposited and annealed stages as obtained from PNR analysis.

NSLD profile of a Ni-Ge bilayer at various stages of annealing are shown in Fig.5.4 (b). The NSLD profile after annealing for 0.5h at 250°C (marked as red circles) in Fig. 5.4 (b) with respect to the as-deposited sample (marked as black squares) shows that there is reduction in interface roughness after the first anneal and marginal increase in density. NSLD of Ni and Ge were found to be $8.03 \times 10^{-6} \text{ \AA}^{-2}$ (85% of bulk.) and $3.6 \times 10^{-6} \text{ \AA}^{-2}$ (~bulk density) after first anneal. On further annealing at 1.5h and 4h width of the alloy layer increased due to higher degree of alloying at the interfaces.

The interface alloy layer was found to have a nuclear SLD value of $5.8 \times 10^{-6} \text{ \AA}^{-2}$ after annealing of 4h at 250 °C. Fig. 5.4 (c) shows the MSLD of Ni for the as deposited and for each annealed stage at 250°C. For the as-deposited state we obtained the MSLD of Ni as $\sim 0.3 \times 10^{-6} \text{ \AA}^{-2}$ (30% of the bulk) from the PNR analysis. With increase in annealing time, as the alloy layer grew in thickness, the magnetic SLD reduced gradually as shown in Fig. 5.4 (c). After final anneal of 4 h MSLD of the remaining Ni layer reduces significantly. This loss in magnetization is due to diffusion of Ge in Ni layers. But the well defined Bragg peaks as observed from PNR profiles indicates the system retains its layered structure even after annealing up to 4h, albeit the appearance of Ni/Ge alloy layers at the interfaces. This indicates thermal stability of the samples after the annealing at 250 °C. The interface alloy layers were found to be non magnetic from PNR analysis.

One can obtain exact alloy composition at the interfaces from dual analysis of PNR and XRR data for a two component system [11,14]. XRR profiles for as-

deposited and annealed state (4h) along with their fits are given in Fig. 5.4(d). Corresponding electron SLD (ESLD) profiles are shown in Fig. 5.4.(e). In case of XRR the data was recorded over a much larger ‘Q’ range compared to PNR and we ensured that we obtained a reasonable fit over the entire ‘Q’ range for both PNR and XRR with the same physical model. The ESLD in XRR and the NSLD in PNR both originate from the same physical density profile in the sample. Hence using these SLD values in equation (discussed in detail in section 3.5 of chapter 3), we can calculate the interface alloy composition in binary systems [11,14]. Here we found the interface alloy stoichiometry to be NiGe (mono germanide) from the reflectometry analysis.

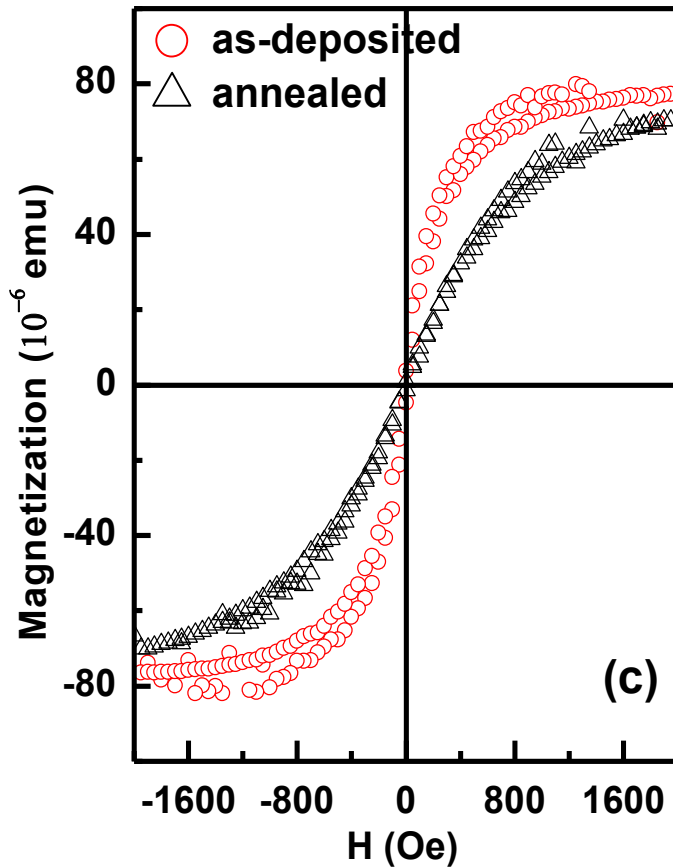


Figure 5.5: SQUID measurement profiles for the as deposited and sample annealed at 250 °C for 4h.

Bulk magnetization data for the sample was also obtained from SQUID measurements. The SQUID data shown in Fig. 5.5 are for samples of different size and have not been normalized to sample volume. This data confirms ferromagnetic behavior of the multilayer in as-deposited and in annealed state and also gives an estimate for saturation magnetic field. In general, we observed reduction in saturation magnetization of the multilayer on annealing, which is in-line with PNR measurements and consistent with the growth of non-magnetic Ni germanides at interfaces as seen by reflectivity techniques discussed later. However samples were saturated well below a magnetic field of 2 kOe (applied during PNR measurements for saturating the sample) in both the cases. There is a reduction in saturation magnetization of the sample from 78 emu/cc to 68 emu/cc on annealing for 4h at 250°C in line with the PNR data.

Key findings of the systems presently studied as obtained from XRR, PNR and resistivity measurements as a function of annealing time is plotted in Fig.5.6 (a) and (b). We have shown the variation in thickness of Ni, Ge and the interface alloy (NiGe) layer due to annealing in Fig.5.6(a). Clear decrease in individual layer thickness of Ni and Ge due to increase in annealing time is observed. We noticed a larger reduction in thickness of Ni (67%) as compared to Ge (48%) due to alloying. Change in resistance of the sample as a function of annealing time at room temperature is shown in Fig 5.6 (b). Resistance of the sample drops significantly after annealing of 0.5h as seen in Fig.5. 6 (b). From Fig. 5.6 (a) and 5.6 (b) it is evident that the drop in resistance of the sample is directly proportional to the increase in thickness of the interface alloy layer. The drop in resistance of the sample on annealing can be explained on the basis of formation of a low resistivity metallic NiGe phase on annealing [32]. Accurate estimation of the layer thicknesses of the components in the Ni-Ge multilayer allows us to make an estimate of

the resistivity of the NiGe alloy layer using a parallel network model as shown in Fig. 5.6 (c) . Fig 5.6 (c) depicts the schematic of alloy formation at interfaces of a single bilayer of Ni-Ge (left panel) on annealing.

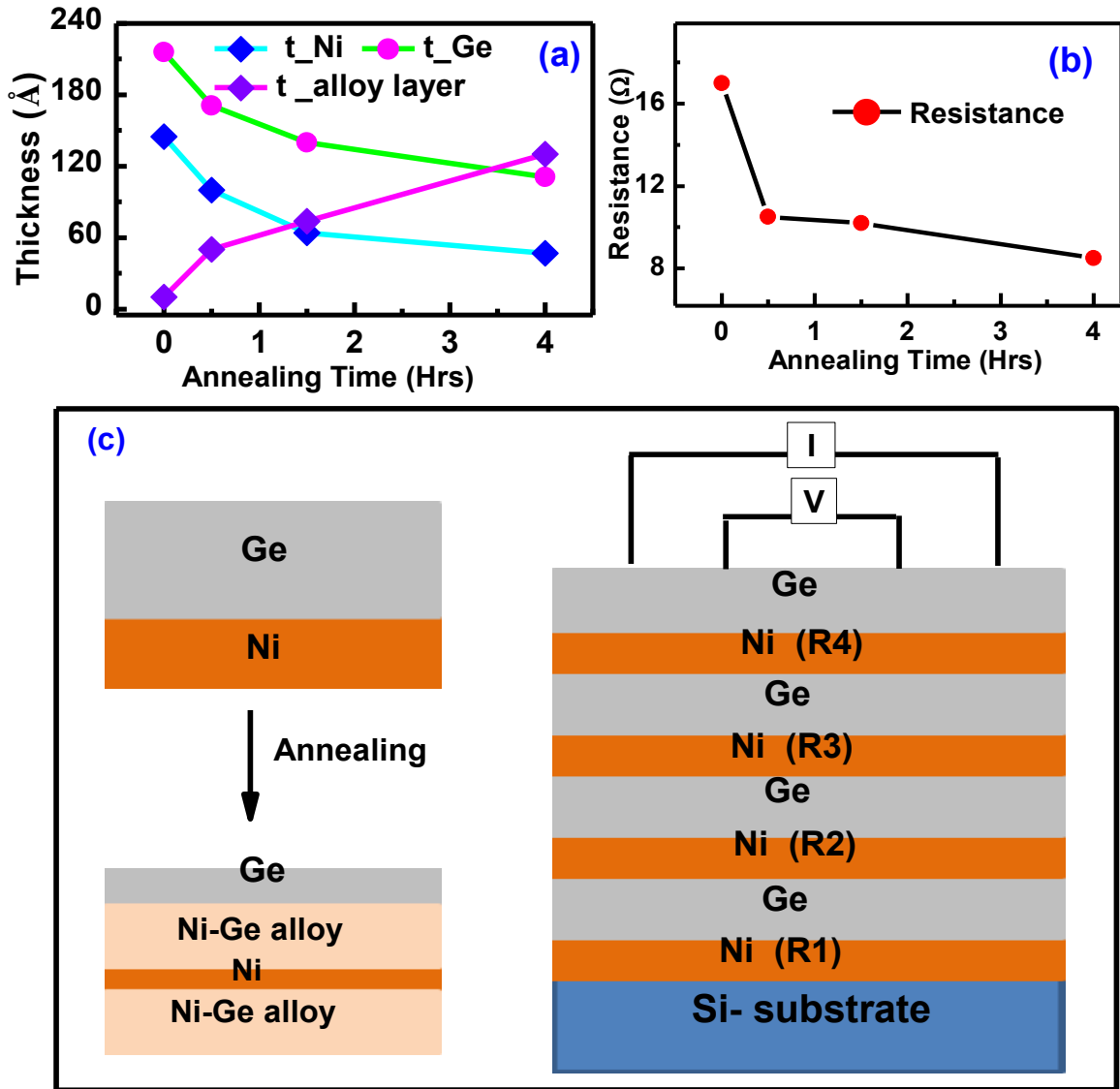


Figure 5.6: Variation in (a) layer thicknesses of Ni,Ge and the alloy layer and (b) resistance of the Ni-Ge multilayer sample at 300 K as a function of annealing time. (c) left panel show the schematic of interface before and after annealing the Ni/Ge multilayer sample. Right panel show the schematic of a parallel combination of resistors with Ni and Ge in alternating positions and considering only the Ni layers as resistors in the as deposited state,

To estimate the resistivity of the interface alloy layer we have considered a simple parallel network model. We have considered the Ni-Ge system as a parallel combination of resistors considering each Ni and Ge layer as individual resistors (four Ni and four Ge resistors for the as-deposited state as shown in Fig.5.6 (c), right panel). Ni has a much smaller value of resistivity ($\rho_{Ni} \sim 10 \mu\Omega\text{cm}$) as compared to Ge ($\rho_{Ge} \sim 10^7 \mu\Omega\text{cm}$) at room temperature [124]. For estimating net resistivity of the system, we have considered the resistance values of each layer of the parallel network model and finally obtained the resistivity from the geometry of the samples. For this calculation, contribution of Ge layers can be neglected as $1/\rho_{Ni} \gg 1/\rho_{Ge}$. Hence Ge layers were assumed to be open paths for the flow of current between the contacts in the as-deposited case as shown in Fig. 5.6 (c). If 'R' is the net resistance of the system and R_{Ni} is the resistance of the individual Ni layers, then for the as deposited state we estimate: $1/R \approx 4/R_{Ni}$, which gives the value of $R_{Ni} \sim 64 \Omega$. After annealing, thickness of the Ni layers reduced and alloy layers of NiGe developed at the interfaces providing extra transport path. The enlarged view for the post annealing stage for a single bilayer is shown in Fig.5.6 (c) (left panel) for better visualization. We have scaled the resistances of Ni layers after annealing (R'_{Ni}) by a factor t_0/t to account for the increase in resistance due to reduction in thickness of the layer, where t_0 and t are the thicknesses of Ni layer before and after annealing respectively. The net resistance (R) of the system now after annealing can be written as:

$$\frac{1}{R} \approx \frac{4}{R'_{Ni}} + \frac{7}{R_{NiGe}} \dots\dots\dots(5.2)$$

Since there are now seven conducting NiGe layers at the interfaces. Using the above relation, resistance of an alloy NiGe layer, R_{NiGe} is estimated to be $\sim 53 \Omega$. This gives an

estimated resistivity of NiGe alloy layer as $\sim 59 \mu\Omega.cm$. This value clearly indicates metallic nature of the interface alloy layer.

5.4 Summary

A series of studies have been performed on a Ni/Ge multilayer to obtain information about microstructural evolution in the system due to annealing at 250 °C for different time intervals. Structural and magnetic properties of the system has been obtained by XRD, XRR and PNR. Other characterizations of the system involve resistivity study by four probe method, bulk magnetization study by SQUID and surface morphology by AFM. We obtained a low resistive, non magnetic alloy at the interfaces of the Ni-Ge multilayer. We estimated resistivity of the alloy layer to be $\sim 59 \mu\Omega.cm$ which is metallic by nature. From AFM study it was observed that the sample does not undergo morphological degradation due to annealing which signifies thermal stability of the sample. The low formation temperature, low resistivity, sufficient morphological stability of NiGe makes it a potentially suitable candidate as a contact material in electronics.

Chapter 6: Summary and Future Directions

6.1 Summary

The research work presented in this thesis primarily involves structural and magnetic study of thin films/multilayer using x-ray reflectometry (XRR) and polarized neutron reflectometry (PNR) data on annealing. Deposition of thin films, bilayers and multilayers also has been carried out using DC/RF magnetron sputtering unit developed in-house, as a part of this thesis. Reduced dimension of thin films often lead to quite different properties from their bulk counterpart and hence of interest for basic queries as well as technical applications. Both these aims can be fulfilled only after understanding detailed structure of a thin film and how this affects physical properties of the films. There are many experimental tools for characterizing thin films at various length scales. Some of these are destructive and some are non-destructive. The later ones are desirable to study the structure of a film without destroying it. Neutron and x-ray reflectometry are two non-destructive techniques, which can characterize thin films with sub-nanometer resolution. Especially PNR is a unique tool that gives magnetic properties with sub-nanometer resolution apart from the physical structure of the film. The present work used these two techniques extensively along with other routine characterization tools viz. X-ray Diffraction (XRD), Atomic Force Microscopy (AFM), Secondary Ion Mass Spectrometry (SIMS), Superconducting Quantum Interference Device (SQUID) for the work presented in the thesis. The thesis has specifically targeted interface alloy layers that form between two different layers of materials with different characteristics and quantified the interface alloy physical parameters in terms of its composition, thickness, roughness etc.. Special

attempt has been made to characterize the structure and magnetic properties at the interfaces in the thin film multilayers studied. We have deposited and characterized multilayer samples of two components, in this thesis. This is due to the fact that for multilayer samples one observes Bragg peaks in reflectivity pattern and if there is mixing or alloying at the interfaces, the Bragg peak intensity deteriorates. Using this loss in intensity one can study diffusion-controlled kinetics at the interfaces. Interface alloys have been formed by controlled annealing in multilayers of metal/metal and metal/semiconductor components. For the metal/metal category Ni-Al multilayers of various thickness combinations were prepared for the study. For the metal-semiconductor category Ni-Ge multilayer was chosen. It has been shown earlier in ref [14,10] that using XRR and PNR together one can determine exact composition of alloy layers at interfaces in two component multilayers. The kinetics of alloy formation, determination of exact alloy stoichiometry, estimation of diffusion constant and growth of first alloy phase at the interfaces have been studied at microscopic length scales using reflectometry techniques in the present thesis. Detailed characterization of the samples were done at every stage of annealing using reflectometry and other characterization tools.

Ni aluminides, have been recognized as suitable candidates for variety of high-temperature structural applications to operate well beyond the operating temperatures of conventional materials due to their excellent oxidation and corrosion resistant properties. Nickel aluminides of desirable physical and mechanical properties can be prepared by controlled solid state reaction with specific thickness combination of Ni and Al layers. A Ni-Al multilayer system of ten bilayers with designed structure of Si/[Al(25Å)/Ni(50Å)] \times 10 was annealed at 160°C for 1h, 4h and 8h. To understand the effect of interface morphology on alloy formation, the as deposited and successive annealed stages have been analyzed by reflectometry

techniques (XRR and PNR). We observed asymmetry in alloy formation at different interfaces, Ni on Al (Ni/Al) and Al on Ni (Al/Ni) due to different surface energies of Ni and Al. It also has been noticed that different surface energy of constituting elements leads to different surface roughness, that leads to different local density at the reacting interfaces. This gives rise to different effective heat of formation which ultimately results asymmetric alloy formation at the interfaces.

To understand the effect of stoichiometry on alloy formation kinetics we have studied another set of Ni-Al multilayer, Si/[Ni(200Å)/Al(100Å)] \times 5 (S1) and Si/[Ni(50Å)/Al(227Å)] \times 5 (S2) with exactly opposite stoichiometry 3:1 and 1:3 in Ni and Al respectively. Structural characterization of the samples has been done using XRR, PNR, XRD and SIMS. XRR and PNR measurements were used to identify the exact composition of alloy at the interfaces after annealing the samples. We calculated the diffusion length from PNR Bragg peaks and observed that the thickness of the interface alloy phase matched well with this length scale for both the samples. Also an attempt has been made to estimate the diffusion lengths for Ni and Al separately, from Darken's combined diffusion expression. We observed that even over short length scales, kinetics of the components takes precedence over thermodynamics at low temperature annealing and the first phase formed was NiAl₃ for both the samples in this study.

Stoichiometry dependent inter diffusion and structural evolution in these multilayer was also done in a separate study. We reported the evolution of crystallite size, alloy layer thickness at the interfaces and magnetic moment of Ni atoms in individual layers as a function of annealing temperature, using XRD, XRR and PNR measurements. Surface morphology of the samples before and after annealing were obtained by AFM technique. The observed changes in crystallite sizes obtained from

XRD analysis are proportional to the corresponding changes in height-height correlation length as measured from AFM. Using PNR we also measured the changes in the magnetic properties of samples on annealing which clearly suggest formation of a nonmagnetic alloy layers at the interfaces. Diffusion constants, obtained from PNR measurements at different temperatures of annealing, have been used to measure the activation energy for diffusion of the systems. We observed, diffusion constant of the Al-Ni multilayer systems, depends strongly on the overall stoichiometry in the films, leading to widely different activation energies for alloy formation in the two multilayers as studied in this work.

Nickel Germanides are one of the important classes among the transition metal Germanides. Ni germanides have properties that are important in the field of magnetism and semiconductor technology. The Ni/Ge systems [Si (substrate) / [Ni_{100Å} / Ge_{200Å}] \times 4] were prepared by DC/RF magnetron sputtering on a deposition unit built in-house. In the present thesis low-resistance Ni-Germanide phase has been formed at the interfaces of a Ni/Ge multilayer film by controlled annealing and has been characterized for its composition, transport and magnetic properties. Here we report successful formation of NiGe metallic alloy phase at the interfaces of a Ni-Ge multilayer on controlled annealing at relatively low temperature ~ 250 ° C. Using XRR and PNR , we found that the alloy phase stoichiometry is equi-atomic NiGe, a desirable low-resistance inter-connect. We found significant drop in resistance ($\sim 50\%$) on annealing the Ni-Ge multilayer suggesting metallic nature of alloy phase at the interfaces. Further we estimated the resistivity of the alloy phase to be $\sim 59\mu\Omega$ cm, which indicates its metallic nature. This study highlights not only formation of a specific alloy phase but use of its structural parameters, obtained from reflectometry, in quantifying its resistivity at nanometer length scale.

6.2 Future Directions

During the present work the author has gained experience in preparation of various thin films, mostly bilayers and multilayers of two materials and used different techniques to characterize them, neutron and x-ray reflectometry being the major tools. The reflectometry experiments were limited to specular mode for all the samples. The samples studied were magnetic and non-magnetic metals or magnetic metal and semiconductor pairs prepared as multilayers. The work specifically targeted studying the growth of interface layers and their characterization at microscopic level.

The author plans to expand the domain of research in two directions. One will be to use reflectometry technique in other modes to carry out the characterization in greater details and the other will be to use the techniques learnt at present for other types of samples of interest. In the present work polarized neutron reflectometry has been used without any spin-analysis to obtain magnetic moment depth-profiles in the samples studied. If one carries out polarization analysis of the reflected beam, it can give details of magnetic structure in the thin film sample. The author plans to carry out such studies in future. Also one can get the morphology of buried interfaces using off-specular neutron reflectometry. Such morphology has been obtained in some samples for the film-air interface using AFM in the present thesis. Off-specular neutron reflectometry for the morphology of buried interfaces is planned for future.

The studies carried out during the present thesis work has demonstrated the strength of the reflectometry techniques in probing thin films with nanometer resolution. The present thesis deals with pure elemental layers of metals and semiconductors. Currently large number of experimental work is being done in oxide materials, especially perovskites and multiferroics. Researchers are attempting to

Chapter 6: Summary and Future Directions

bring two or ordered states in the same material and study the dependence of one order on the other. Thin films are ideally suited for such an attempt. One can combine two such oxide layers in close proximity at microscopic length scale and study the role of such proximity on the macroscopic ferromagnetic, ferroelectric or ferroelastic states. Such samples will also require characterization at nanometer length scale for which PNR and XRR will be the ideal probes. Moreover one can choose various substrates for such samples which will provide excellent epitaxy to tune the layering of the films. The author is looking forward to carry out such studies in future.

All the samples used in the present thesis were inorganic in nature. Neutrons provide excellent contrast between hydrogen and deuterium in terms of scattering lengths. This fact has made neutron reflectometry an important tool worldwide for studying polymer films and their interface dynamics. This author plans to explore this window also in future.

In general, the author proposes to expand the scope of studies on thin films by using the probes in other modes, learn other techniques for thin film growth & characterization and explore new thin film samples for future studies.

References

- [1] https://www.tu-chemnitz.de/physik/PHFK/LEHRE/Script%204_2010.pdf
- [2] M. Wittmer, *J. Vac. Sci. Technol. A* **2**, 273-280 (1984).
- [3] S. C. Deevi and V. K. Sikka, *Intermetallics* **4**, 357 (1996).
- [4] M. N. Baibich, J. M. Broto, A. Fert, F. Nguyen Van Dau, F. Petro, P. Eitenne, G. Creuzet, A. Friederich, and J. Chazelas, *Phys. Rev. Lett.* **61**, 2472 (1988).
- [5] A. G. Evans and J. W. Hutchinson, *Acta metall. mater.* **43**, 2507-2530 (1995).
- [6] V. K. Sikka, J. T. Mavity and K. Anderson, *Material Science and Engineering* **A153**, 712-721 (1992).
- [7] U. Rothhaar, H. Oechsner, M. Scheib, and R. Müller, *Phys. Rev. B* **61**, 974-979 (2000).
- [8] R. Pretorius, R. De Reus, A.M. Vredenberg and F.W. Saris, *Mater. Lett.* **9**, 494-499 (1990).
- [9] H. Schmidt , M. Gupta , T. Gutberlet , J. Stahn , M. Bruns, *Acta Mater.* **56**, 464-470 (2008).
- [10] M. Swain, S. Singh, S. Basu, D. Bhattacharya and M. Gupta, *J. App. Phys.* **116**, 222208 (2014).
- [11] Surendra Singh, Saibal Basu, M. Gupta, C. F. Majkrzak, and P. A. Kienzle, *Phys. Rev. B* **81**, 235413 (2010).
- [12] S. Datta and B. Das, *Appl. Phys. Lett.* **56**, 665 (1990).
- [13] I. Žutić, J. Fabian, and S. Das Sarma, *Rev. Mod. Phys.* **76**, 323 (2004).
- [14] Mitali Swain, Surendra Singh, Saibal Basu, Mukul Gupta, *J. Alloy. Compd.* **576**, 257 (2013).
- [15] L.G. Parratt, *Phys. Rev.* **95**, 359-369 (1954).
- [16] C. F. Majkrzak, *Physica B* **173**,75-88 (1991).

- [17] Milton Ohring, *The Materials Science of Thin Films*, Academic Press, United Kingdom Edition (1992).
- [18] Debarati Bhattacharya, A. Biswas, K.G. Bhushan, M. Swain and S. Basu, AIP Conf. Proc. **1349**, 487-488 (2011).
- [19] Joy Joy George, *Preparation of Thin Films*, Marcel Dekker. INC. New York, (1992).
- [20] G. E. Bacon, *Neutron Diffraction* , Oxford Clarendon Press (1975).
- [21] Krassimir Stoev And Kenji Sakurai, The Rigaku Journal **14**,22-37, (1997).
- [22] M. R. Fitzsimmons and C.F. Majkrzak, *Modern Techniques for Characterizing Magnetic Materials*, Springer: New York, (Chap. 3, pp. 107–155R.) (2005).
- [23] E. G. Colgan, Mater. Sci. Rep.**5**,1(1990).
- [24] F. Scheppe , P.R. Sahm, W. Hermann, U. Paul, J. Preuhs, Materials Science and Engineering **A329–331**, 596–601(2002).
- [25] G. K. DEY, Sadhana **28**, 247 (2003).
- [26] S. Kalpakjian, *Manufacturing Engineering and Technology* (4th Edn.), Prentice Hall, (2001).
- [27] D.K. Singh, *Fundamental of Manufacturing Engineering* (1st Edn.), Ane Books India, (2008).
- [28] A. I. Taub and R. L. Fleischer, Science **243**, 616 (1989).
- [29] M. Yamaguchi, H. Inui and K. Ito, Acta mater. **48**, 307-322 (2000).
- [30] P. Nash, M.F. Singleton and J.L. Murray, *Phase Diagrams of Binary Nickel Alloys*, 4th edn (Metals Park, OH: ASM International,(1991).
- [31] E. G. Colgan, M. Nastasi, and J. W. Mayer, J. Appl. Phys. **58**, 4125 (1985).

- [32] Jae-Wook Lee, Jee-Hwan Bae, Ji-Hye Hwang, Hyung-Kyu Kim, Min-Ho Park, Hyounsub Kim, Cheol-Woong Yang, *Microelectronic Engineering* **89**, 23-26 (2012).
- [33] Q. Zhang, N. Wu, T. Osipowicz, L. K. Bera and C. Zhu, *Japanese J. App. Phys.* **44**, L1389–L 1391 (2005).
- [34] S. Gaudet, C. Detavernier, A. J. Kellock, P. Desjardins, and C. Lavoie, *J. Vac. Sci. Technol. A* **24**, 474 (2006).
- [35] S. P. Ashburn, M. C. Ozturk, J. J. Wortman, G. Harris, J. Honeycutt and D. M. Maher: *J. Electron. Mater* **21**, 81(1992).
- [36] S. Zhu, R. Li, S. J. Lee, M. F. Li, A. Du, J. Singh, C. Zhu, A. Chin and D. L. Kwong: *IEEE Electron Device Lett.* 26 81(2005).
- [37] A Fick, *Phil. Mag.* **10**, 30 (1855).
- [38] Helmut Mehrer, *Diffusion in Solids* (Springer Publishing).
- [39] D.A. Glocker, S.I. Shah (Eds.), *Handbook of Thin Film Process Technology*, IOP Publishing, Bristol, (1995).
- [40] R.F. Bunshah (Ed.), *Handbook of Deposition Technologies for Films & Coatings*, Noyes Publications, New Jersey, (1994).
- [41] L. M. Falicov, *Physics Today*, **46**, Oct., (1992).
- [42] P.J. Kelly, R.D. Arnell, *Vacuum* **56**, 159-172(2000).
- [43] P.D. Davidse and L. M. Maissel, *Transactions of 3rd international Vacuum Congress, Stuttgart., 1965; J Appl. Phys.* **37**,574 (1966).
- [44] John A. Thornton, *J. Vac. Sci. Technol. A* **4** (6), 3059 (1986).
- [45] Y. Kudriavtsev, A. Villegas, A. Godines, R. Asomoza, *App. Surf. Sci.* **239**, 273–278, (2005).

- [46] Krishna Seshan, *Handbook of thin-film deposition processes and Techniques Principles, Methods, Equipment and Applications, 2nd Edn*, New Noyes Publications, William Andrew Publishing, U.S.A. (2002).
- [47] Mitali Swain, Debarati Bhattacharya, and Saibal Basu, AIP Conf. Proc. **1591**, 946-947 (2014).
- [48] M. Swain, D. Bhattacharya, K.G Bhushan, and S. Basu, AIP Conf Proc. **1451**, 182-184 (2012).
- [49] Debarati Bhattacharya, T.V.Chandrasekhar Rao, K.G.Bhushan, M.Swain and S. Basu, AIP Conf Proc. **1451**, 319-321 (2012).
- [50] R. Rosenberg, D.C.Edelstein, C.-K.Hu, K.P. Rodbell, Annu. Rev. Mater. Sci. **30**, 229 (2000).
- [51] Mitali Swain , Surendra Singh, Debarati Bhattacharya, Ajay Singh, R.B. Tokas, C.L Prajapat and Saibal Basu, AIP Advances
- [52] Attwood D., *Soft X-Rays and Extreme Ultraviolet Radiation*, Cambridge University Press (1999).
- [53] B.P. Toperverg, Physica B **297**,160-168 (2001).
- [54] L. Cheng, Z. Altounian, D. H. Ryan, J. O. Ström-Olsen, and M. Sutton and Z. Tun, Phys. Rev. B **69**, 1444031 (2004).
- [55] M. Sato and K. Abe, Solid State Commun. **26**, 95 (1978).
- [56] J. Lekner, *Theory of Reflection of Electromagnetic and Particle Waves*, (Martinus Nijhoff Publishers), (1987).
- [57] M. Born and E. Wolf, *Principles of Optics: Electromagnetic Theory of Propagation, Interference and Diffraction of Light* ,Oxford, Perg. Press ,(1965).
- [58] H. Zabel, *Festkörperprobleme* **30**, 197 (1990).

- [59] M. Tolan, *X-Ray Scattering from Soft-Matter Thin Films*, Springer Tracts in Modern Physics **148**, Springer Heidelberg, (1999).
- [60] L. Névot and P. Croce, *Rev. Phys. Appl.*, **15**, 761(1980).
- [61] C. F. Majkrzak, *Physica B* **173**,75-88 (1991).
- [62] G. P. Felcher, R. T. Kampwirth, K. E. Gray and Roberto Felici, *Phys. Rev. Lett.* **52**, 1539, (1984).
- [63] P. Yeh, *Optical Waves in Layered Media*, Wiley, New York, (1988).
- [64] S. W. Lovesey, *Theory of neutron scattering from condensed matter*, Vol. **2**, Clarendon Press, Oxford,(1984).
- [65] F. Mezei, *Z. Phys.* **255**, 146 (1972).
- [66] S Basu and S Singh, *J. Neut. Res.* **14**, 109 (2006).
- [67] D.E. Goldberg, *Genetic Algorithm in Search, Optimization and Machine Learning*, Addison-Wesley, Reading, MA, (1989).
- [68] S. Singh and S. Basu, *Solid State Phy. (India)* **44**, 257 (2001).
- [69] W. H. Press, S. A. Teukolsky, W. T. Vetterling, and B. P. Flannery *Numerical Recipes in Fortran: The Art of Scientific Computation*, 2nd ed. Cambridge: Cambridge University Press, (1992).
- [70] M. Wormington, C. Panccione, K. M. Matney and D. K. Bowen, *Phil. Trans. R. Soc. Lond. A*, **357**, 2827 (1999).
- [71] T.V. Chandrasekhar Rao and M. K. Sanyal, *Appl. Surf. Sci.* **74**, 315 (1994).
- [72] P. C. Clapp and M. J. Rubins and S. Charpenay and J. A. Rifkin and Z. Z. Yu and A. F. Voter, *MRS Online Proceedings Library*, Volume 133, 1988, 29
doi:10.1557/PROC-133-29, Published online by Cambridge University Press 26 Feb 2011.

- [73] R. Darolia and D. F. Lahrman and R. D. Field and A. J. Freeman, MRS Online Proceedings Library, Volume 133, 1988, 113, doi: 10.1557/PROC-133-113, Published online by Cambridge University Press 26 Feb 2011.
- [74] Diana Farkas, MRS Online Proceedings Library, Volume 133, 1988, 137 doi: 10.1557/PROC-133-137, Published online by Cambridge University Press 26 Feb 2011.
- [75] S. P. Chen and A. F. Voter and A. M. Boring and R. C. Albers and P. J. Hay MRS Online Proceedings Library, Volume 133, 1988, 149, doi: 10.1557/PROC-133-149, Published online by Cambridge University Press 26 Feb 2011
- [76] D. N. Sioff and S. S. Brenner and Hua Ming-Jian MRS Online Proceedings Library, Volume 133, 1988, 155, doi: 10.1557/PROC-133-155, Published online by Cambridge University Press 26 Feb 2011.
- [77] K.Ganesh Kumar, Sivarao, T. Joseph Sahaya Anand, International Journal of Engineering & Technology IJET-IJENS **11**, 274-282 (2011).
- [78] V.K. Sikka, S.C. Deevi, S. Viswanathan, R.W. Swindeman , M.L. Santella, Intermetallics **8**, 1329-1337 (2000).
- [79] N. S. Stoloff, C. T. Liu , S. C. Deevi, Intermetallics **8**, 1313-1320 (2000).
- [80] H. Sieber, J.S. Park, J. Weissmüller, J.H. Perepezko, Acta Mater. **49**, 1139-1151 (2001).
- [81] L. Battezzati , P. Pappalepore, F. Durbiano and I. Gallino, Acta Mater. **47**, 1901-1914. (1999).
- [82] C.C. Koch and J. D. Whittenberger, Intermetallics **4** ,339-355 (1996).
- [83] B. S. Murty and S. Ranganathan, Int. Mater. Rev. **43**,10-140 (1998).
- [84] Naresh N. Thadhani, Prog. Mater. Sci. **37**, 117-226 (1993).

- [85] J. Noro, A.S. Ramos, M.T. Vieira, *Intermetallics* **16**, 106-1065 (2008).
- [86] E. Ma ,C. V. Thompson, and L. A. Clevenger, *J. Appl. Phys.* **69**, 2211 (1991).
- [87] R. W. Bené, *Appl. Phys. Lett.* **41**, 529 (1982).
- [88] A. S. Edelstein, R. K. Everett, G. Y. Richardson, S. B. Qadri, E. I. Altman et al.
J. Appl. Phys. **76**, 7850-7859 (1994).
- [89] Mitali Swain, Surendra Singh , Saibal Basu , Debarati Bhattacharya, R.B. Tokas, Mukul Gupta, *J. Alloy. Compd.* **631**, 46-51 (2015).
- [90] H.-J. Butt , B. Cappella, M. Kappl, *Surf. Sci. Rep.* **59**, 1-52 (2005).
- [91] S. Singh, S. Basu, *Surf. Coat. Tech.* **201**, 952-957 (2006).
- [92] G. Srinivas and Sung-Chul Shin, *Journal of Magnetism* **2**, 138-142 (1997).
- [93] V.M. Kuznetsov, R.I. Kadyrov and G.E. Rudenskii, *J. Mater. Sci. Technol.* **14**, 320-322 (1998).
- [94] J. D. R. Buchanan, T. P. A. Hase, and B. K. Tanner, P. J. Chen, L. Gan, C. J. Powell, and W. F. Egelhoff, Jr. *Phys. Rev. B* **66**, 104427 (2002).
- [95] T. Bigault, F. Bocquet, S. Labat, and O. Thomas, H. Renevier, *Phys. Rev. B* **64**, 125414 (2001).
- [96] S. Chakravarty, E. Hüger, H. Schmidt, M. Horisberger, J. Stahn and N.P. Lalla, *Scripta Mater.* **61**, 1117-1120 (2009).
- [97] J. Speakman, P. Rose, J. A. Hunt, N. Cowlam, R. E. Somekh, and A. L. Greer, *J. Magn. Mater.* **156**, 411-412 (1996).
- [98] L. E. Trimble, D. Finn, and A. Cosgarea, Jr., *Acta. Metall.* **13**, 501 (1965).
- [99] Mukul Gupta, Ajay Gupta, S. Rajagopalan, and A. K. Tyagi, *Phys. Rev. B* **65**, 214204 (2002).

- [100] S. Hofmann, A. Rar, D. W. Moon, K. Yoshihara, J. Vac. Sci. Technol. A **19**, 1111 (2001).
- [101] Mukul Gupta, Akhil Tayal, Ajay Gupta, Rachana Gupta, J. Stahn, M. Horisberger, and A. Wildes, J. Appl. Phys. **110**, 123518 (2011).
- [102] J. Noro, A. S. Ramos, M. T. Vieira, Intermetallics **16**, 1061 (2008).
- [103] S. Singh and S. Basu, *Solid State Physics*, edited by S. L. Chaplot, P. S. R. Krishna, and T. Sakuntala, Vol. 44, p. 257, Narosa Publishing House, New Delhi, (2001).
- [104] G. I. Grigorov, I. N. Martev, J.-P. Langeron, J.-L. Vignes, Thin Solid Films **161**, 249 (1988).
- [105] Frans Spaepen, Alison L. Shull, Curr. Opin. Solid State Mater. Sci. **1**, 679 (1996).
- [106] E. Kirkendall, L. Thomassen, C. Upthegrove, Trans. AIME **133**, 186 (1939).
- [107] E. O. Kirkendall, Trans. AIME **147**, 104 (1942).
- [108] A. L. Patterson, Phys Rev **56**, 978-982, (1939).
- [109] S. Singh, M. R. Fitzsimmons, T. Lookman, J. D. Thompson, H. Jeon, A. Biswas, M. A. Roldan and M. Varela, Phys Rev Lett. **108**, 077207 (2012).
- [110] S. Singh, S. Basu, P. Bhatt, and A. K. Poswal, Phys. Rev. B **79**, 195435 (2009).
- [111] H Zabel and K Theis-Bröhl, J. Phys. Condens. Matter **15**, S505–S517 (2003).
- [112] S.L Zhang and M. Östling, Crit Rev. Solid State Mater. Sci. **28**, 1 (2003).
- [113] L. J. Brillson, Surf. Sci. **299/300**, 909 (1994).
- [114] A. T. Hanbickia and B. T. Jonker, G. Itkos, G. Kioseoglou, and A. Petrou, Appl. Phys. Lett. **80**, 1240 (2002).

- [115] S. Singh, S. Basu, M. Vedpathak, R. H. Kodama, R. Chitra and Y. Goud, *Appl. Surf. Sci.* **240**, 251-259 (2005).
- [116] S. Singh, S. Basu, D. Bhattacharya, and A. K. Poswal, *J. Appl. Phys.* **107**, 123903 (2010).
- [117] S. Singh and S. Basu, M. Gupta, M. Vedpathak and R. H. Kodama, *J. Appl. Phys.* **101**, 033913 (2007).
- [118] D. Bhattacharya, S. Basu, S. Singh, S. Roy, B. N. Dev, *Appl. Surf. Sci.* **263**, 666–670 (2012).
- [119] H. Shang, H. Okorn-Schmidt, K. K. Chan, M. Copel, J. A. Ott, P. M. Kozlowski, S. E. Steen, S. A. Cordes, H.-S. P. Wong, E. C. Jones and W. E. Haensch: *IEDM Tech. Dig.* p. **441**, (2002).
- [120] L. J. Brillson, *J. Phys. Chem. Solids* **44**,. 703-733 (1983).
- [121] S. Zhu and A. Nakajima, *Jpn. J. Appl. Phys.* **44**, L753-L755 (2005).
- [122] F. M. Smits, *Bell System Technical Journal* **37**, 711-718, (1958).
- [123] C. Y. Lin, W. J. Chen, C. H. Lai, A. Chin, and J. Liu, *IEEE Electron Device Lett.* **23**, 464–466, (2002).
- [124] A. J. Dekker, *Solid State Physics*,(Chap 11, pp 275-304), Macmilan India Limited (2008).